J. Fluid Mech. (2014), *vol.* 758, *pp.* 5–62.
doi:10.1017/jfm.2014.505

Confinement effects in shock wave/turbulent boundary layer interactions through wall-modelled large-eddy simulations

Iván Bermejo-Moreno[1,†], Laura Campo[2], Johan Larsson[1,‡], Julien Bodart[1,§], David Helmer[2] and John K. Eaton[2]

[1]Center for Turbulence Research, Stanford University Stanford, CA 94305, USA

[2]Department of Mechanical Engineering, Stanford University, Stanford, CA 94305, USA

(Received 1 December 2013; revised 25 June 2014; accepted 27 August 2014;
first published online 3 October 2014)

We present wall-modelled large-eddy simulations (WLES) of oblique shock waves interacting with the turbulent boundary layers (TBLs) (nominal $\delta_{99} = 5.4$ mm and $Re_\theta \approx 1.4 \times 10^4$) developed inside a duct with an almost-square cross-section (45 mm $\times$ 47.5 mm) to investigate three-dimensional effects imposed by the lateral confinement of the flow. Three increasing strengths of the incident shock are considered, for a constant Mach number of the incoming air stream $M \approx 2$, by varying the height (1.1, 3 and 5 mm) of a compression wedge located at a constant streamwise location that spans the top wall of the duct at a 20° angle. Simulation results are first validated with particle image velocimetry (PIV) experimental data obtained at several vertical planes (one near the centre of the duct and three near one of the sidewalls) for the 1.1 and 3 mm-high wedge cases. The instantaneous and time-averaged structure of the flow for the stronger-interaction case (5 mm-high wedge), which shows mean flow reversal, is then investigated. Additional spanwise-periodic simulations are performed to elucidate the influence of the sidewalls, and it is found that the structure and location of the shock system, as well as the size of the separation bubble, are significantly modified by the lateral confinement. A Mach stem at the first reflected interaction is present in the simulation with sidewalls, whereas a regular shock intersection results for the spanwise-periodic case. Low-frequency unsteadiness is observed in all interactions, being stronger for the secondary shock reflections of the shock train developed inside the duct. The downstream evolution of secondary turbulent flows developed near the corners of the duct as they traverse the shock system is also studied.

Key words: compressible boundary layers, shock waves, turbulent boundary layers

1. Introduction

Shock wave/turbulent boundary layer interactions (STBLIs) are relevant in a variety of external and internal flows found in supersonic and hypersonic flight engineering

† Email address for correspondence: ibermejo@stanford.edu
‡ Present address: Department of Mechanical Engineering, University of Maryland, USA.
§ Present address: Université de Toulouse, ISAE, France.

applications. The two STBLI configurations most commonly studied in the literature are the compression ramp interaction and the reflected shock interaction. The main advantage of these canonical configurations is that they provide simpler and cleaner shock systems that locally isolate the relevant physics of the interaction. Nevertheless, for internal flows such as that occurring inside the isolator of a scramjet engine, the confinement imposed by the sidewalls of the engine modifies the shock structure as it interacts with the boundary layers developed on those sidewalls. Yet, the majority of experiments and simulations carried out to date aimed at studying the interaction between shock waves and TBLs have focused on canonical configurations in which the effects of the sidewalls are minimized (by means of wind tunnels with large aspect ratios or lateral aerodynamic fences), removed (using spanwise periodicity in simulations) or neglected (as seen, for example, in the survey of recent numerical STBLI simulations by Edwards 2008).

One aspect of the STBLI for which previous experimental and computational work has raised awareness of the importance of the three-dimensionality imposed by the effect of sidewalls is the size of the separation bubble that appears for sufficiently strong interactions. In the experiment of Green (1970), oil-flow photographs were used to study the three-dimensionality of a reflected STBLI in a rectangular wind tunnel with a relatively low aspect ratio, with the finding that the main effect of the sidewalls was the variation in the length of the separation bubble, which was found to vary by almost one order of magnitude for different geometries and the same flow conditions. In their review of two-dimensional STBLIs, Adamson & Messiter (1980) also suggest that the size of the separation bubble is enhanced by the presence of sidewalls in the wind tunnel, which was confirmed by multiple numerical simulations using spanwise periodicity (see, e.g., Priebe, Wu & Martin 2009; Hadjadj *et al.* 2010; Pirozzoli *et al.* 2010; Pirozzoli & Bernardini 2011; Priebe & Martin 2012; Morgan *et al.* 2013). In these simulations, the size of the separation bubble was typically under-predicted with respect to targeted experiments. Furthermore, when spanwise periodicity is used in simulations, Touber & Sandham (2009*b*) found that the size of the separation bubble varies with the width of the domain: if the computational domain is not sufficiently wide in the spanwise direction, the separation bubble size is over-predicted.

Linked with the flow separation observed in STBLIs is the phenomenon of low-frequency unsteadiness, which has drawn the attention of many studies in the literature (for a review, see Clemens & Narayanaswamy 2014): large-scale motion of the shock system occurs at frequencies one to two orders of magnitude lower than those characteristic of the turbulence in the incoming boundary layer (Dolling 2001). Based on direct measurements from experiments and simulations, several mechanisms have been proposed to explain such low-frequency motions, some of which have been derived in reduced-order models. Plotkin (1975) developed a simple stochastic model that assumes a linear restoring mechanism of the shock wave to its mean location based on the stability of the mean flow from the departures imposed by velocity fluctuations of the incoming TBL. Touber & Sandham (2011) developed a model mathematically equivalent to that of Plotkin, but derived from the exact form of the momentum integral equation combined with data from large-eddy simulations (LES), and hypothesized that the phenomenon of low-frequency unsteadiness is not necessarily a consequence of the upstream forcing or coherent structures as proposed by Beresh, Clemens & Dolling (2002) and Ganapathisubramani, Clemens & Dolling (2007, 2009), but an intrinsic property of the shock–boundary layer system. The dynamic mode decomposition (DMD) performed by Grilli *et al.* (2012) also discarded the upstream coherent structure of the incoming boundary layer as the relevant cause

in the observed low-frequency dynamics of their simulations. A similar conclusion was drawn from a series of STBLI LES performed by Morgan *et al.* (2013) at different Reynolds numbers and shock strengths. Pirozzoli & Grasso (2006) proposed an acoustic resonance mechanism to be responsible for sustaining the low-frequency, oscillatory motion of the separation point, and also developed a simplified model. Wu & Martin (2008), in their study of direct numerical simulations (DNS) of a compression-ramp STBLI, noted that, in accordance with Dussauge, Dupont & Debiève (2006), the Strouhal number of the low-frequency motion does not depend significantly on the Mach number and suggested that instead of an acoustic resonance, the low-frequency shock motion may be similar to the wake-mode generation in cavity flows. Piponniau *et al.* (2009) proposed a model for the low-frequency unsteadiness based on the entrainment properties of the mixing layer developed at the edge of the separation. By looking at the time signals of the separation and reattachment points in a spanwise-periodic compression-ramp STBLI DNS, Priebe & Martin (2012) noticed a low-frequency breathing motion of the separation bubble, manifested through the growth and shrinking of the extent of the separation, and suggested that the low-frequency motion is dominated by downstream effects for fully separated cases, but that upstream effects are expected to become relatively more important for mild interactions. Such a conclusion, of a combination of upstream and downstream interplaying mechanisms being responsible for the low-frequency unsteadiness and becoming dominant depending on the strength of the interaction, is aligned with the experimental findings of Souverein *et al.* (2010) when considering multiple reflected STBLIs and Humble *et al.* (2009*a*) in their tomographic PIV used to study the instantaneous three-dimensional structure of a reflected STBLI.

Despite all the previous work devoted to the study of the low-frequency unsteadiness in STBLI, little is known about the influence (if any) of the confinement imposed by the sidewalls. Dussauge *et al.* (2006) considered several experiments of reflected STBLIs and hypothesize that the three-dimensional structure of the separation bubble might be the cause of the low-frequency unsteadiness. Sidewalls play a decisive role in determining the size and shape of the separation bubble, which in turn may influence the characteristics of its own low-frequency motion and that of the shock system. In addition, just as the shock structure is modified as it interacts with the sidewall boundaries (Campo, Helmer & Eaton 2012; Helmer, Campo & Eaton 2012), it is plausible that any low-frequency motion associated with the shock system will also be altered in those regions. Furthermore, when considering the series of STBLIs resulting from the subsequent reflections on the walls (referred to as a shock train), for example, in an experimental wind tunnel or in the isolator of a scramjet, it is not known whether the large-scale motions of the different STBLIs might be coupled for some frequencies under certain circumstances.

One of the challenges faced in the numerical simulation of the interaction of shocks and TBLs is that the grid resolution required to resolve the near-wall structures of the TBL in DNS and LES greatly increases with the flow Reynolds number (see Choi & Moin 2012, and references therein). Thus, numerical simulations that resolve those near-wall structures are currently limited to flows with relatively low Reynolds numbers. For a given computational power in a simulation, the inclusion of additional walls only lowers the attainable Reynolds number. An alternative in LES is to use wall models, so that the near-wall structures are not resolved, but modelled instead (see Piomelli & Balaras 2002). The required grid spacing then scales with the boundary layer thickness, as opposed to the viscous length scale. Despite the rich history of wall-modelling developments in LES found in the literature, its application

to cases with shock waves is scarce: Kawai & Larsson (2013) developed a dynamic non-equilibrium wall model based on their own earlier equilibrium formulation (Kawai & Larsson 2012) and applied it to the reflected STBLI of Souverein *et al.* (2010). Here, non-equilibrium refers to the inclusion of the pressure-gradient and convective terms in the system of boundary layer equations solved by the wall model, terms that are otherwise neglected in the equilibrium formulation. The void of numerical simulations with even simpler equilibrium wall models applied to STBLIs leaves their validity for such flow configurations as an open question. A second alternative is the integration of Reynolds-averaged Navier–Stokes (RANS) and LES formulations into hybrid simulations, as is done in detached eddy simulations (DES) (for a review, see Spalart 2009). Two of the few computational examples that account for the presence of sidewalls using these hybrid methods are Edwards, Choi & Boles (2008) and Garnier (2009). In the latter, a modified DES methodology was used to replicate the STBLI experiments by Dupont, Haddad & Debiève (2006), finding evidence that the sidewalls induce corner separation that reduces the effective section of the wind tunnel, thus strengthening the interaction.

Another important physical phenomenon resulting from the sidewalls is precisely the presence of secondary flows developed near the duct corners. Several studies have focused on the three-dimensionality of a normal shock interacting with such corner flows (see Bruce *et al.* 2011, and references therein), linking experimentally the shock-induced separation at the centre of a wind tunnel and the size of the corner-flow separation. Evidence of these corner flows was also found for an oblique STBLI in the experiments by Dupont *et al.* (2005), who used normalized vorticity detectors placed at different heights to infer the presence of two counter-rotating vortices near the corners. The rotation frequency of these corner vortices was found to be of the same order as the low-frequency motion of the reflected shock, suggesting that there is also a direct link between the two. In the experiments by Helmer *et al.* (2012) of oblique STBLIs, the existence of corner flows was also inferred from PIV measurements taken in several planes parallel to a sidewall, at different locations inside the boundary layers. From these measurements, a qualitative representation of the downstream evolution of such corner flows as they enter the interaction region with a compression ramp was hypothesized.

The present study stems from those recent experiments of Helmer *et al.* (2012), and its objectives are to validate and use wall-modelled large-eddy simulations (WMLES) to explore the physics of a series of STBLIs inside a duct with a low aspect ratio cross-section, extending the original experimental set-up to include multiple strengths of the interaction. An experimental effort is being pursued in parallel with the numerical simulations presented here. Particular emphasis is placed on evaluating how significantly the confinement imposed by the sidewalls affects the flow. Three increasing shock strengths are considered by modifying the geometry of the shock-generating compression wedge in one of the duct walls. In § 2, we describe the mathematical formulation, simulation methodology and computational set-up. The equilibrium wall model in use is presented in § 2.1. Section 2.2 focuses on the method to synthetically generate TBLs at the inflow plane of the simulations from partial experimental PIV data, based on digital filtering techniques. In § 3, we present the simulation results, starting in § 3.1 with the validation of the WMLES by comparing time-averaged flow quantities with available experimental PIV data for two of the shock strengths under consideration. In § 3.2, WMLES results for the third, stronger-interaction case are presented, including simulations with and without sidewalls, the latter incorporating spanwise-periodic boundary conditions.

Time-averaged flow features for each simulation type are investigated first at the centre plane in § 3.2.1, followed by a description of their three-dimensionality and that of the overall shock system in § 3.2.2. Mean flow reversal is observed in this configuration for both simulations with and without sidewalls, and is investigated in § 3.2.3, where pressure and streamwise skin friction coefficient profiles are also compared with the weaker-interaction cases. Secondary flows developed on horizontal and vertical transverse planes are presented in § 3.2.4, focusing on the turbulent secondary flows developed near the duct corners, and their downstream evolution as they traverse the shock system formed inside the duct. An analysis of the instantaneous flow features is then presented in § 3.2.5, followed by an investigation of the low-frequency unsteadiness of primary and secondary reflected STBLIs. We finalize in § 4 with the conclusions of this work and several remarks on future directions. Additional validation of the equilibrium WMLES methodology is included in the Appendix, by replicating the stronger-interaction case found in the experiments of Piponniau *et al.* (2009), for which mean flow reversal was observed.

2. The computational set-up and methodology

The present simulations solve the spatially filtered compressible Navier–Stokes equations for the conserved variables of mass, momentum and total energy of a calorically perfect gas, using a finite volume formulation, control-volume based discretization on unstructured hexahedral meshes. A solution-adaptive methodology is implemented, which combines a non-dissipative centred numerical scheme and an essentially non-oscillatory (ENO) second-order shock-capturing scheme. The latter, which uses an HLLC Riemann solver for the computation of Euler fluxes, is applied in regions near shock waves, identified by a shock sensor activated according to the criterion: $-\partial u_k/\partial x_k > \max(\sqrt{\omega_j\omega_j}, 0.05c/\Delta)$, where $\partial u_k/\partial x_k$, $\omega_j\omega_j$ and c are the local dilatation, enstrophy and sound speed, respectively, and Δ is the mesh cell size. Biased, upwind schemes such as ENO result in extra numerical dissipation being added to the flow solution, which is detrimental when trying to solve turbulent flows, owing to the broad range of scales that needs to be resolved. Centred schemes, on the other hand, do not add such extra numerical dissipation and are better suited for resolving the turbulence structures, but produce spurious, unphysical oscillations at flow discontinuities (e.g. shock waves) that contaminate the solution numerically and can lead to instabilities (the Gibbs phenomenon). On the other hand, because of the extra numerical dissipation added by upwind schemes, these are better suited to capture shock waves without introducing numerical oscillations, by smearing the shock across a few cells. The numerical method in use combines these two schemes (centred and upwind) so that the upwind, dissipative scheme is primarily applied at and near shock waves, whereas the centred scheme is applied elsewhere, thus minimizing the overall numerical dissipation introduced while avoiding numerical instabilities. Owing to the polynomials used to reconstruct the fluxes at each cell face, the non-dissipative centred scheme, applied away from shocks, has nominally a fourth-order maximum degree of accuracy in regions where the mesh is Cartesian and uniform, reverting to second-order elsewhere. A mesh-based blend of the centred and upwind numerical schemes is used for numerical robustness, by expressing the Euler flux in each cell as $F = (1-\alpha)F_c + \alpha F_u$, where F_c and F_u are the fluxes calculated with the centred and upwind numerical schemes, respectively, and α ($\in [0, 1]$) is the local blending parameter. The calculation of α is based on the lack of skew-symmetry of the differencing operator (see Khalighi *et al.* 2011).

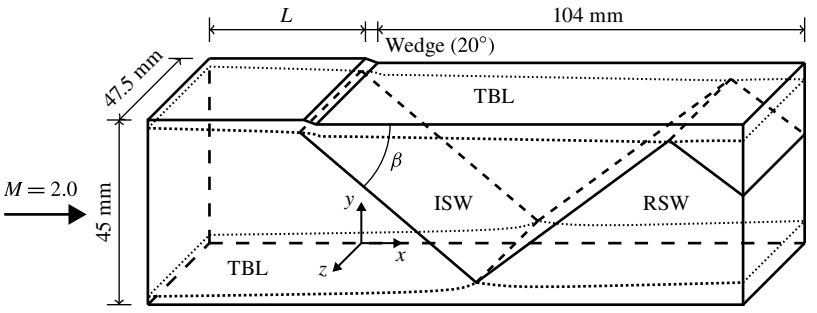

FIGURE 1. The computational domain and a schematic representation of incident (ISW) and reflected (RSW) shock waves and TBL.

Subgrid-scale stresses are explicitly modelled following Vreman (2004), and a fixed turbulent Prandtl number of 0.9 is used to model the subgrid-scale heat flux. Subgrid-scale model terms are set to zero in regions marked by the shock sensor (i.e. where the shock-capturing scheme is active), to avoid adding extra dissipation to the already dissipative ENO scheme that is applied in those regions. This subgrid-scale modelling approach was validated in Bermejo-Moreno, Larsson & Lele (2010) for the case of canonical shock–turbulence interaction, in comparison with DNS results. The discretized equations are advanced in time using a three-stage, third-order explicit Runge–Kutta algorithm.

The computational domain is shown in figure 1. It includes the test section of the wind tunnel used in the experiments by Helmer & Eaton (2011), Campo *et al.* (2012) and Helmer *et al.* (2012), consisting of a constant-area duct section (45 mm $\times$ 47.5 mm) followed by a short contraction produced by a compression wedge that spans the top wall at a 20° angle, and another constant-area section downstream of the apex of the compression wedge. The reference system is chosen such that the origin of the streamwise coordinate, x, coincides with the location of the foot of the compression wedge; y is the vertical coordinate, with its origin on the bottom wall; and z is the spanwise coordinate, with its origin on the left wall as we look downstream from inside the duct. The compression wedge (nominally two-dimensional) interacts with the incoming boundary layer developed on the top wall, generating an oblique incident shock wave that reflects off the bottom-wall boundary layer. In the present study, we consider independently three different heights of the compression wedge: 1.1, 3 and 5 mm. The strength of the incident shock and of the subsequent interactions with the boundary layers increases with the height of the compression wedge. At the apex of the compression wedge, an expansion fan is generated, turning the flow back to follow the horizontal top wall. This expansion fan propagates downstream and eventually interacts with the flow along the bottom wall.

In the experiment, a 3D converging nozzle followed by a 2D converging–diverging nozzle were used to accelerate the incoming flow of air in the wind tunnel to a nominal Mach number of approximately $M = 2.05$ in the centreline of the constant-area duct section upstream of the compression wedge, corresponding to a streamwise velocity of approximately $U_o = 525$ m s^{-1}. For the wedge deflection angle of 20° and such a Mach number, inviscid theory predicts incident shock angles of 74° and 53.4° for the strong and weak interaction cases, respectively. The thickness (δ_{99}) measured experimentally on the top-wall TBL 21 mm upstream of the foot of the wedge and at the near-centre spanwise location of $z = 21$ mm is $\delta_o = 5.4$ mm

Mesh	δ_o/Δ_x	δ_o/Δ_n	Δ_x^+	Δ_n^+	N_h
Coarse	10	$70 \rightarrow 10$	226	$32 \rightarrow 226$	4
Medium	16	$105 \rightarrow 16$	141	$22 \rightarrow 141$	6
Fine	20	$140 \rightarrow 20$	113	$16 \rightarrow 113$	7

TABLE 1. The mesh resolution in the streamwise (x) and wall-normal ($n = y, z$) directions, non-dimensionalized in outer (δ_o) and viscous (ℓ_o) units ($\xi^+ \equiv \xi/\ell_o$). Right arrows indicate the change in resolution (through grid stretching) from the wall to the core of the duct. Here, N_h is the number of LES cell centres inside the inner, wall-model layer.

and will be taken as a reference for outer-scale non-dimensionalization throughout this paper. Note that in all configurations, the compression wedge is fully immersed within the boundary layer of the top wall. The boundary layer momentum thickness measured in the experiment was $\theta \approx 450$ μm at that same upstream location (Helmer *et al.* 2012). In the simulations, the corresponding values of δ_o and θ are 5.6 mm and 479 μm, respectively. The nominal Reynolds number based on the momentum thickness of the top-wall boundary layer at the same reference streamwise station, located 21 mm (i.e. $4\delta_o$) upstream of the wedge foot, is $Re_\theta \approx 1.4 \times 10^4$, based on the free-stream velocity, density and viscosity. Alternatively, when the wall density and viscosity are considered instead, a value of $Re'_\theta = 6600$ is recovered, in close agreement with the $Re'_\theta = 6500$ value reported in Helmer *et al.* (2012).

For each wedge height, three independent simulations were run on meshes of increasing resolution to perform a grid-convergence study. Table 1 summarizes the parameters used for each mesh resolution, in terms of outer and inner units. A uniform grid spacing is used in the streamwise coordinate, whereas in the wall-normal directions the grid is stretched from the wall up to a distance $2\delta_o$, resulting an isotropic grid in the core of the duct. Each mesh is composed of 27 hexahedral blocks. In the streamwise direction, the domain is split into three parts, two of which correspond to the constant-area duct sections, whereas the third comprises the geometric contraction imposed by the compression wedge. Each of these parts contains nine hexahedral blocks that divide the transverse planes triply along the y and z Cartesian coordinate directions: a central, interior block with cells of uniform, isotropic size is located in the core of the duct, surrounded by two lateral and two vertical adjacent blocks, the cells of which are smoothly stretched in the direction normal to their limiting wall, and four additional corner blocks also stretched normal to the two perpendicular walls at their boundaries, with the same stretching laws as their adjacent lateral and vertical blocks. The (interior) boundaries of the core block are located a distance $2\delta_o$ from the corresponding parallel walls. The reference boundary layer thickness, δ_o, is used as the outer length scale, whereas the viscous length scale at the same streamwise reference location, ℓ_o, is used for the inner scaling: $\ell_o \equiv \mu_w/\rho_w u_\tau$, where μ is the dynamic viscosity, ρ is the density and $u_\tau \equiv \sqrt{\tau_w/\rho_w}$ is the friction velocity (based on the shear stress $\tau = \mu \partial u/\partial \eta$, where η is the wall-normal coordinate). The subscript w refers to the quantities taken at the wall. As shown in the fourth column of table 1, for all mesh resolutions considered, the first cell centre away from the walls is located well above the $\eta^+ \approx 1$ value required to resolve the near-wall structures, where the $^+$ superscript indicates normalization by the viscous length scale, ℓ_o.

An equilibrium wall model, described in § 2.1, is used in these simulations to model the effect of the inner part of the boundary layer instead of resolving it, significantly

lowering the computational cost. From the mesh spacing in each coordinate direction given in table 1 and the topology of the mesh explained above, the resulting number of cells for the finest resolution is approximately 40 million, for the 3 and 5 mm-high compression wedge cases. For a wall-resolved LES using the same mesh topology, the spacing imposed by the requirement to resolve the viscous, inner layer of the four boundary layers in this flow configuration would result in a mesh size of approximately 2 billion cells (i.e. 50 times the resolution of the finest WMLES attempted in this study), for the moderate Reynolds number considered. However, a 10-fold reduction in mesh size for the wall-resolved LES can be achieved by using nested grids that increase resolution near the wall in the wall-parallel directions (Chapman 1979) or by exploiting the unstructured nature of the flow solver (still resulting in roughly five times the mesh size of the finest WMLES). For larger Reynolds numbers, the reduction in mesh size and associated computational cost resulting from the use of a wall model is increasingly significant (see, e.g., the estimates provided in Choi & Moin 2012).

The streamwise distance from the inflow boundary condition (see § 2.2) to the foot of the compression wedge, L, is taken as 21 mm for the 1.1 mm-high wedge case configuration and is extended to 37 mm for the 3 and 5 mm-high wedge cases, for which the stronger compression wedge interaction starts further upstream in the top boundary layer. For the 5 mm-high wedge configuration, additional simulations with spanwise-periodic boundary conditions are performed, to better elucidate the influence of the confinement in the characteristics of the interaction by comparison with the simulations that include the sidewalls. In the spanwise-periodic simulations, a narrower domain of 23.75 mm ($\approx 4.4\delta_o$) is used in the spanwise direction to reduce the computational cost of the simulation, still ensuring that it is sufficiently wide to avoid spurious effects on the size of the separation bubble, as observed by Touber & Sandham (2009*b*).

2.1. *The wall model*

The wall model proposed by Kawai & Larsson (2012) is used in the present simulations. It solves the equilibrium boundary layer equations in a refined, near-wall inner grid, embedded in the coarser, background LES grid:

$$\frac{\mathrm{d}}{\mathrm{d}\eta}\left[(\mu+\mu_t)\,\frac{\mathrm{d}u_\parallel}{\mathrm{d}\eta}\right]=0, \tag{2.1}$$

$$\frac{\mathrm{d}}{\mathrm{d}\eta}\left[(\mu+\mu_t)\,u_\parallel\frac{\mathrm{d}u_\parallel}{\mathrm{d}\eta}+c_p\left(\frac{\mu}{Pr}+\frac{\mu_t}{Pr_t}\right)\frac{\mathrm{d}T}{\mathrm{d}\eta}\right]=0. \tag{2.2}$$

Here, $u_\parallel$ is the wall-parallel velocity, T is the temperature, c_p is the fluid-specific heat capacity at constant pressure, μ is the fluid molecular viscosity, Pr is the Prandtl number and μ_t is the wall-model eddy viscosity, which is taken from a mixing-length model as

$$\mu_t=\kappa\rho\eta\sqrt{\tau_w/\rho}\left[1-\exp\left(-\frac{\eta^+}{A^+}\right)\right]^2. \tag{2.3}$$

The model parameters are set constant: $\kappa=0.41$, $Pr_t=0.9$, $A^+=17$.

The inner, wall-model simulation takes the LES flow variables (ρ, $u_\parallel$, T) as the outer boundary condition at a specified wall-normal distance, h_{wm}. After the system of equations (2.1)–(2.2) is solved, the LES takes the wall shear stress (τ_w) and

temperature (T_w) or heat flux (q_w), for an adiabatic or isothermal boundary condition, respectively, from the wall-model inner simulation.

The wall model is applied at all four walls, which are considered adiabatic. The exchange location is taken as $h_{wm}/\delta_o = 0.056$, similar to the value used in Kawai & Larsson (2012). We performed additional simulations (not shown) halving and doubling that value, without finding significant variations with respect to the results in the flow field quantities presented in this paper. The rationale given by Kawai & Larsson (2012) to include several LES cells below the exchange location is to feed more accurate, better-resolved LES values as the outer boundary condition to the inner, wall-model simulation. Table 1 shows, for each mesh resolution, the number of LES cells in the wall-normal direction, the centre of which is located between the wall and the exchange location (N_h). From the numerical experiments of Kawai & Larsson (2012), a value of $N_h \geqslant 4$ was recommended.

The equilibrium assumption of the wall model implies that temporal, convective, pressure-gradient and wall-parallel diffusion terms are neglected in its formulation of the boundary layer equations. This assumption greatly simplifies the system of equations to be solved, changing its character from partial to ordinary differential equations (ODEs) (2.1) and (2.2). Alternative, more complete, wall-model formulations that do not assume equilibrium have been proposed in the literature (see, e.g., Cabot 1995; Balaras, Benocci & Piomelli 1996; Wang & Moin 2002; Kawai & Larsson 2013), by retaining one or multiple of the additional terms neglected under the equilibrium assumption. However, Hickel *et al.* (2012) caution that if any of the pressure-gradient, convective and temporal terms are retained, then all three of them should be retained jointly for consistency, since the pressure-gradient and convection terms balance outside the viscous sublayer, whereas the sum of temporal and convective terms describes the fluid particle evolution. The flow under consideration in this study presents strong pressure gradients (through the STBLIs) as well as secondary flows near the duct corners, resulting in boundary layers that are out of equilibrium. One of the objectives of this work is to evaluate whether an LES with an equilibrium wall model acting on a small fraction ($\lesssim 10\,\%$) of the boundary layer thickness can be used to accurately reproduce the non-equilibrium phenomena present in such flows for the regimes under consideration.

2.2. *Inflow*

In the experiments by Helmer & Eaton (2011), Campo *et al.* (2012), Helmer *et al.* (2012) and Campo, Helmer & Eaton (2013), TBLs developed on the four walls of the wind tunnel along the 325 mm-long constant-area duct section placed upstream of the compression wedge. The computational domain has its inlet located 21–37 mm upstream of the foot of the compression wedge, corresponding to the most-upstream stations where experimental PIV measurements were available ($x = -21$ mm for the 1.1 mm-high wedge configuration and $x = -37$ mm for the 3 mm-high wedge case, also used for the 5 mm-high wedge case simulations). To account for the turbulent nature of the boundary layers at the inlet of the simulations, we use a synthetic turbulent inflow generator based on a digital filtering technique originally proposed by Klein, Sadiki & Janicka (2003), with the improvements of Xie & Castro (2008) (who reduced the dimensionality of the required filtering from 3D to 2D, by adding a time correlation between consecutive 2D fields) and Touber & Sandham (2009*b*) (who extended it to compressible flows and improved the efficiency of the random fields generation). Digital filtering techniques, as any other synthetic turbulence

generation, inevitably introduce modelling errors that may take several boundary layer thicknesses of streamwise development to recover. However, one of the main advantages over existing alternatives such as rescaling/recycling (Lund, Wu & Squires 1998; Urbin & Knight 2001; Morgan *et al.* 2011) is that no low-frequency forcing is added at the inflow (Touber & Sandham 2009*b*, 2011) that could otherwise interfere with any intrinsic low-frequency motion associated with the STBLI, which will be the focus of § 3.2.6.

One-dimensional profiles of mean velocities and Reynolds stresses were available from PIV experimental measurements on vertical planes located at four spanwise locations: one near the centre (unless otherwise specified, when referring to the 'centre' of the duct, the 'spanwise centre' is implied) of the duct (at $z = 21$ mm) and three near the left sidewall (at $z = 2.5$, 4 and 5.5 mm). These experimental profiles were measured off the top wall, down to a distance from that wall of approximately $3\delta_o$. We then use symmetries and antisymmetries to reconstruct a 2D representation at the inflow plane that can be fed into the synthetic turbulence generator. In addition to the mean velocities and Reynolds stresses retrieved experimentally, pressure and temperature profiles are also required. The inlet pressure is assumed to have a constant value on the inflow plane, equal to the 33 100 Pa measured experimentally on the top wall. The mean temperature profiles are approximated from the mean streamwise velocity profiles by a Crocco–Busemann relation with a recovery factor of 0.89.

Besides the mean velocities and single-point correlations specified so far, the digital filtering technique relies on specified integral length scales in each coordinate direction that characterize the two-point correlations: presently, we consider a length scale of order δ_o in the streamwise direction (based on Pirozzoli 2012, and references therein), and $\delta_o/2$ in the transverse directions (y and z). Tutkun *et al.* (2009) studied two-point correlations from wind tunnel measurements in flat-plate TBLs at two different Reynolds numbers ($Re_\theta = 9800$ and 19 100, comparable to the 1.4×10^4 value of the present study), finding that in the spanwise direction the extent of positive two-point correlation varies between $0.4\delta_o$ and $0.8\delta_o$ across the boundary layer. When discussing the spanwise large-scale structures responsible for Reynolds stress production, Tomkins & Adrian (2003) note that these structures extend approximately 0.5δ spanwise. Following Xie & Castro (2008), the integral length scale in the streamwise coordinate is transformed into a Lagrangian time scale to enforce the two-point correlation in the direction normal to the inflow plane, avoiding the filtering of a 3D field needed in the original method by Klein *et al.* (2003). Therefore, for the choice of integral length scales, the time scales introduced at the inflow by the synthetic turbulence generator are $O(\delta_o/U_o)$.

The availability of experimental PIV data on three vertical planes near the sidewall, in addition to the near-centre plane, makes the characterization of the inflow more complete than is commonly available in previous STBLI experiments. Nevertheless, it is important to note that the reconstruction of the full inflow plane used in our simulation is still an approximation to the actual experimental conditions, and several sources of potential discrepancies exist. For example, the mean velocity and Reynolds stresses involving the spanwise coordinate were not available experimentally, as they involve the out-of-plane direction in the 2D PIV measurements. Potentially uncancelled compression/expansion waves resulting from the 3D and 2D nozzles upstream of the wind tunnel test section could lead to a different development of the bottom-wall boundary layer, which we assumed to be symmetric to the top-wall boundary layer, where the PIV data were collected. Also, the inner part of the sidewall boundary layers, in between the wall and the first plane where PIV data were

measured (2.5 mm away from the wall), is reconstructed from the top-wall boundary layer profiles, but the presence of a 2D converging–diverging nozzle upstream could lead to a different development of the boundary layers on the sidewalls with respect to those on the top/bottom walls, contrary to what is assumed. Finally, measurement uncertainties in the experiments, which are higher near the walls, will also contribute to errors in our approximation of the inflow used in the simulations.

3. Results

In this section, we present first WMLES results for the 1.1 and 3 mm-high wedge cases, for which PIV experimental data were available (see Campo *et al.* 2012, 2013; Helmer *et al.* 2012) and were used for validation of our simulation methodology described in § 2. Once confidence is built in the simulation results, we then use the WMLES databases to complement experimental findings by exploring flow features not directly available through the PIV measurements. In § 3.2, simulation results for the 5 mm-high wedge configuration are introduced, including time-averaged and instantaneous flow features. A three-way comparison among the 1.1, 3 and 5 mm-high wedge cases is made for several time-averaged quantities to elucidate the influence of the incident shock strength in the results. Secondary flows developed near the corners of the duct are studied, along with their downstream evolution as they are influenced by the shock system. An analysis of the low-frequency unsteadiness of the multiple STBLIs found for the 5 mm-high wedge case is also presented. Unless explicitly specified otherwise, the simulation results shown correspond to the finest resolution available.

3.1. *Validation of wall-modelled simulations*

To compare with experimental PIV measurements, flow variables in the WMLES were averaged in time over a period of $1000\delta_o/U_o$ after the initial transient. PIV data were available on vertical (x, y)-planes located at four spanwise locations: three near one of the sidewalls, at $z/\delta_o \approx 0.5$, 0.7 and 1.0, and one near the centre of the duct, at $z/\delta_o = 3.89$. As described in Helmer & Eaton (2011), Helmer *et al.* (2012) and Campo *et al.* (2013), for each plane, PIV data were acquired in multiple small tiles within the test section, focusing only on the regions of interaction. Composite images of those multiple tiles were used to reconstruct contour plots of mean and turbulence quantities for each plane. White areas in the PIV data shown in figures 2–5 correspond to regions where experimental data were not available, because: (*a*) those regions were away from the interactions and measurements were not acquired; (*b*) the laser sheet was obstructed (for example, in the vertical bands seen around $x/\delta_o \approx -3$ and 7 in figure 4); or (*c*) optical effects introduced false peaks in the cross-correlation (for example, the almost horizontal streaks in figures 2*a* and 3*a*).

3.1.1. *Mean velocity contours*

Figure 2 shows contours of mean vertical velocity on the near-centre ($z/\delta_o = 3.89$) plane, for the 1.1 mm- (*a*,*c*) and 3 mm-high (*b*,*d*) wedge cases, comparing available experimental PIV measurements (*a*,*b*) with WMLES results (*c*,*d*).

The main flow features observed in the near-centre plane are accurately represented by the WMLES. The compression-wedge STBLI on the top wall extends an upstream distance of approximately δ_o for the 1.1 mm-high wedge case and $2\delta_o$ for the 3 mm-high wedge case. The shock angle of the incident shock immediately upstream of the interaction with the bottom-wall boundary layer is $-38.6°$ in the PIV and

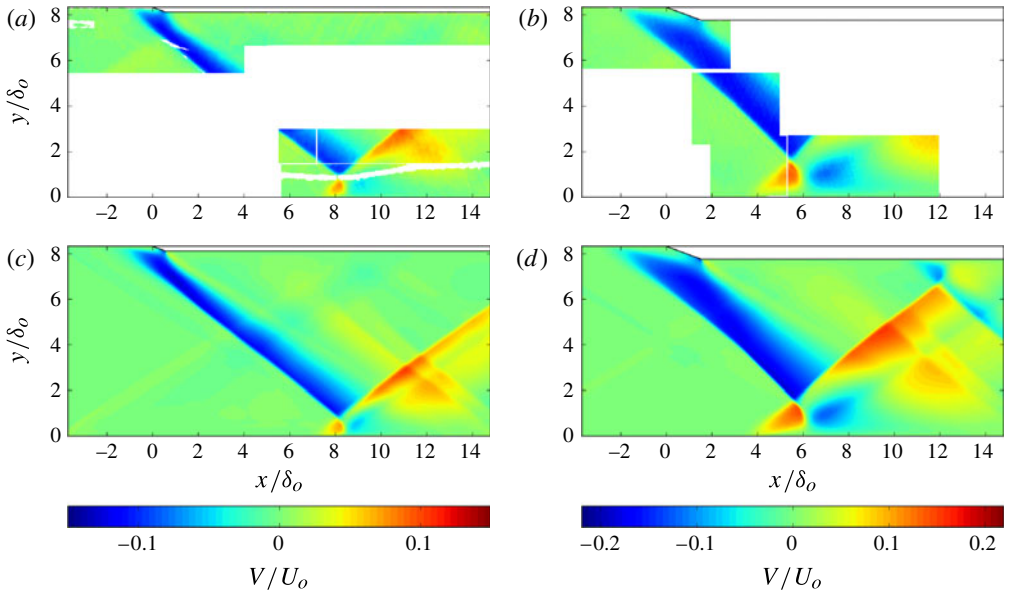

FIGURE 2. Contours of mean vertical velocity on a vertical (x, y)-plane located at $z/\delta_o = 3.89$ (near the centre of the duct) for the 1.1 mm-high wedge case (a,c) and the 3 mm-high wedge case (b,d), obtained from PIV (a,b) and WMLES (c,d). Blank regions correspond to unavailable experimental PIV measurements.

$-38.0°$ in the LES for the 1.1 mm-high wedge case. The angle of the reflected shock, for that 1.1 mm-high wedge case, is 38.3° and 38.8° in the PIV and WMLES, respectively. For the 3 mm-high wedge case, the incident shock angle is $-43.9°$ in the PIV and $-44°$ in the WMLES, whereas the reflected shock angle is 47.8° in the PIV and 45.7° in the WMLES. Note that these values differ significantly from the 53.4° shock angle that would correspond to a 20° deflection angle imposed by the compression wedge from 2D inviscid theory. The height of the shock-generating compression wedge located on the top wall is smaller than the incoming boundary layer for the three cases considered in this study. Therefore, the wedge imposes a deflection angle over a region of the boundary layer where the streamwise velocity is lower than in the free stream, resulting in a reduced strength of the generated shock. As the pressure rise propagates through the subsonic part of the boundary layer, the incoming flow upstream of the compression wedge is forced to turn away from the wall. As the height of the compression wedge increases, it penetrates into a larger portion of the top-wall boundary layer, where the velocity is also higher, resulting in a larger adverse pressure gradient that propagates further upstream of the compression ramp. A larger pressure gradient translates into a higher deflection angle needed to circumvent the larger obstruction seen by the boundary layer and, thus, into a stronger shock. This shock-generating mechanism differs from previous experiments and simulations in which the compression wedge either protrudes into or is placed in the free stream, and inviscid theory can be applied to relate the compression wedge angle with the flow deflection angle and shock strength.

The expansion fan formed at the apex of the compression wedge turns the flow back to the horizontal direction. The region of negative vertical velocity imposed by the incident shock is thus confined to a limited streamwise region (coloured blue

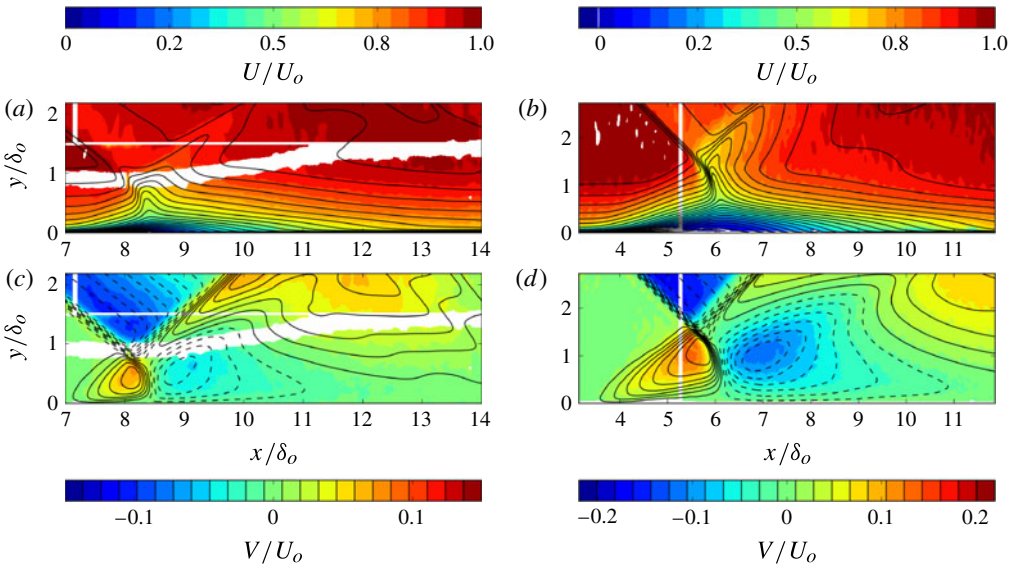

FIGURE 3. Contours of mean streamwise (*a*,*b*) and vertical (*c*,*d*) velocity on the first reflected STBLI off the bottom wall, taken on a vertical (x, y)-plane located at $z/\delta_o = 3.89$ (near the centre of the duct) for the 1.1 mm-high wedge case (*a*,*c*) and the 3 mm-high wedge case (*b*,*d*). PIV data shown in the background (by a colour map), with 24 contour lines from the WMLES data superimposed (solid and dashed lines correspond to positive and negative isocontour values, respectively).

in figure 2). Whereas its leading edge becomes sharper as the compression waves coalesce propagating downstream, the opposite holds for its trailing edge, which is smoothened (i.e. the streamwise gradient of vertical velocity decreases) by the spreading of the expansion fan as it propagates downstream.

The location and extent of the reflected STBLI on the bottom wall is well predicted by the simulations for both wedge heights, and will be the focus of a more exhaustive comparison later in this section. The region of positive vertical velocity centred around $x/\delta_o \approx 12$ (and lifted $2\delta_o$ and $3\delta_o$ for the 1.1 and 3 mm-high wedge cases, respectively) is a consequence of the three-dimensional confinement imposed by the sidewalls, which produces corner shocks that propagate towards the centre, as will be shown in detail for the 5 mm-high wedge case. Even though not confirmed experimentally, due to lack of data in that region, the WMLES for the 3 mm-high wedge case shows a secondary reflection (on the top wall) inside the computational domain, with its shock-crossing point (defined as the point of intersection between the incident and reflected shock waves) located approximately at $(x, y)/\delta_o = (12, 6.5)$.

The reflected STBLI region near the bottom wall is enlarged in figure 3, for both wedge heights. Colour contours of mean streamwise and vertical velocity extracted from the PIV are shown in the background, with the corresponding contour lines from the WMLES superimposed. A reasonable agreement is observed between experiments and simulations for these mean quantities in the plane under consideration. In particular, the shape of the interaction and the location of the shock-crossing point are accurately predicted in both configurations. In the 3 mm-high wedge case, the reflected shock departs from the shock-crossing point at a slightly ($\approx 1°$) shallower angle in the WMLES than in the experiment. It is also noticeable in this

comparison that the peak of positive vertical velocity for the 3 mm-high wedge case is displaced somewhat downstream in the simulation compared with the experiment (from $x/\delta_o \approx 5.4$ to 5.6). We note that this region corresponds to the strongest adverse gradient, and therefore it is where the equilibrium assumption of the wall model in use is most challenged (note that the agreement of contour lines is better for the equivalent positive-vertical-velocity region in the 1.1 mm-high wedge, weaker-interaction case). Despite this discrepancy in the location of the peak value of positive velocity for the 3 mm-high wedge case, good agreement is observed in the remainder of the interaction ($x/\delta_o > 6$).

For the 3 mm-high wedge case, a small region of mean flow reversal is found in both the experiment and the simulation at the reflected STBLI in the velocity field. The mean separation bubble is centred at $x/\delta_o \approx 6$ and extends a length $L_s/\delta_o \approx 0.64$ in the streamwise direction (compared with $L_s/\delta_o \approx 0.71$ found in the experiments) with a maximum height of $h_s/\delta_o \approx 0.017$. In the simulations, this region is within the wall-model inner grid, and thus below the exchange location used to transfer information from the background LES mesh to the wall-model grid. As a consequence, as will be shown in § 3.2.3, the streamwise friction coefficient for this incipiently separated case remains positive throughout the interaction. This is a consequence, for this particular case, of choosing the exchange location to be several grid cells away from the wall, in order to reduce the numerical error by utilizing information from a better-resolved part of the LES, as proposed in Kawai & Larsson (2012): the velocity passed from the LES to the wall model does not capture the flow reversal occurring below and, therefore, nor does the wall shear stress returned by the wall model to the LES. One possible solution would be to locally decrease the height of the exchange location (or even deactivate the wall model) by means of an appropriately defined sensor based on flow quantities, similarly to what is done in Bodart & Larsson (2012) in the context of transitional flows. However, even if a sensor-based approach was used and the exchange location in those regions was taken at the first cell centre from the wall (or the wall model deactivated), incipient separation could still result in a maximum height of the separation bubble that is below the first cell centre, depending on the mesh spacing at the wall and how shallow the separation bubble is. We also note that once the streamwise drop in C_f is captured and its magnitude becomes small, the role of the momentum flux is also reduced, compared with the local pressure gradient (which is still captured through the LES background grid). A further case of validation for a stronger interaction is included in the Appendix, to assess the applicability of the equilibrium WMLES methodology to cases with larger regions of mean flow reversal.

Figures 4 and 5 show mean velocity contours on the $z/\delta_o \approx 0.7$ plane (i.e. inside the left wall boundary layer) for both wedge heights, comparing PIV measurements and WMLES results, which agree qualitatively well. The colour maps are identical to those utilized in figures 2 and 3 to highlight the weakening effect that the sidewall boundary layer has on the reflected STBLIs, which almost vanish compared with the near-centre plane. This weakening effect is a consequence of the reduction of the Mach number as the sidewall is approached. Note that the sidewall boundary layers are also thickened by the action of the incident shock. Away from the bottom wall, the incident and reflected shocks are still clearly distinguishable in that near-sidewall plane, although the large gradients observed in the near-centre plane now appear smoothed by the effect of the sidewall boundary layer. The expansion fan that originates at the apex of the compression wedge on the top wall appears to be more pronounced near the sidewall in the simulations than in the experiments (compare the yellow-coloured zones emanating from the apex). As a consequence of the weakening

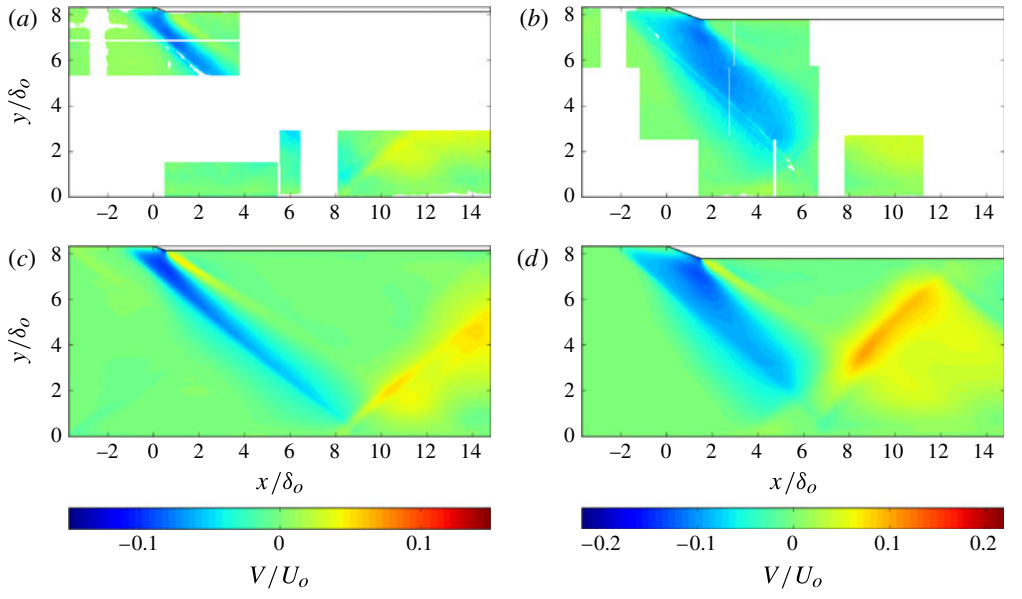

FIGURE 4. Contours of mean vertical velocity on a vertical (x, y)-plane located at $z/\delta_o \approx 0.7$ (inside the sidewall boundary layer) for the 1.1 mm-high wedge case (a,c) and the 3 mm-high wedge case (b,d), obtained from PIV (a,b) and WMLES (c,d). Blank regions correspond to unavailable experimental PIV measurements.

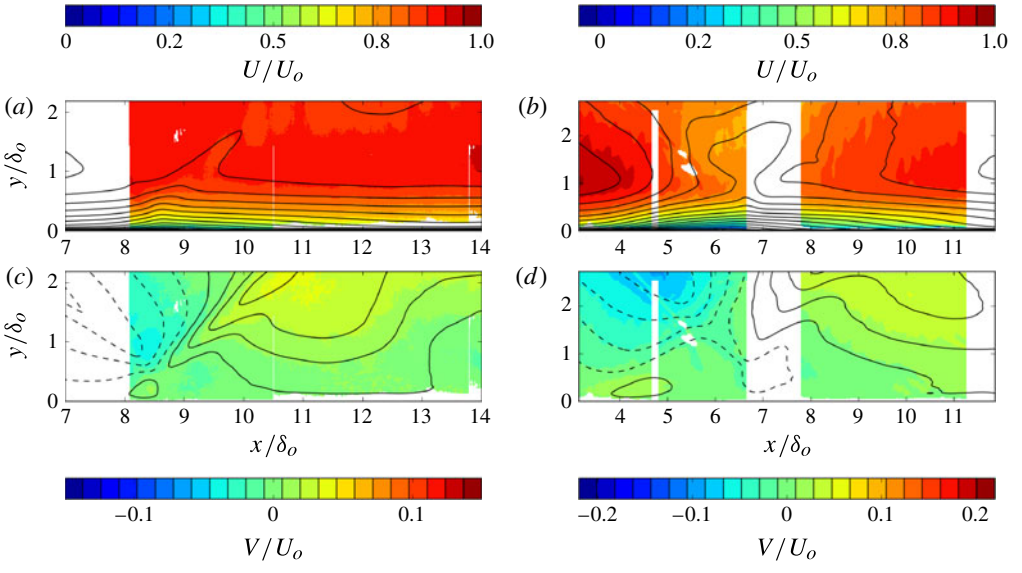

FIGURE 5. Contours of the mean streamwise (a,b) and vertical (c,d) velocity on the first reflected STBLI off the bottom wall, taken on a vertical (x, y)-plane located at $z/\delta_o \approx 0.7$ (inside the sidewall boundary layer) for the 1.1 mm-high wedge case (a,c) and the 3 mm-high wedge case (b,d). PIV data are shown in the background (by a colour map) with contour lines from the WMLES data superimposed (solid and dashed lines correspond to positive and negative isocontour values, respectively). Blank regions correspond to unavailable experimental PIV measurements.

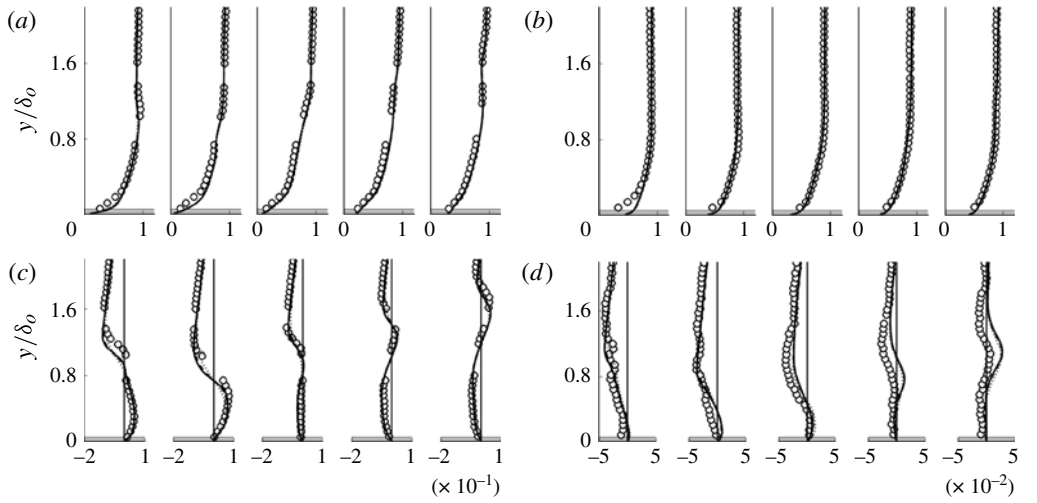

FIGURE 6. Mean velocity profiles in the reflected STBLI for the 1.1 mm-high wedge case: (*a*) and (*b*), streamwise velocity (U/U_o); (*c*) and (*d*), vertical velocity (V/U_o). (*a*) and (*c*), near-centre plane ($z/\delta_o = 3.89$); (*b*) and (*d*), near-sidewall plane ($z/\delta_o \approx 0.7$). From left to right in each plot: $x/\delta_o = 7.8$, 8.2, 8.5, 8.9, 9.3. Symbols: PIV data; solid, WMLES fine resolution; dashed, WMLES medium resolution; dotted, WMLES coarse resolution. Shaded grey areas near $y/\delta_o = 0$ represent the extent of the inner, wall-model layer in the simulations.

effect of the sidewall boundary layer on the shock system, the STBLI on the bottom wall is also mildly pushed downstream about $\delta_o/2$ (see figure 5). We performed comparisons (not shown) between experiments and simulations for the other two near-sidewall planes ($z/\delta_o = 0.5$ and 1.0) where PIV data had been collected, finding similar levels of qualitative agreement.

3.1.2. *Wall-normal vertical profiles of mean velocities and Reynolds stresses*

A more quantitative comparison between PIV experimental measurements and simulation results is presented in figures 6–9, which show one-dimensional profiles of mean velocities (in the streamwise, U/U_o, and vertical, V/V_o, directions) and Reynolds stresses ($\sqrt{\overline{u'u'}}/U_o$, $\sqrt{\overline{v'v'}}/U_o$, $-\overline{u'v'}/U_o^2$), extracted at five streamwise locations spanning the reflected STBLI on the bottom wall, for the 1.1 and 3 mm-high wedge cases. Profiles are taken at several streamwise locations for two planes: one near the centre of the duct, $z/\delta_o = 3.89$, and one near the left sidewall, $z/\delta_o = 0.7$. Results on the other two planes near the sidewall for which PIV measurements were available (at $z/\delta_o \approx 0.5$ and 1.0) are not shown, since they lead to similar conclusions regarding the WMLES–PIV comparison. A comparison of the mean velocities and Reynolds stresses in the undisturbed incoming bottom-wall boundary layer can be seen in the leftmost plots in figures 8 and 9.

The WMLES results are plotted in figures 6–9 for the three mesh resolutions considered, so that the grid-convergence of the results can be assessed. The shaded grey area in each plot represents the wall-normal extent of the inner grid used in the simulation by the wall model. We note that the simulation profiles shown in these figures correspond to the LES background grid solution. Inside the grey shaded

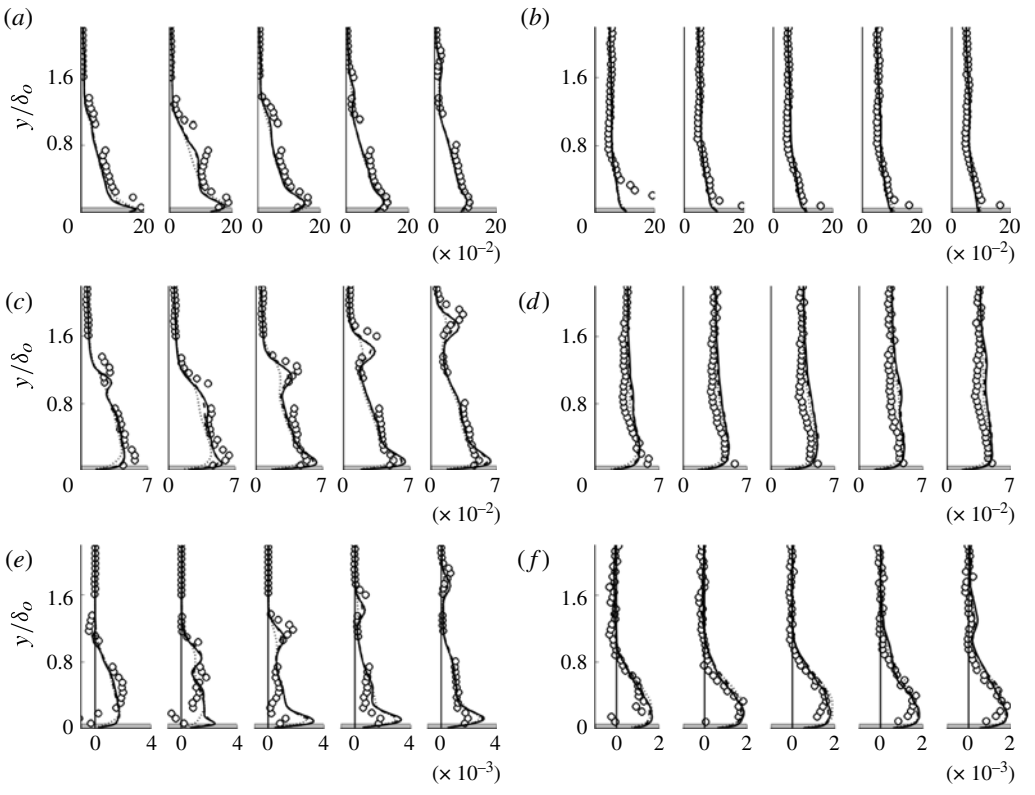

FIGURE 7. Reynolds stress profiles in the reflected STBLI for the 1.1 mm-high wedge case: (*a*) and (*b*), normal streamwise Reynolds stress ($\sqrt{\overline{u'u'}}/U_o$); (*c*) and (*d*), normal vertical Reynolds stress ($\sqrt{\overline{v'v'}}/U_o$); (*e*) and (*f*), Reynolds shear stress ($-\overline{u'v'}/U_o^2$). (*a*), (*c*) and (*e*), near-centre plane ($z/\delta_o = 3.89$); (*b*), (*d*) and (*f*), near-sidewall plane ($z/\delta_o \approx 0.7$). From left to right in each plot: $x/\delta_o = 7.8$, 8.2, 8.5, 8.9, 9.3. Symbols: PIV data; solid, WMLES fine resolution; dashed, WMLES medium resolution; dotted, WMLES coarse resolution. Shaded grey areas near $y/\delta_o = 0$ represent the extent of the inner, wall-model layer in the simulations.

regions, the wall-model solution (not shown) is being used instead by the simulation to provide the wall boundary condition to the LES.

For the 1.1 mm-high wedge case, the mean velocities are accurately reproduced by the WMLES (see figure 6). The streamwise velocity profiles on the plane near the sidewall remain practically unchanged across the interaction, in contrast to the profiles on the plane near the centre of the duct, confirming the dampening effect of the sidewall boundary layer on the strength of the STBLI earlier described in § 3.1.1. The profiles of mean vertical velocity also show the weakened interaction (note the reduction of one order of magnitude in the scale used to plot the near-sidewall profiles compared with the near-centre ones). For the two most-downstream vertical velocity profiles near the sidewall shown in figure 6(*d*), the WMLES under-predicts the values observed in the PIV, although the shape of the profiles is well captured.

The profiles of Reynolds stresses for the 1.1 mm-high wedge case in the near-centre plane (see figure 7*a*,*c*,*e*) show good agreement between PIV and WMLES in shape and absolute magnitude. The locations of the incident and reflected shocks can be

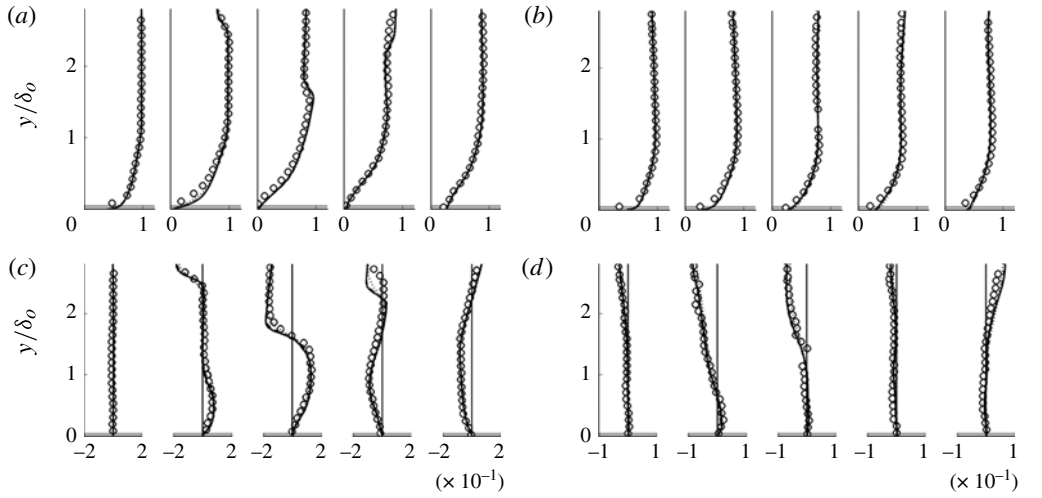

FIGURE 8. Mean velocity profiles in the reflected STBLI for the 3 mm-high wedge case: (*a*) and (*b*), streamwise velocity (U/U_o); (*c*) and (*d*), vertical velocity (V/U_o). (*a*) and (*c*), near-centre plane ($z/\delta_o = 3.89$); (*b*) and (*d*), near-sidewall plane ($z/\delta_o \approx 0.7$). From left to right in each plot: $x/\delta_o = 2.1, 4.6, 5.4, 6.4, 7.9$. Symbols: PIV data; solid, WMLES fine resolution; dashed, WMLES medium resolution; dotted, WMLES coarse resolution. Shaded grey areas near $y/\delta_o = 0$ represent the extent of the inner, wall-model layer in the simulations.

clearly identified by the intermediate peaks (moving from $y/\delta_o \approx 0.8$ to 1.8) of the vertical Reynolds stress (central plots) as we traverse the profiles for the five different streamwise locations shown. These peaks are the result of the amplification of turbulence experienced across the shock (see Larsson & Lele 2009). A rise of the normal streamwise Reynolds stress (top plots) is observed in the PIV near the gaps in the available data, but the simulation results show monotonic profiles in those regions. We attribute this rise seen in the PIV to an experimental error derived from the presence of the optical obstruction (at a constant height of $y/\delta_o \approx 0.9$). The Reynolds shear stress profiles (bottom plots) show a generally good agreement between experiments and simulations, although some discrepancies are seen in the near-wall ($y/\delta_o \lesssim 0.3$) behaviour for the profiles at the three most-upstream streamwise locations considered, where the PIV profiles drop to low and even negative values, whereas the simulation profiles remain positive and drop to zero very near the wall. This might be related to the systematic bias reported in Helmer & Eaton (2011) towards lower values of vertical and shear Reynolds stresses in the PIV experimental measurements, found to be more pronounced in the near-centre plane than in the planes located near the sidewall. Experiments by Souverein (2010), using a similar PIV technique to investigate a reflected STBLI, also showed a consistent under-prediction of the Reynolds shear stress in the near-wall region ($y/\delta_o \lesssim 0.3$), when compared with earlier hot-wire anemometry measurements by Klebanoff (1955). Helmer & Eaton (2011) suggested that this bias might be a consequence of peak-locking acting to damp the measured wall-normal fluctuations, and thus resulting in a probability density function (p.d.f.) biased towards zero displacement.

For the near-sidewall plane in the 1.1 mm-high wedge case (figure 7*b*,*d*,*f*), the simulations results recover the correct levels of turbulence in each direction away

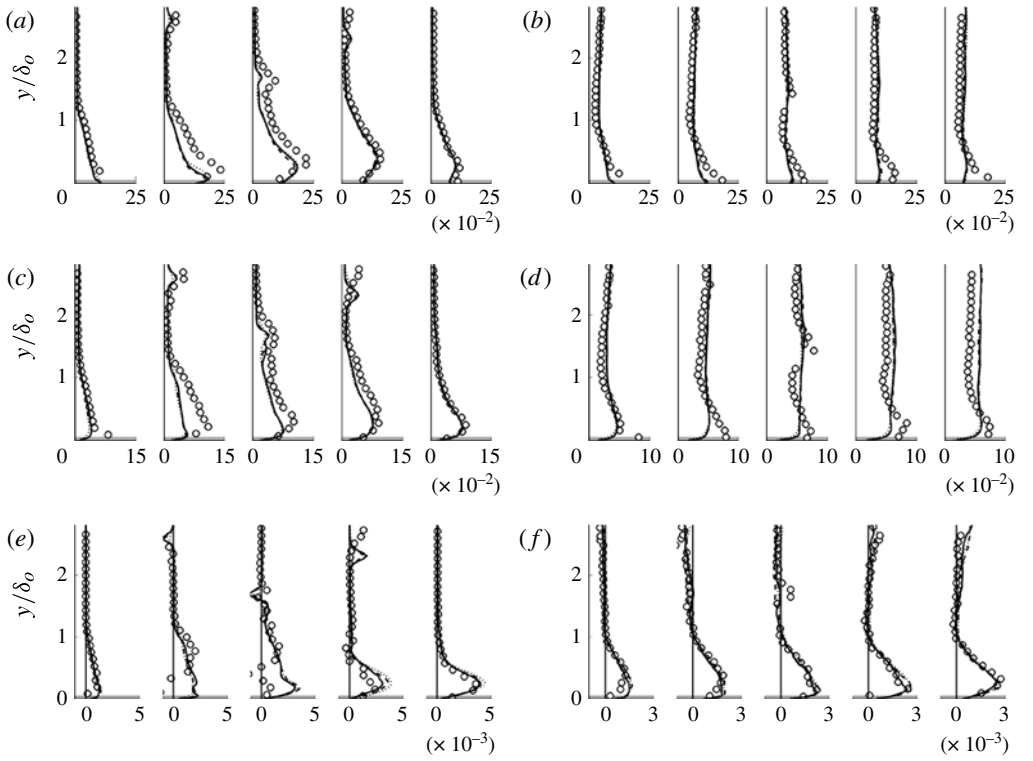

FIGURE 9. Reynolds stress profiles in the reflected STBLI for the 3 mm-high wedge case: (*a*) and (*b*), normal streamwise Reynolds stress ($\sqrt{\overline{u'u'}}/U_o$); (*c*) and (*d*), normal vertical Reynolds stress ($\sqrt{\overline{v'v'}}/U_o$); (*e*) and (*f*), Reynolds shear stress ($-\overline{u'v'}/U_o^2$). (*a*), (*c*) and (*e*), near-centre plane ($z/\delta_o = 3.89$); (*b*), (*d*) and (*f*), near-sidewall plane ($z/\delta_o \approx 0.7$). From left to right in each plot: $x/\delta_o = 2.1, 4.6, 5.4, 6.4, 7.9$. Symbols: PIV data; solid, WMLES fine resolution; dashed, WMLES medium resolution; dotted, WMLES coarse resolution. Shaded grey areas near $y/\delta_o = 0$ represent the extent of the inner, wall-model layer in the simulations.

from the bottom wall (as imposed through the synthetic turbulence generator at the inflow). The variation of these profiles across the STBLI is again less noticeable than near the centre of the duct, a consequence of the weakening of the interaction by the effect of the sidewall boundary layer. The peaks resulting from the incident and reflected shocks, observed in the vertical Reynolds stress profiles near the centre of the duct, are not present for the profiles near the sidewall. The rapid increase of streamwise Reynolds stress very near the wall is under-predicted by the simulations, but the agreement is good everywhere else. The vertical and Reynolds shear stresses are accurately predicted. The drop observed in the Reynolds shear stress near the bottom wall at some stations in the near-centre plane is much less noticeable in these profiles on the near-sidewall plane.

The 3 mm-high wedge case also shows good agreement of the mean velocity profiles, for both planes considered (see figure 8). The normal Reynolds stresses (figure 9) show a small under-prediction in the simulations for $y/\delta_o \lesssim 1$ at the core of the interaction in the near-centre plane, recovering the PIV values as we move downstream in the interaction. Reynolds shear stresses are consistently well

predicted (excluding the drop near the bottom wall observed in the PIV for profiles in the near-centre plane at the core of the interaction, which could be a result of a measurement bias as explained above).

3.2. *Strong interaction, 5 mm-high wedge case*

Once confidence in the simulation methodology was built for the 1.1 and 3 mm-high wedge cases, as presented in § 3.1, we performed additional simulations for a stronger-interaction case corresponding to a 5 mm-high wedge configuration, keeping the same 20° wedge angle. The primary goal of these simulations was to produce a larger region of mean flow reversal by an increased shock strength, to study the effects of the confinement imposed by the sidewalls on the extent and dynamics of the separation bubble. Since no experimental data were available for this 5 mm-high wedge configuration, direct validation of the applicability of the equilibrium wall model for this configuration is not possible. For that reason, an extra case of validation is included in the Appendix, replicating the strongest interaction found in previous experiments by Piponniau *et al.* (2009), for which significant mean flow reversal was observed.

We performed two sets of simulations with the 5 mm-high wedge: one set includes the sidewalls whereas the other set uses spanwise-periodic boundary conditions, resulting in a nominally two-dimensional interaction. Three meshes of increasing resolution were considered for each set. The streamwise length of the computational domain in both cases is identical to the 3 mm-high wedge configuration. Simulations with the sidewalls have the same grid spacing parameters as shown in table 1, whereas the spanwise-periodic simulations have a reduced domain width of $4.4\delta_o$ with a uniform grid spacing in z (i.e. no stretching away from the centre plane). Results for the finest resolution will be presented.

3.2.1. *Time-averaged flow features at the centre plane*

Figure 10 shows contours of streamwise and vertical mean velocities for simulations with and without sidewalls. Mean sonic and separation lines are superimposed as dashed and solid lines, respectively, in each plot. Regions of mean flow separation appear in both simulations in the compression STBLI (top wall) and, as targeted, in the first reflected STBLI (bottom wall). The extent and location of these separated regions differ between the two simulations, and will be investigated in § 3.2.3. However, the most striking difference between the two simulations is the character of the first reflected STBLI at the bottom wall: the spanwise-periodic simulation shows a regular shock intersection, whereas the simulation with sidewalls presents a singular shock intersection centred around $(x, y) \approx (3.43, 2.75)\delta_o$. Schematic representations highlighting the main features of these two types of reflected STBLI are shown in figure 11. In the singular intersection, a Mach stem is formed in between the incident and reflected shock waves, consisting of a quasi-normal shock with two triple points at the intersection with the incident and separation shocks and the reflected and transmitted shocks, respectively (Babinsky & Harvey 2011). A region of subsonic flow appears immediately downstream of the Mach stem, which is accelerated by the surrounded regions of supersonic flow on each side until the flow in the wake of the Mach stem becomes supersonic again, passing through a sonic throat. The wake is slightly turned downward by the expansion fan reflected as the transmitted shock penetrates the boundary layer (see figure 11*b*). The wake remains visible throughout the rest of the computational domain (see figures 10*a* and also 13*b*) interacting with

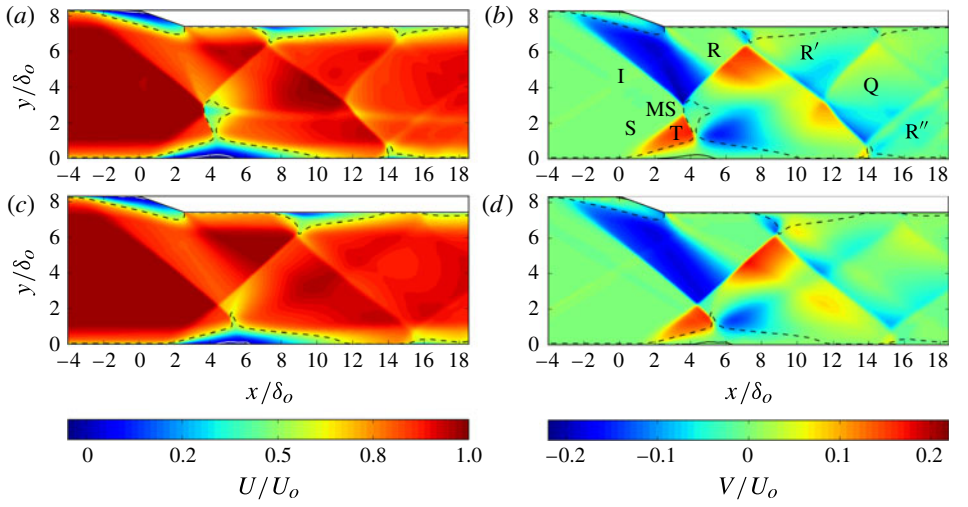

FIGURE 10. Contours of mean streamwise (*a*,*c*) and vertical (*b*,*d*) velocities for the 5 mm-high wedge case at the centre plane ($z/\delta_o = 4.4$), with the sonic line (dashed) and separation lines (solid) superimposed in each plot. Comparison between simulations with sidewalls (*a*,*b*) and spanwise periodicity (*c*,*d*). I, incident shock generated by the compression corner; MS, Mach stem; S, T and R, separation, transmitted and reflected shocks from the first STBLI at the bottom wall; R′, reflected shock from the second STBLI at the top wall; Q, incident shock on the third STBLI at the top wall; R″, reflected shock from the second STBLI at the bottom wall.

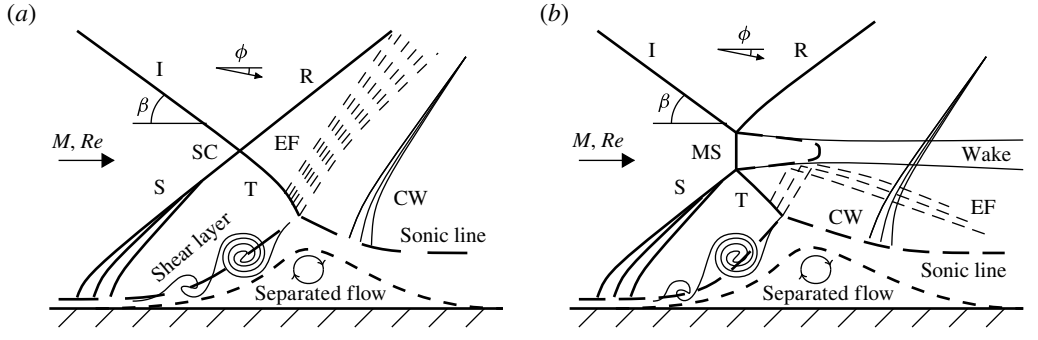

FIGURE 11. A schematic representation of regular (*a*) and singular (*b*) shock intersections in a STBLI with mean flow separation. I, incident shock; S, separation shock; R, reflected shock; T, transmitted shock; SC, shock-crossing point; MS, Mach stem; EF, expansion fan; CW, compression waves; ϕ, deflection angle.

the shock train. The Mach stem and its influence in the flow will be studied in more detail in § 3.2.5.

In the simulation with the sidewalls, for which the Mach stem (MS) appears, the incident shock wave (I) formed by the compression wedge has an angle of −40° at the core of the duct. This angle is steeper than in the lower-wedge cases, as the higher compression wedge now affects a larger portion of the top-wall boundary layer, but still lower than the 53.4° predicted by inviscid theory for a deflection of 20° imposed

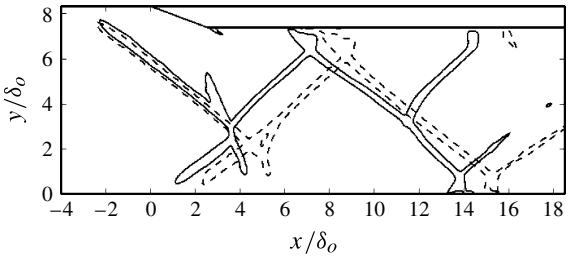

FIGURE 12. The shock system at the centre plane ($z/\delta_o = 4.4$) identified by isolines of mean density gradient along the streamwise direction ($\partial\rho/\partial x = 4 \times 10^3 \rho_o/\delta_o$) for the 5 mm-high wedge configuration: solid lines, simulation with sidewalls; dashed lines, spanwise-periodic simulation.

by the compression wedge. At the first STBLI on the bottom wall, the angle of the separation shock (S) formed by the compression waves emanating from the bottom-wall boundary layer is 38°. Below the Mach stem, the transmitted shock (T) has an angle of −63°, whereas the reflected shock above the Mach stem (R) departs at 47°. This angle reduces to 42° before R interacts with the top-wall boundary layer, the own reflected shock (R′) of which departs at a −34° angle, and steepens to −37° further downstream. An additional shock interaction occurs in the core of the duct at $x/\delta_o \approx 12$, as R′ approaches the wake of the Mach stem: the shock angle of R′ steepens to −52° and a new oblique shock (Q) forms, with an angle of 62° towards the top wall. As R′ crosses the wake of the Mach stem, the shock angle becomes −44° before impinging on the bottom-wall boundary layer in a third reflected STBLI (located at $x/\delta_o \approx 14$). The Q shock gradually decreases its angle before impinging on the top wall in a fourth STBLI (located at $x/\delta_o \approx 14.3$).

In the spanwise-periodic simulation, the Mach stem is not present and a regular shock intersection occurs, in contrast to the simulation with sidewalls. This is an indication that, for this geometric configuration and flow parameters, the confinement effects imposed by the sidewalls are responsible for strengthening the incident and separation shocks to a point beyond which their two polars cannot intersect, requiring a quasi-normal shock and two triple points that provide the singular Mach intersection, also known as the direct Mach phenomenon and Edney type II shock interference. In the STBLI experiments by Dupont *et al.* (2005, 2006), Piponniau (2009), Piponniau *et al.* (2009) and Souverein *et al.* (2010), regular shock intersections occurred for even the strongest interaction, which is replicated in the WMLES presented in the Appendix. In those experiments, the cross-section of the wind tunnel had a higher aspect ratio, compared with the almost-square duct configuration of the present work, for which the relative width of the boundary layer is also larger, when compared with the cross-section dimensions. Singular shock intersections have been observed experimentally, for example, in over-expanded nozzles (Bourgoing & Reijasse 2005; Délery & Dussauge 2009).

To aid in the comparison between the simulation with spanwise periodicity and the simulation including sidewalls, figure 12 shows the shock systems educed from both simulations by isolines of the streamwise gradient of time-averaged density. The incident shock generated by the compression wedge has the same angle as in the simulation with sidewalls (−40°). The lack of a Mach stem in the spanwise-periodic simulation translates into the first reflected STBLI occurring (approximately $0.8\delta_o$)

further downstream than in the simulation with sidewalls. The shock-crossing point between the incident and reflected shocks for the regular interaction is also located at a lower height than its triple-point counterpart in the case with the Mach stem. Together with the fact that the angle of the R reflected shock is lower (43°) than in the simulation with sidewalls (47°), the secondary STBLIs will be displaced further downstream ($\approx 1.5\delta_o$) in the spanwise-periodic simulations. The Q shock found in the simulation with sidewalls is not present in the spanwise-periodic simulation (its origin will be explained later in this paper when looking at the corner shocks). However, the compression waves that emanate from the first STBLI at the bottom wall propagate downstream, generating a much weaker interaction with the top-wall boundary layer at $x/\delta_o \approx 15.5$, compared with the stronger, fourth STBLI described for the simulation with sidewalls.

3.2.2. *The three-dimensionality of the time-averaged flow features*

We now focus our attention on the three-dimensionality imposed by the sidewalls across the spanwise direction, z. Results from the simulation with sidewalls will also be compared with the spanwise-periodic simulation, for which the homogeneity in the z direction makes it a nominally two-dimensional interaction.

Figure 13 shows contours of streamwise normal Reynolds stress, $\sqrt{\overline{u'u'}}/U_o$, on selected vertical planes of the simulation with sidewalls, both along the streamwise coordinate ((x, y)-planes, figure 13*b–f*) and normal to it ((y, z)-planes, figure 13*g–j*). Spanwise-averaged contours of the same quantity for the spanwise-periodic simulation are also shown in figure 13(*a*). The streamwise normal Reynolds stress is chosen as the plotted field as it clearly identifies the TBLs, the shock system and the shear layers delimiting the wake of the Mach stem, when present. Mean separation and sonic lines are superimposed on each plot in solid and dashed style, respectively.

The Mach stem reaches its maximum strength at the centre plane ($z/\delta_o = 4.4$, figure 13*b*), where it extends vertically for approximately $0.5\delta_o$. Moving away from the centre plane towards the sidewalls (figure 13*c–f*), the Mach stem progressively shrinks, decreasing its height and eventually vanishing (figure 13*e*). A regular shock intersection is then recovered, before reaching the sidewall boundary layer (figure 13*f*). A cross-sectional plane passing through the Mach stem is shown in figure 13(*h*), so that its shape, spanwise and vertical extent can be visualized better: note the superimposed sonic (white dashed) lines, confirming that the curvature of the Mach stem is decreasing its height away from the centre plane, and vanishing at a distance of approximately $2.5\delta_o$ from the sidewalls. It will be shown later that such curvature is imposed by corner shocks emanating from the top wall.

The TBLs are thickened through the different STBLIs, and recover along the downstream relaxation zones from the turbulent amplification experienced at each interaction, becoming thinner. Based on the normal streamwise Reynolds stresses at the centre plane (figure 13*b*), the compression wedge interaction thickens the top boundary layer by approximately 30 %, whereas the shock reflection near the bottom wall thickens its boundary layer by 60 %. Both values are slightly higher than their counterparts in the spanwise-periodic simulation (figure 13*a*).

The relaxation zone that follows the first bottom-wall STBLI is also shorter in the streamwise direction in the simulation with sidewalls and results in a thinner boundary layer than in the spanwise-periodic simulation, a consequence of the stronger downward mean velocity imposed by the interaction downstream of the transmitted shock when sidewalls are present (compare figure 3*b*,*d*). Thus, even though the subsequent secondary STBLI on the bottom wall is stronger when

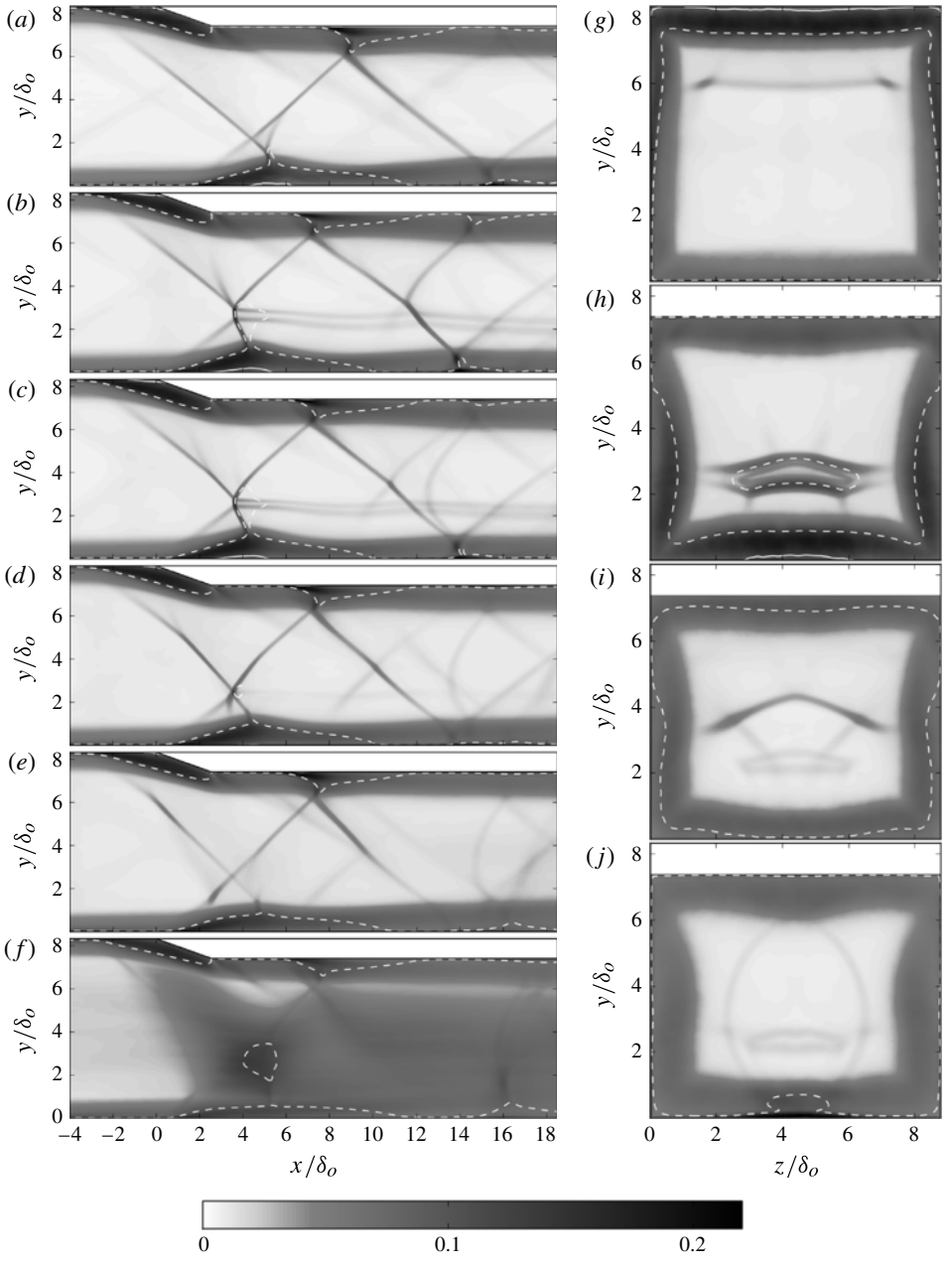

FIGURE 13. Contours of the streamwise Reynolds stress ($\sqrt{\overline{u'u'}}/U_o$) on vertical planes normal to z (*a–f*) and normal to x (*g–j*): (*a*) contours at $z/\delta_o = 4.4$ for the spanwise-periodic simulation; (*b–f*) contours at $z/\delta_o = \{4.4, 3.5, 2.6, 1.8, 0.9\}$, respectively, for the simulation with sidewalls; (*g–j*) contours at $x/\delta_o = \{0.0, 3.7, 10, 14\}$, respectively, for the simulation with sidewalls. Mean sonic (dashed) and separation (solid) lines are superimposed on each plane.

sidewalls are present, as seen by the steeper incident shock and higher Reynolds stresses in figure 13(*b*) relative to its counterpart in the spanwise-periodic simulation (figure 13*a*), the thickness of the bottom-wall boundary layer by the end of the computational domain is still larger for the spanwise-periodic simulation (by 30 %).

On the contrary, at the top wall, the secondary STBLI is stronger in the spanwise-periodic simulation, as indicated by the larger amplification of the streamwise Reynolds stress and the steeper angle of the reflected shock, and results in a (10 %) thicker boundary layer than in the simulation with sidewalls. However, the additional STBLI found on the top wall near the centre plane at $x/\delta_o \approx 14$ when sidewalls are present (figure 13*b*) further thickens the boundary layer, so that at the exit of the computational domain, both simulations show a similar thickness of the top-wall boundary layer. Looking at transverse (y, z)-planes at different streamwise locations in figure 13(*g–f*), the boundary layers appear to be highly three-dimensional throughout the interactions. From an almost uniform thickness found upstream of the interactions (see, for example, the bottom-wall boundary layer in figure 13*g*), all boundary layers thicken more (≈15 %) near the centre of each wall than near the duct corners at the first STBLI (figure 13*h*). The opposite holds further downstream (figure 13*i*), where the relaxation experienced by the bottom-wall boundary layer after the STBLI makes it thinner near the spanwise centre ($z/\delta_o \approx 4.4$), but the interaction with lateral shocks continues, thickening the boundary layers near the bottom-wall corners. The boundary layers on the top wall and the sidewalls also show non-uniform thickening across their span throughout the interactions with shocks. Secondary flows occurring near the corners, their effect on the boundary layers and downstream evolution through the interactions will be investigated in § 3.2.4.

The overall shock system is also curved away from the centre of the duct by the confinement imposed by the sidewalls. This is visible, for example, in the cross-sectional planes located downstream of the first STBLI: figure 13(*i*) shows the increasing convexity of the reflected shock resulting from the first STBLI at the bottom wall, whereas figure 13(*j*) shows two highly curved secondary shocks enclosing the wake of the Mach stem at a streamwise location near the second STBLI at the bottom wall ($x/\delta_o = 14$). The three-dimensional structure of the shock system inside the computational domain is visualized in figure 14 and confirms the curved nature of the reflected and secondary shocks earlier described. In addition, figure 14 clearly shows the lateral separation shocks that form near the sidewalls and intersect with the incident and reflected shocks of the first STBLI at the bottom wall, confining the Mach stem to the core of the duct in the spanwise direction.

Several corner shocks are visible throughout the domain, resembling the irregular shock reflection generated by two intersecting wedges immersed in a supersonic inviscid stream (Kutler 1974; Gun'ko, Kudryavtsev & Rakhimov 2004). The STBLIs on the top and bottom walls generate adverse pressure gradients that are also felt on the sidewalls and thicken the lateral boundary layers, which effectively act as secondary wedges and thus generate the lateral and corner shocks. For example, the intersections of the incident shock generated by the compression wedge on the top wall and the lateral shocks generated by the sidewalls develop into two corner shocks that propagate downstream and towards the centre of the duct, until they eventually intersect with the Mach stem, which then adopts a lenticular shape. The cross-sectional plane taken at the streamwise location of the foot of the wedge shown in figure 13(*g*) shows the presence of these corner shocks interacting with the incident compression shock at $y/\delta_o \approx 6$. Note that, in contrast to the top wall, no corner shocks are visible near the first STBLI at the bottom wall; instead, regular

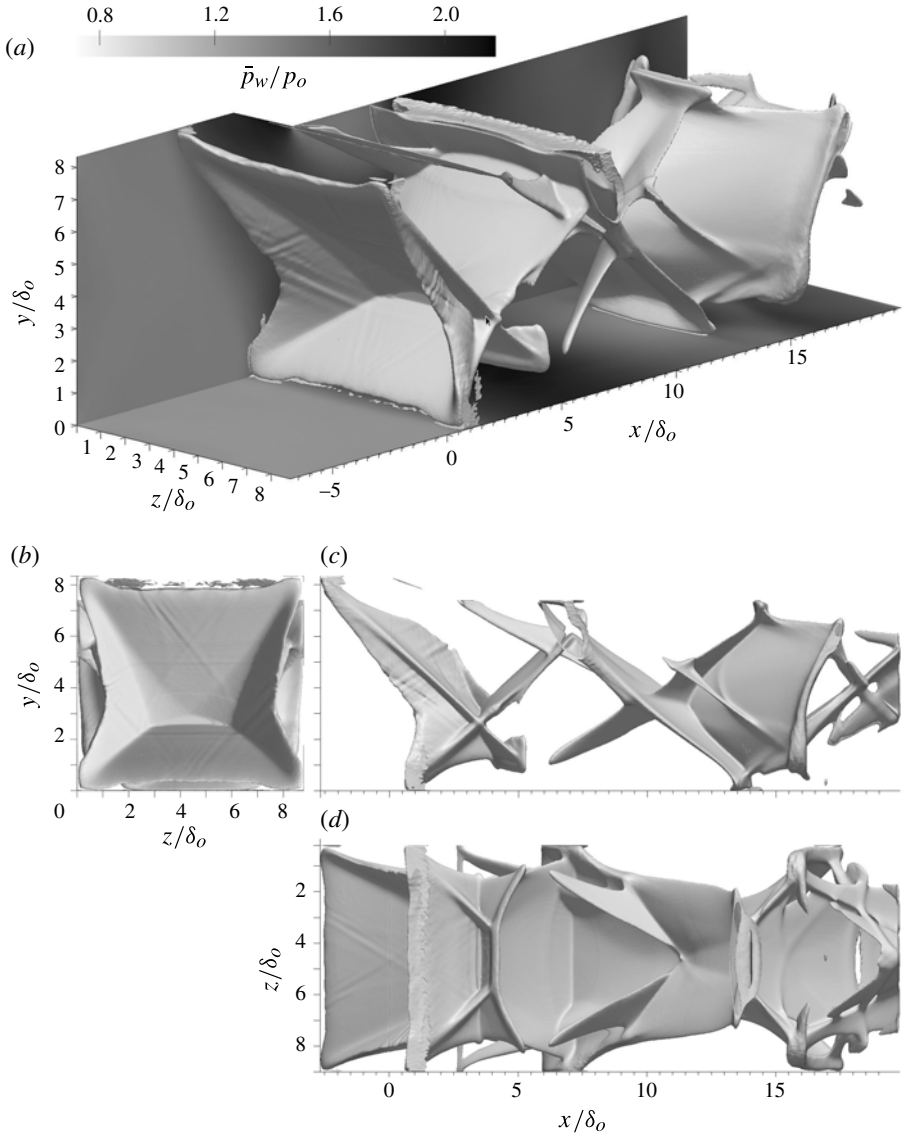

FIGURE 14. The isosurface of the mean density gradient in the streamwise direction (at a contour value of $\partial\overline{\rho}/\partial x = 0.21\rho_o/\delta_o$), showing the three-dimensional structure of the shock system: (*a*) a 3D projection, with contour plots of mean wall pressure shown on the bottom and left walls (from 0.7 to 2.2 p_o, white to black); (*b*) a view along the streamwise direction from an upstream location; (*c*) the side view; (*d*) the bottom view.

intersections between the separation shocks formed on the bottom and sidewalls occur. Other instances of corner shocks are found starting at the end of the compression wedge on the top wall, and also immediately downstream of the transmitted shock of the first STBLI on the bottom wall. The latter intersect near the centre of the duct with the reflected shock from the second STBLI on the top wall (see figure 13*d*). The transmitted corner shocks then jointly form a narrower oblique shock near the centre of the duct (figure 13*a*) that becomes the incident shock for the third STBLI

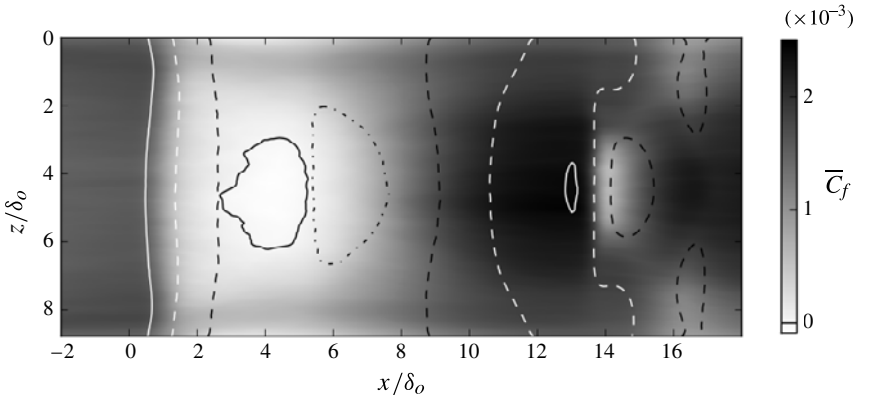

FIGURE 15. Contours of the mean streamwise skin friction coefficient, $\overline{C}_f$, on the bottom wall (grey scale) with the mean separation line ($\overline{C}_f = 0$) in solid black and isolines of the mean wall pressure at $\overline{p}_w/p_o = 1.12$ (solid white), 1.42 (dashed white), 1.72 (dashed black) and 2.02 (dash-dotted) superimposed, for the simulation with sidewalls.

on the top wall. Note that this incident shock near the centre plane resulting from the transmitted corner shocks can be clearly identified in the contours of streamwise Reynolds stress shown in figure 13(*b*). This is in contrast to the spanwise-periodic simulation, represented in figure 13(*a*), for which no corner shocks exist.

As each lateral shock interacts with the transmitted shock of the first STBLI at the bottom-wall boundary layer ($x/\delta_o \approx 3$), a λ shock structure forms (see figure 14*d*). The flow deceleration through the lateral shock in that λ pattern is responsible for the spanwise curvature of the transmitted shock near the sidewalls. There is also a noticeable decrease in the spanwise extent of successively reflected STBLIs in the shock train on the bottom and top walls.

3.2.3. *Mean flow reversal*

Both spanwise-periodic and sidewall simulations present regions of mean flow reversal in the compression wedge interaction at the top wall as well as in the first reflected STBLI at the bottom wall (see the solid white lines in figure 13). Figure 15 shows contours of the mean streamwise skin friction coefficient, $\overline{C}_f$, and the wall pressure, $\overline{p}_w$, mapped on the bottom wall for the simulation with sidewalls; the mean separation line at the first STBLI interaction is also shown, along with isolines of the mean wall pressure. Note how the isolines of the wall pressure are almost two-dimensional upstream of the interaction (showing some curvature only near the corners as a result of secondary flows). Further downstream, the isolines of the wall pressure become more three-dimensional, particularly at the interactions. The mean separation line is located upstream of the region of maximum pressure, and is also highly three-dimensional, with a spanwise extent of approximately $3\delta_o$, representing slightly over a third of the width of the duct. The separation bubble reduces its streamwise extent away from the centreline. The lack of spanwise perfect symmetry of the separation line with respect to the centre plane of the duct is probably a consequence of the slow convergence of the statistics for this region of low-speed flow.

Figure 16(*a*) shows a three-dimensional visualization of the separation bubble on the bottom wall. The Mach stem and the structure of the transmitted and reflected shocks of that STBLI are also shown, along with the bottom wall (coloured by mean pressure) and the vertical plane at the centre of the duct ($z/\delta_o = 4.4$), coloured by

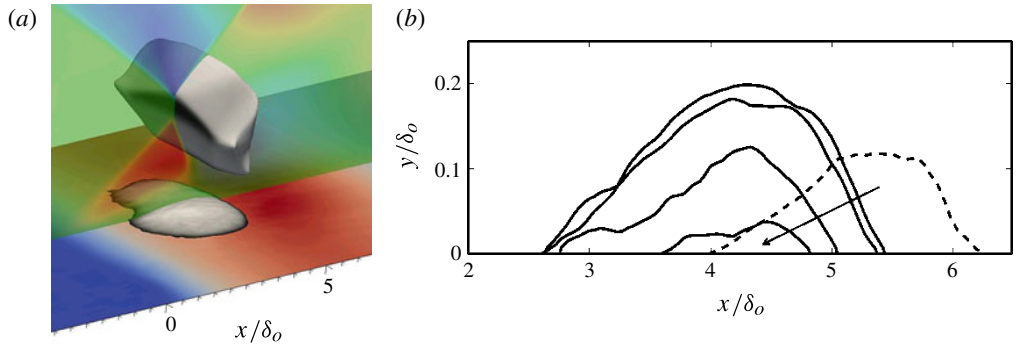

FIGURE 16. (*a*) A 3D visualization near the first STBLI at the bottom wall for the 5 mm-high wedge simulation, showing the separation bubble (the isosurface of zero mean streamwise velocity coloured by vertical Reynolds stress, $\sqrt{\overline{v'v'}}/U_o$ from 0 to 0.1, black to white), the Mach stem with the reflected shocks educed by an isosurface of constant mean density $\overline{\rho}/\rho_o = 2.4$, coloured by mean temperature from $\overline{T}/T_o = 1.37$ to 1.53 (white to black), the centre vertical plane ($z/\delta_o = 4.4$) with isocontours of vertical mean velocity, V/U_o, from -0.2 to 0.2 (blue to green to red, semi-transparent), and the bottom wall (with the full spanwise extent between sidewalls, coloured by mean pressure, $\overline{p}/p_o$ from 1.0 to 2.1, blue to grey to red). (*b*) Isolines of zero mean streamwise velocity (defining the mean separation bubble) for the simulation with sidewalls (solid) on z-normal planes from the centre of the duct towards the sidewall (in the direction of the arrow), and for the spanwise-periodic simulation (dashed line).

mean vertical velocity, for reference. Figure 16(*b*) shows the projection of several slices of the separation bubble on vertical planes normal to the spanwise coordinate, at increasing distance from the centre of the duct. A dashed line corresponding to the mean separation bubble for the spanwise-periodic simulation is also shown for comparison.

Several observations can be made from figure 16(*b*). First, the shape of the separation bubble profiles on the (x, y)-planes is markedly asymmetric, with its maximum height skewed towards downstream locations. From the upstream separation point ($x/\delta_p \approx 2.7$), the separation bubble increases its height, reaching its maximum at $x/\delta_o \approx 4.4$ (corresponding to approximately 60 % of its full streamwise extent), and then dropping more abruptly until the reattachment point is reached at $x/\delta_o \approx 5.4$. This characteristic asymmetric shape (and the approximate location of the maximum height) is shared across the profiles at the different spanwise locations, and will be discussed in relation to the instantaneous flow features in § 3.2.5. A second observation is that the separation bubble for the spanwise-periodic simulation is located approximately δ_o further downstream and is smaller (approximately 20 % shorter streamwise and of almost half the height) than in the simulation with sidewalls, whereas the skewed shape is similar in both simulations. The smaller size found for the spanwise-periodic simulation is consistent with the observations by Priebe *et al.* (2009), Hadjadj *et al.* (2010), Pirozzoli *et al.* (2010), Pirozzoli & Bernardini (2011) and Morgan *et al.* (2013), who found an under-prediction of the streamwise separation length when comparing spanwise-periodic simulation results with experiments. Those previous experiments (see, e.g., Dussauge *et al.* 2006; Piponniau *et al.* 2009) present some differences compared with the ones that are the object of our present simulations: the aspect ratio of the wind tunnel cross-section was larger, the relative size of the

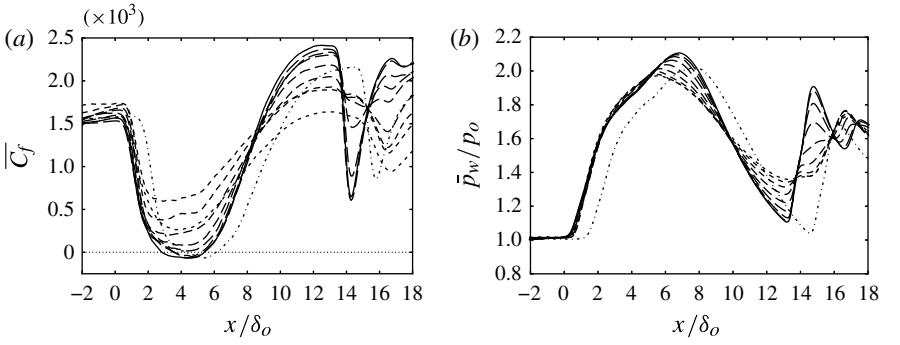

FIGURE 17. Profiles of the time-averaged streamwise skin friction coefficient $\overline{C}_f$ (*a*), and the wall pressure $\bar{p}_w$ (*b*), along the bottom wall, for the 5 mm-high wedge simulation with sidewalls: solid line, centre plane ($z/\delta_o = 4.4$); dashed lines of decreasing dash length correspond to decreasing distance to the sidewall ($z/\delta_o = 3.85$, 3.32, 2.79, 2.25, 1.72, 1.19, 0.66, 0.13). The spanwise-averaged profiles retrieved from the spanwise-periodic simulation are plotted in dash–dotted lines for comparison.

incoming boundary layers was smaller with respect to the cross-section dimensions and the shock generator was placed in the free stream. As a consequence, the resulting incident shock angle and the strength of the interaction were also different and a Mach stem was not observed. However, despite these differences between experiments, similar confinement effects are observed regarding the increased interaction size and strength, as well as a larger separation bubble, resulting from the inclusion of sidewalls versus considering a spanwise-periodic simulation. This is confirmed in the Appendix, which replicates the stronger-interaction case of Piponniau *et al.* (2009).

Figure 17 shows streamwise profiles of the mean streamwise skin friction coefficient, $\overline{C}_f$, and the wall pressure, $\bar{p}_w$, obtained on the bottom wall at several planes normal to the spanwise direction. Profiles for the spanwise-periodic simulation are also plotted in dash–dotted lines. Compared with the first STBLI, the second interaction on the bottom wall shows a slightly larger drop in streamwise skin friction coefficient near the centre plane of the duct, as a consequence of the larger wall pressure gradient experienced: however, the higher value of $\overline{C}_f$ attained downstream of the relaxation zone that follows the first STBLI prevents mean flow reversal from occurring in this second interaction, which occupies a shorter streamwise length. The profiles of streamwise skin friction coefficient largely vary with the spanwise location along the whole streamwise domain plotted, whereas the profiles of mean wall pressure practically overlap for locations upstream of $x/\delta_o \approx 5$, indicating an almost two-dimensional character of the wall pressure in that region. The expansion fan that propagates from the apex of the compression wedge on the top wall reaches the bottom wall and results in a favourable pressure gradient that lowers the pressure for $x/\delta_o \gtrsim 5.5$ near the sidewall and $x/\delta_o \gtrsim 7$ near the centre (the discrepancy being due to the lower streamwise velocity found near the sidewall). The local extrema of pressure found at the first and second reflected STBLIs are largest at the centre plane and smooth out as the sidewall is approached. The decreased strength of the expansion fan near the sidewall results in a reduced favourable pressure gradient compared with the centre of the duct. As noted, the streamwise location of the maximum wall pressure at the first STBLI moves upstream (a relative distance of approximately $1.5\delta_o$) from its position on the centre plane to its final location on the

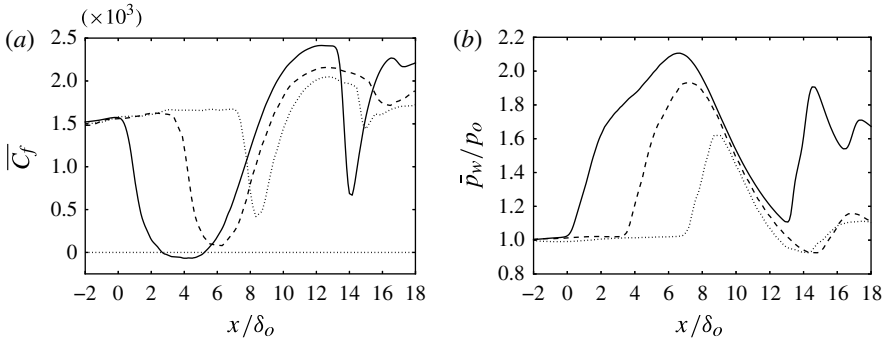

FIGURE 18. Profiles of the time-averaged streamwise skin friction coefficient $\overline{C}_f$ (*a*), and the wall pressure $\overline{p}_w$ (*b*), along the bottom wall, for the 1.1 mm- (dotted), 3 mm- (dashed) and 5 mm-high (solid) wedge simulations with sidewalls at the duct centre plane ($z/\delta_o = 4.4$).

nearest plane to the sidewall plotted. In contrast, the minimum reached immediately upstream of the second STBLI stays at almost the same streamwise location for all the spanwise planes considered. Downstream of the second STBLI, the local extrema of the profiles at the centre and nearest-sidewall plane are in opposite phase. For the spanwise-periodic simulation (dash–dotted lines), the main difference is the downstream displacement of the STBLIs, as already pointed out. The maximum values of the streamwise skin friction coefficient and the mean wall pressure reached downstream of the first STBLI are noticeably smaller than in the simulation with sidewalls. The length of the relaxation zone downstream of the first STBLI is longer for the spanwise-periodic case and, as a consequence, the pressure drops to a lower value before encountering the second STBLI, for which the pressure gradient is slightly lower than in the simulation with sidewalls, thus resulting in a smaller drop of the streamwise skin friction coefficient. Both simulations (with and without sidewalls) show a similar shape for the initial rise of the wall pressure at the first interaction, consisting of a steeper almost-linear part upstream followed by a gradual decrease of the slope (i.e. a lowering pressure gradient) and another shallower, almost-linear part until the maximum is reached.

Figure 18 shows a comparison of the streamwise profiles at the centre plane ($z/\delta_o = 4.4$) of the time-averaged streamwise skin friction coefficient $\overline{C}_f$ and wall pressure for the simulations with the three wedge heights considered in this study (the three of them including sidewalls). The shape of the $\overline{C}_f$ profiles at the first STBLI is similar for the three cases, even though the streamwise location and extent largely varies (moving upstream and occupying a larger region for increasing wedge height). The 5 mm-high wedge case is the only one among the three with mean flow reversal predicted by the negative values of the streamwise friction coefficient. Even though the 3 mm-high wedge case shows a small region of flow separation in the velocity flow field, as explained in § 3.1.1, this region is located below the exchange location of the wall model, and therefore it is not captured by the streamwise friction coefficient shown in figure 18. The value of the streamwise skin friction coefficient reached downstream of the relaxation zone of the first STBLI increases monotonically with the strength of the interaction, even though the observed increase is larger between the 3 mm and 5 mm heights than between the 1.1 mm and 3 mm, respectively.

The wall pressure profiles in figure 18(*b*) show, as expected, a monotonic increase of the pressure jump at the first STBLI for increasing shock strength (i.e. a larger

wedge height). However, the shape of the profiles changes with the shock strength: an almost-linear pressure rise is observed in the 1.1 mm-high wedge case, until it is rounded near the pressure peak at $\overline{p}/p_o \approx 1.62$, whereas the 3 mm and 5 mm-high wedge cases show the two-slope behaviour described earlier for the strongest interaction case. The pressure gradient in the initial linear part of the profile is almost identical among the three cases, in agreement with the theory of free interaction (Chapman, Kuehn & Larson 1957), which states, for steady TBLs, that the pressure distribution up to the point of separation is independent of the mode of inducing separation (in this case, the variation in the shock strength induced by a larger compression wedge). The change in slope begins for the 3 and 5 mm-high wedge cases above $\overline{p}_w/p_o \approx 1.7$, and continues until reaching their maximum pressure levels of $\overline{p}/p_o \approx 1.94$ and 2.12, respectively.

The favourable pressure gradient seen in the relaxation zone downstream of the first STBLI results from the interaction with the expansion fan that propagates from the apex of the compression wedge. This favourable pressure gradient is practically identical for the three wedge heights, but starts further upstream for stronger interactions, since the apex of the compression wedge is closer to the bottom wall (owing to the taller and longer wedge, for the same wedge angle).

The presence of three inflection points in the wall pressure distribution has been linked in the literature with incipient separation (see, e.g., Kuehn 1959; Green 1970). The results found in the present study appear to be consistent with such an argument, as three inflection points only appear in the pressure profiles of the 3 and 5 mm-high wedges (note that no mean flow reversal occurs for the 1 mm-high wedge case). The second inflection point in the pressure profile of the 5 mm-high wedge case forms slightly upstream of the mean separation point at the centre plane. Closer to the sidewalls, the flow on the bottom wall is far from even incipient separation, but the two-slope behaviour of the pressure profiles remains, as explained above. This seems to indicate that the presence of a region of mean flow reversal is enough to preserve the three-inflection-point character of the wall pressure profiles across the span of the duct.

The second STBLI is comparatively much stronger in the 5 mm-high wedge case than in the other two cases. In fact, the behaviour of the second interaction with the wedge height is non-monotonic, probably resulting from the interference with the reflected shocks on the top and sidewalls, as well as with corner shocks: as can be seen in figure 18 for the streamwise skin friction coefficient (at $x/\delta_o \approx 16$), the 1.1 mm-high wedge case shows a location and strength for the second STBLI that are closer to the 5 mm-high wedge case than the 3 mm-high wedge case.

3.2.4. *Secondary flows*

Next, we investigate the flow patterns found in transverse planes resulting from the three-dimensionality of the flow. First, we analyse these secondary flows on the large scales (comparable with the dimensions of the duct). Later, we focus on the turbulent secondary flows that develop along the bottom-wall boundary layer, near one corner of the duct, and consider the downstream evolution as the secondary flows interact with the shock system.

Figure 19 shows cross-sectional (y, z)-planes taken at several streamwise locations of the computational domain, and a horizontal (x, z)-plane taken $0.1\delta_o$ above the bottom wall. The flow patterns are highlighted through in-plane streamlines calculated from the mean velocity components and superimposed on contours of the cross-sectional Reynolds stress, $\overline{v'w'}$. Only large-scale motions are represented in figure 19, since the

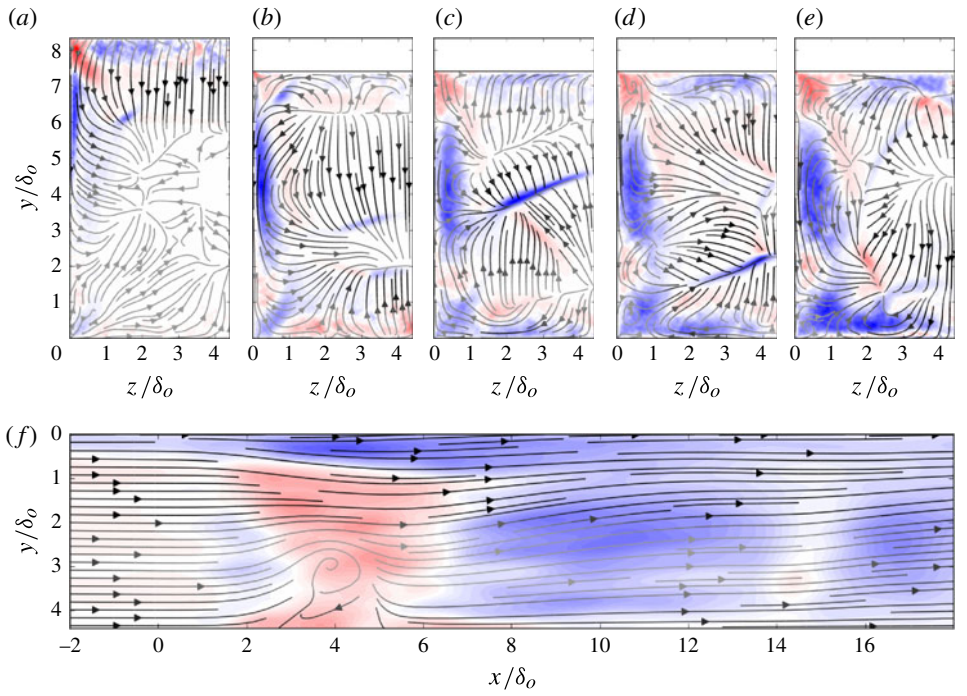

FIGURE 19. Contours of the cross-sectional Reynolds stress ($\overline{v'w'}$) on vertical (y, z)-planes at streamwise locations $x/\delta_o = 0$, 4.1, 9.6, 12.2 and 14.6 (plots *a–e*, respectively) and on a horizontal (x, z)-plane at $y/\delta_o = 0.1$ (plot *f*). Streamlines from mean in-plane velocities are superimposed, with arrows pointing in the flow direction within the plane. Only half the domain is represented in each plot: the flow patterns are symmetric with respect to the spanwise-normal centre plane ($z/\delta_o = 4.4$), whereas $\overline{v'w'}$ is antisymmetric. The colour map of $\overline{v'w'}$ runs from blue (minimum) to white (zero) to red (maximum). The colour map of streamlines indicates the relative magnitude of the in-plane velocity, from grey (minimum) to black (maximum). Each plot has its colour maps normalized for the plane that it represents.

data have been downsampled to draw the streamlines with enough spacing for clarity. The relative magnitude of the in-plane mean velocity for each plot is represented by the local intensity of the streamlines (black being the highest velocity, and fading to grey for slower flow).

The height of the horizontal plane represented in figure 19(*f*) is chosen to visualize the recirculation pattern found inside the separation bubble. This pattern resembles those found experimentally through oil-flow visualizations (for example, see figure 6 in Dussauge *et al.* 2006, even though the shape of the separation bubble differs). At $(x/\delta_o, z/\delta_o) \approx (4, 3)$, a spiralling streamline can be identified. This indicates the presence of a pair (by symmetry) of near-wall counter-rotating, tornado-like vortices located at the spanwise extrema of the separated region. The traces of these vortices on the bottom wall (see Délery, Marvin & Reshotko 1986; Babinsky & Harvey 2011) are foci of the skin friction vector, a key feature of three-dimensional separated flows according to critical point theory (see Tobak & Peake 1982, and references therein).

A region with a high magnitude of $\overline{v'w'}$ is visible (in red) near the first STBLI on that horizontal plane. This region extends laterally towards the sidewall, first

decreasing its streamwise extent with respect to the centre of the duct across the separation bubble, and then increasing in size towards the sidewall. On the sidewall boundary layer, a high magnitude of $\overline{v'w'}$ is also observed in the first STBLI (centred around $x/\delta_o \approx 4$), but with the opposite sign compared with outside the sidewall boundary layer. The thickening of this sidewall boundary layer produced by the interaction is also noticed in the deflection of the streamlines away from the wall. The maximum thickness of this sidewall boundary layer on that plane is reached at $x/\delta_o \approx 6$, followed downstream by a relaxation where the magnitude of $\overline{v'w'}$ decreases inside the boundary layer. Away from the sidewall, moving downstream from the first STBLI, the $\overline{v'w'}$ also changes sign in the relaxation region ($x/\delta_o \gtrsim 7$), almost vanishing at the second STBLI on the bottom wall ($x/\delta_o \approx 14$), and recovering its magnitude again in the subsequent relaxation zone.

Looking at the cross-sectional (y, z)-planes, the dominant downward motion imposed by the two-dimensional compression wedge is seen in figure 19(*a*), corresponding to the wedge foot streamwise location. The effect of the sidewall is noticeable in its vicinity ($z/\delta_o \lesssim 1.5$) by the curvature of the streamlines as well as by the development of regions of high magnitude of $\overline{v'w'}$: a positive region (in red) extending diagonally away from the corner; a negative region (in blue) corresponding to the corner shock at $(y, z)/\delta_o \approx (1.5, 6)$; and, finally, an elongated negative region within the sidewall boundary layer. The latter extends downward following the motion of the shock as it propagates downstream, as seen in figure 19(*b*), where the additional corner shock emanating from this end of the compression wedge can be identified by the negative $\overline{v'w'}$ visible at $(y, z)/\delta_o \approx (1, 6.5)$. A multi-cell flow pattern appears near the top wall. Elsewhere, the transverse flow appears to be directed towards the region in the wake of the Mach stem (located in the duct core at $y/\delta_o \approx 2$–3). On the bottom wall, near the centre of the duct, the flow is clearly pushed upwards by the reflected STBLI; towards the bottom left-hand corner, the downward motion imposed by the incident shock is still dominant and the flow turns counterclockwise as it encounters the bottom-wall boundary layer. This will be seen better when the evolution of the flow inside that corner is described below. This flow pattern near the bottom wall is inverted further downstream (see figure 19*c* corresponding to the relaxation region of the first STBLI on the bottom wall). As the sidewall boundary layers grow, noticeable due to the thickening of the near-wall regions of negative $\overline{v'w'}$ in figure 19(*c–e*), the three-dimensionality of the cross-sectional flow patterns also becomes dominant in the core of the duct, from the diagonal motions imposed by the inclined reflected shocks (marked by the sharp regions of negative $\overline{v'w'}$ in blue seen in figure 19*c*,*d*).

Besides the large-scale and complex transverse flow patterns outlined above, more subtle secondary motions can be found inside the TBLs. The two kinds of turbulent secondary flows originally identified by Prandtl are present in the flow under consideration: the first kind is produced by the lateral deflection of a TBL (for example, by a spanwise pressure gradient, such as the one found near the separation bubble or near the sidewalls of the duct in the vicinity of the STBLI); the second kind originates from gradients of Reynolds stresses in transverse directions, such as those experienced near the intersection of solid walls (corners flows). Both kinds of secondary flow have their origin in the generation of streamwise mean vorticity. Attending to their different generating mechanism, Bradshaw (1987) renamed them as skew- or stress-induced, respectively. In what follows, we focus our attention on the latter.

Figure 20 shows the downstream evolution of the corner flows developed near the intersection of the bottom and left duct walls, through cross-sectional planes taken

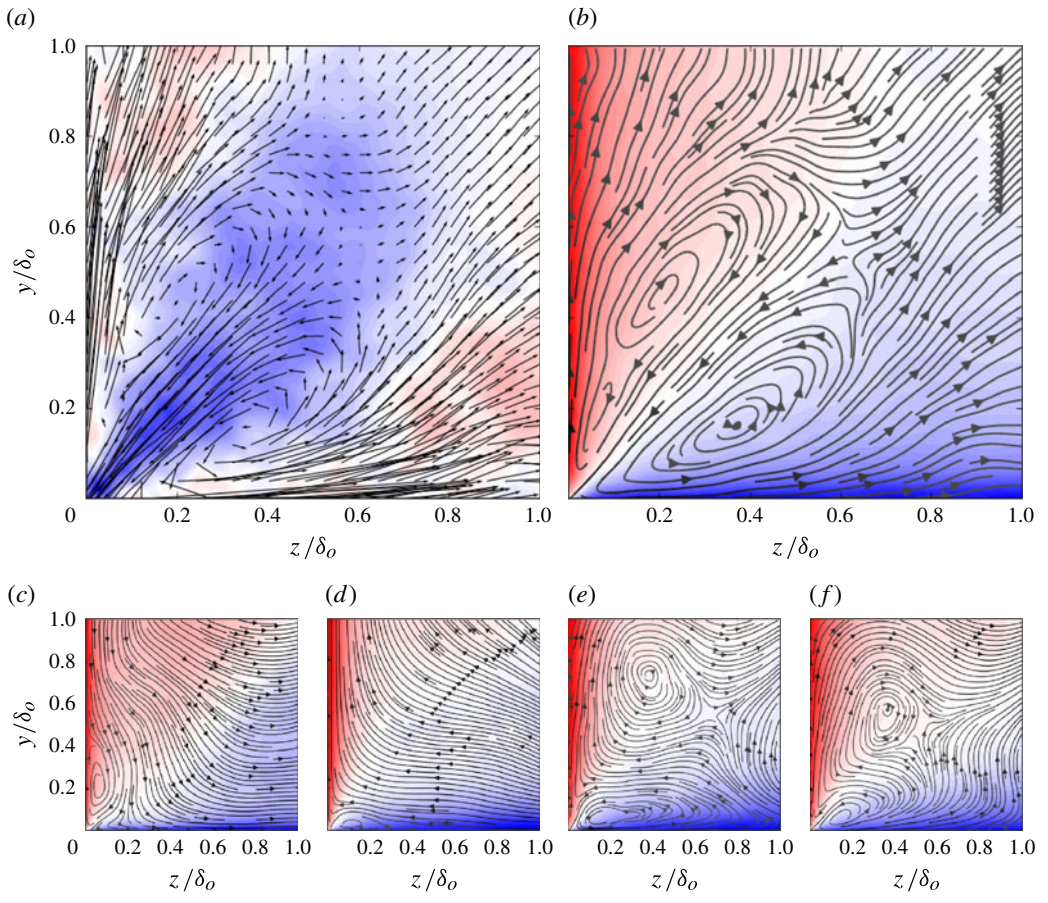

FIGURE 20. The downstream evolution of secondary flows near the corner at the intersection of the bottom and left duct walls, from cross-sectional planes taken at $x/\delta_o =$ 0 (*a*,*b*), 4.1 (*c*), 9.6 (*d*), 12.2 (*e*) and 14.6 (*f*). Contours of $\overline{v'w'}$ are shown in (*a*), whereas (*b–f*) show contours of $\overline{v'v'} - \overline{w'w'}$. Streamlines from mean in-plane velocities are superimposed, with arrows pointing in the flow direction within the plane. The colour map of $\overline{v'w'}$ and $\overline{v'v'} - \overline{w'w'}$ runs from blue (minimum) to white (zero) to red (maximum). The colour map of streamlines, from grey to black, indicates the relative magnitude of the in-plane velocity. Each plot has its colour maps normalized.

at the same streamwise locations as presented earlier in figure 19. Upstream of the first STBLI (figure 20*a*,*b*), an almost symmetric pair of counter-rotating vortices is observed. This qualitatively agrees with experiments by Davis, Gessner & Kerlick (1986), Gessner, Ferguson & Lo (1987) and Davis & Gessner (1989), in which the cell structure of corner flows in supersonic cases was found to be similar to its incompressible counterpart. The maximum transverse velocity magnitude at that upstream, unperturbed location is $0.026U_o$, consistent with the $\leqslant 0.03$ values found for the supersonic flow in a square duct experiment by Davis & Gessner (1989) and also in previous studies for incompressible flow. From the transport equation for the mean streamwise vorticity in incompressible flow (see Bradshaw 1987), the dominant terms in the development of these corner flows are the gradients of the cross-plane shear stress, $\overline{v'w'}$, and of the difference between the vertical and spanwise-normal

Reynolds stresses, $\overline{v'v'} - \overline{w'w'}$. These quantities are plotted in figures 20(*a*) and 20(*b*), respectively, along with the streamlines obtained from the cross-sectional mean velocity components, and the arrows representing the corresponding transverse mean velocity vectors. The flow is accelerated along the bisector towards the corner, where the minimum cross-plane shear stress is reached, consistent with the DNS results of Huser & Biringen (1993) and Joung, Choi & Choi (2007). From the corner, the flow is ejected away along each wall. Figure 20(*c*) corresponds to a streamwise location inside the first STBLI ($x/\delta = 4.1$). The downward motion imposed by the incident shock along the sidewall boundary layer at this location breaks the symmetry of the original counter-rotating vortex pair, so that only the vortex near the sidewall remains, which is moved closer to the corner. The flow is directed downward and deflected along the bottom wall towards the centre of the duct. The locus of $\overline{v'v'} - \overline{w'w'} = 0$, which coincided with the bisector in the unperturbed location, is now curved and roughly follows a path perpendicular to the in-plane streamlines. In figure 20(*d*), corresponding to a location within the relaxation zone downstream of the first STBLI ($x/\delta_o \approx 9.6$), the opposite patterns develops: the cross-sectional flow is directed towards the sidewall along the bottom wall and deflected upwards, with a vortex near the corner on the bottom wall, and the locus of $\overline{v'v'} - \overline{w'w'} = 0$ curved towards the sidewall. A counter-rotating vortex pair configuration is recovered further downstream in the relaxation zone (see figures 20(*e*) and 20(*f*), corresponding to streamwise locations $x/\delta_o = 12.2$ and 14.6, respectively), even though the cell structure is no longer symmetric with respect to the bisector: the upper vortex appears to be lifted away from both walls with an almost circular shape, whereas the lower vortex is closer to the corner and stretches along the bottom wall.

3.2.5. *Instantaneous flow structure and time evolution*

We now focus on the instantaneous organization of the flow features as well as their evolution in time, emphasizing the three-dimensionality contributed by the sidewalls. As noted by Humble, Scarano & van Oudheusden (2009*b*) in their visualizations of a reflected STBLI experiment (see figure 3 in that reference), the instantaneous global structure of the interaction changes significantly in time. In the present simulations, similar unsteady changes are observed, as seen in figure 21, which shows a substantial variation in the shapes and sizes not only of the different STBLIs present on the top and bottom walls within the computational domain, but also of the Mach stem and its wake. For example, the extent and intensity of the low-speed and recirculation regions (coloured in light to dark blue tones) found in the compression-wedge interaction on the top wall and in the first reflected STBLI on the bottom wall largely vary between the two time instants shown. A flatter interaction region on the bottom wall is seen in figure 21(*a*), with higher streamwise velocities than in figure 21(*d*), for which a stronger, taller and more localized separation is seen, extending closer to the transmitted shock. At the time of the locally stronger separation region observed on the z-normal plane shown in figure 21(*d*), the vertical extent of the Mach stem shrinks. Views of the Mach stem on the cross-sectional planes shown in figure 21(*b*,*e*) confirm the thinning of the aforementioned lenticular shape of the Mach stem. A spanwise decrease in size is also seen in those planes and further confirmed by the horizontal views shown in figure 21(*c*,*f*), from which a narrower wake immediately downstream of the Mach stem is also observed. Note how the λ structure of the reflected STBLIs on the sidewalls is also modified between the two times, in relation to the different shape of the interaction regions (this is particularly noticeable on the right sidewall, which corresponds to $z/\delta_o = 8.8$). Despite changes in the shape and size of the Mach

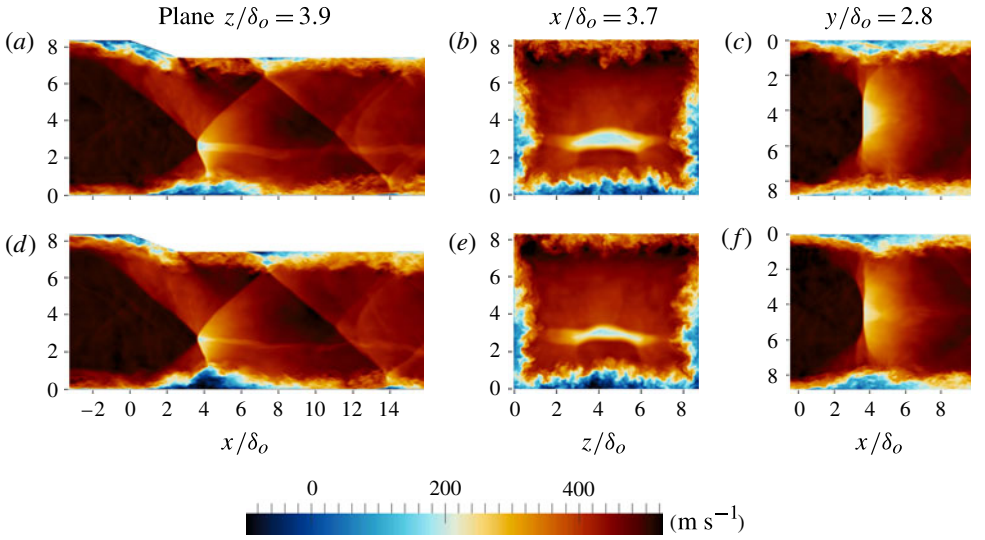

FIGURE 21. Instantaneous streamwise velocity contours at two uncorrelated time steps (top and bottom) on coincident planes normal to z (a,d), x (b,e) and y (c,f). All planes pass through the Mach stem.

stem, its streamwise location appears practically unaltered between the two time steps considered. These unsteady variations appear to be manifestations of a close interplay between the breathing motion of the instantaneous separation regions in the boundary layers, the beating of the Mach stem and the fluttering of the corner shocks. A final remark from figure 21(b,e) is the confirmation of the deeper penetration of regions of higher streamwise velocity also found instantaneously near all corners of the duct, as a consequence of the mean secondary turbulent flows described in § 3.2.4.

From their experimental study of a reflected STBLI, Humble *et al.* (2009*b*) suggested that, as the interaction is approached, vortical structures are lifted away from the wall, riding above the separation bubble (seen as an obstacle) and creating a fluid exchange between the inner and outer layers of the interaction. In figure 22, we present a time sequence of a lifting event found in the first reflected STBLI at the bottom wall of the present simulations: low-speed fluid from the incoming boundary layer is lifted as it enters the interaction at the foot of the separation shock. As the low-speed fluid pocket rises and propagates downstream towards the transmitted shock, high-speed fluid is trapped between two layers of low-speed fluid. Downstream of the transmitted shock, the tip of the low-speed fluid patch appears to be shed into the downstream flow, accelerated by the surrounding, faster fluid. While only vertical slices are shown in figure 22, the three-dimensional local structure of the boundary layer as it traverses the interaction will play a significant role in these lifting events (Humble *et al.* 2009*a*).

It is expected that the secondary STBLIs resulting from subsequent shock reflections on the top and bottom walls of the duct will show an even more marked unsteady character, due to the amplified level of turbulence contained in their incoming boundary layers from prior interactions, and to the comparatively weaker incident shocks that they encounter. Figure 23 shows the instantaneous shock structure near the second STBLI at the bottom wall ($x/\delta_o \approx 14$) by contours of dilatation on the centre plane, where the interaction is strongest. The foot of the incident shock (R')

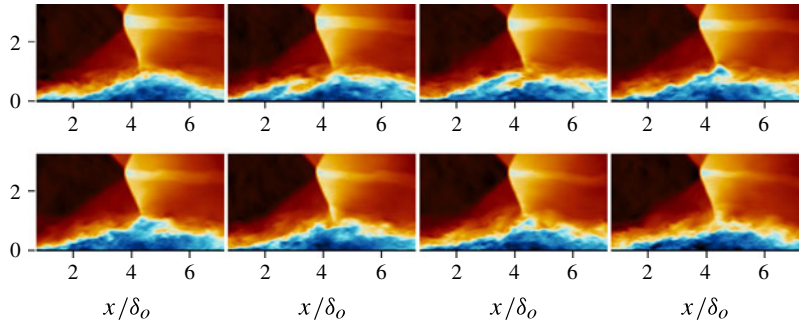

FIGURE 22. The time sequence (from left to right, and top to bottom) of the upward ejection of a low-speed fluid pocket formed at the foot of the separation shock as it traverses the first STBLI at the bottom wall on the centre plane. Subsequent snapshots are equispaced in time $1.5\delta_o/U_o$, resulting in a total duration of the sequence of $12\delta_o/U_o$. See figure 21 for the corresponding colour bar.

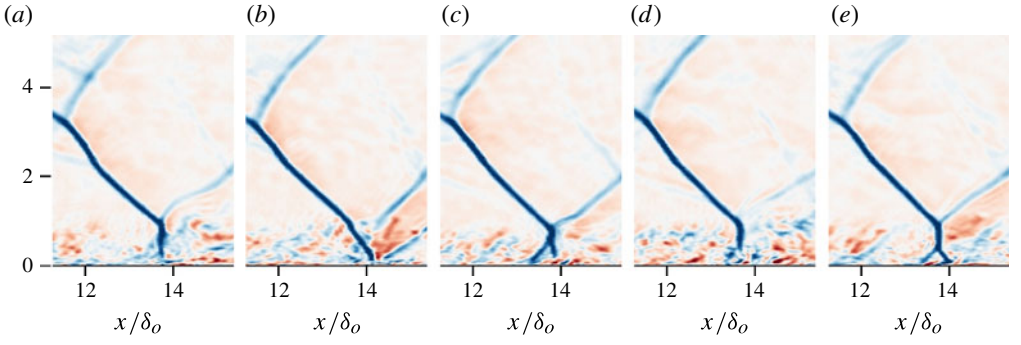

FIGURE 23. Instantaneous dilatation contours on the centre plane ($z/\delta_o = 4.4$) zoomed on the second STBLI on the bottom wall at multiple times (from left to right). See figure 24 for the shared colour map.

is indeed largely unsteady, varying from a quasi-normal shock (figure 23*a*,*d*) to a λ configuration (*c* and *d*) or simply continuing as a oblique shock extending very near the bottom wall (*b*). The reflected shock from this interaction (R'') is weaker (noted by the lighter blue tone of the dilatation contours) and also highly unsteady, showing changes of curvature (compare figure 23*a*,*e*) or locally vanishing (figure 23*d*).

Even though the Mach stem occurs in a region of the flow (near the core of the duct) that contains low levels of turbulence, its wake presents a marked unsteady character. There are two shear layers that develop from the lines of triple shock points (formed at the intersections of the Mach stem with incident and reflected shocks, and with the separation and transmitted shock, respectively). These shear layers can be identified by the generation of spanwise vorticity, as highlighted by instantaneous contours on the centre of the duct presented in figure 24. From a relatively straight development immediately downstream of the Mach stem, Kelvin–Helmholtz instabilities develop in the wake, amplified by the interaction with the perturbations imposed by the expansion fan and the compression waves emanating from the relaxation of the nearby STBLI at the bottom wall. These instabilities curve the instantaneous shear layers and get amplified at their intersection with the reflected

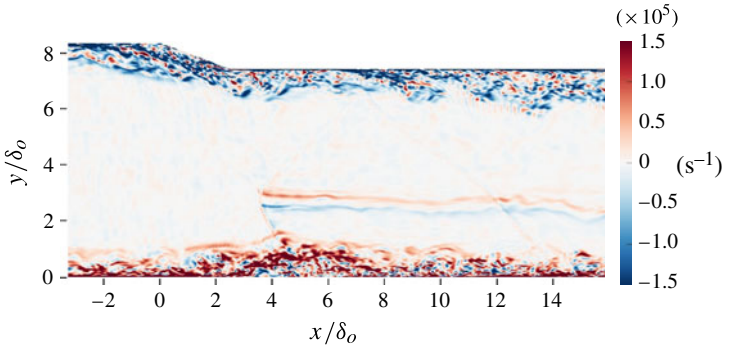

FIGURE 24. Instantaneous spanwise vorticity contours on the centre plane.

shock R' from the top wall at $x/\delta_o \approx 12$. Despite the convoluted shape, the two shear layers remain mostly parallel throughout their downstream evolution.

Contours of the instantaneous zero streamwise skin friction coefficient shown by the black lines in figure 25 for the top, left and bottom walls of the duct reveal patterns of instantaneous flow separation that are substantially different from the time-averaged result shown in figure 15. Focusing on the first STBLIs on the top and bottom walls, for which mean separation exists, instead of a contiguous separation bubble, the overall separation appears broken into smaller, highly corrugated packets, which tend to present more elongated (i.e. finger-like) and disconnected shapes in the most-upstream locations of each interaction, in contrast with wider and often more connected separation packets found further downstream within the interaction zone, suggesting a higher likelihood of mean separation at those streamwise locations. These shape differences may be responsible for the skewness towards downstream locations seen in figure 16(*b*) for the shape of the mean separation bubble, and would also explain the spanwise shape of the mean separation bubble observed in figure 15. Additionally, instantaneous flow reversal is observed in the form of small separation bubbles on the second STBLI of the top wall and also on the sidewall (for example, at $(x, y)/\delta_o \approx (4, 1.5)$).

3.2.6. *Low-frequency unsteadiness*

After highlighting in § 3.2.5 some of the unsteady effects in the instantaneous flow features, we now perform a spectral analysis of such unsteadiness. One of the purposes is to elucidate whether low-frequency motions observed in previous experiments and simulations in the literature concerning STBLIs also exist in the present configuration and, if so, whether they are modified by the confinement effect of the sidewalls.

For the present analysis, we consider both the simulations with sidewalls and the spanwise-periodic simulation. Arrays of probes equispaced $0.185\delta_o$ along the streamwise coordinate are placed on the bottom and top walls, both at the centre plane ($z/\delta_o = 4.4$) and at a near-sidewall plane ($z/\delta_o \approx 0.5$). For the spanwise-periodic simulation, only the centre-plane probes will be considered. Both simulations are run for $t \approx 2000\delta_o/U_o$. The sampling frequency of the probes is $f = 206U_o/\delta_o$. Similarly to Priebe & Martin (2012), power spectra are calculated from the pressure signals at each location, using Welch's method. Eight segments with 50 % overlap are used, combined with a Hann window function applied to every segment, before computing its Fourier transform.

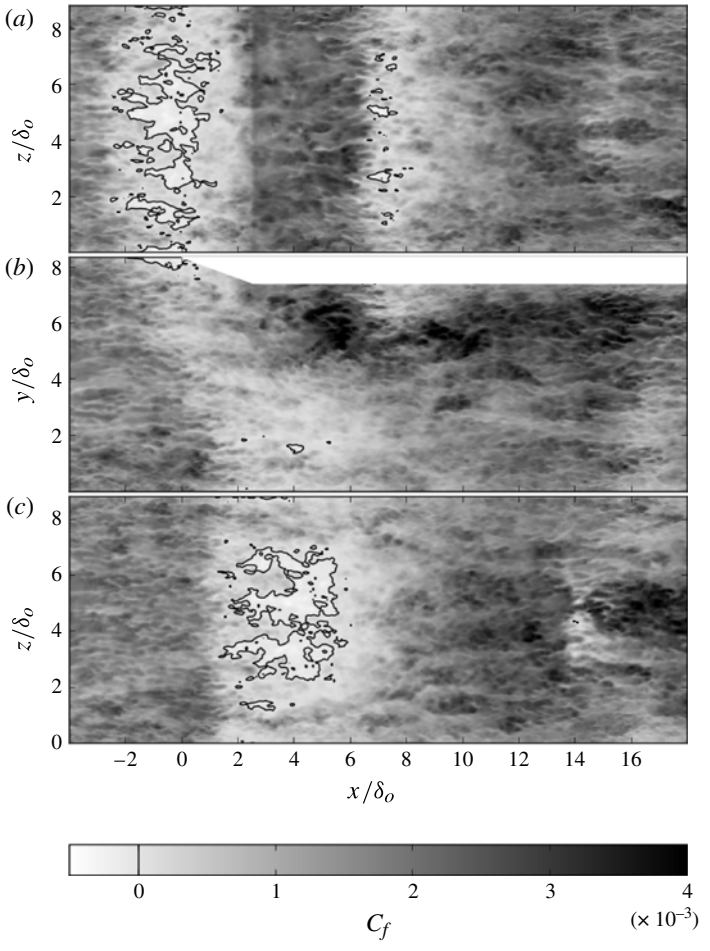

FIGURE 25. Contours of the instantaneous streamwise skin friction coefficient, C_f, on the top (*a*), left (*b*) and bottom (*c*) walls. The superimposed black line represents the locus of instantaneous separation ($C_f = 0$).

Figure 26 shows contours of the premultiplied power spectral density (PSD′) of the bottom-wall pressure signals as a function of the streamwise location and the normalized frequency $f\delta_o/U_o$. The PSD′ at each streamwise location is normalized with its integrated value across all frequencies. Figure 26(*a*,*b*) correspond to the simulation with sidewalls, at spanwise locations of $z/\delta_o = 4.4$ (the centre plane) and $z/\delta_o \approx 0.5$ (the near-sidewall plane), respectively. Figure 26(*c*) shows the centre plane results for the spanwise-periodic simulation. To aid in the explanations that follow, figure 27 shows individual PSD′s at particular streamwise locations from the centre plane corresponding to the simulation with sidewalls. The associated flow features present in those planes for each simulation can be seen in figure 13.

As stated in § 2.2, frequencies $f_o \sim O(U_o/\delta_o)$ are introduced by the synthetic turbulence generator at the inflow, based on the digital filtering technique being used and for the choice of turbulent length scales specified in these simulations. This is verified in figure 26(*a–c*), for which the frequency content of the PSD′s at upstream locations (where the boundary layer is not yet perturbed by the shock) is dominated

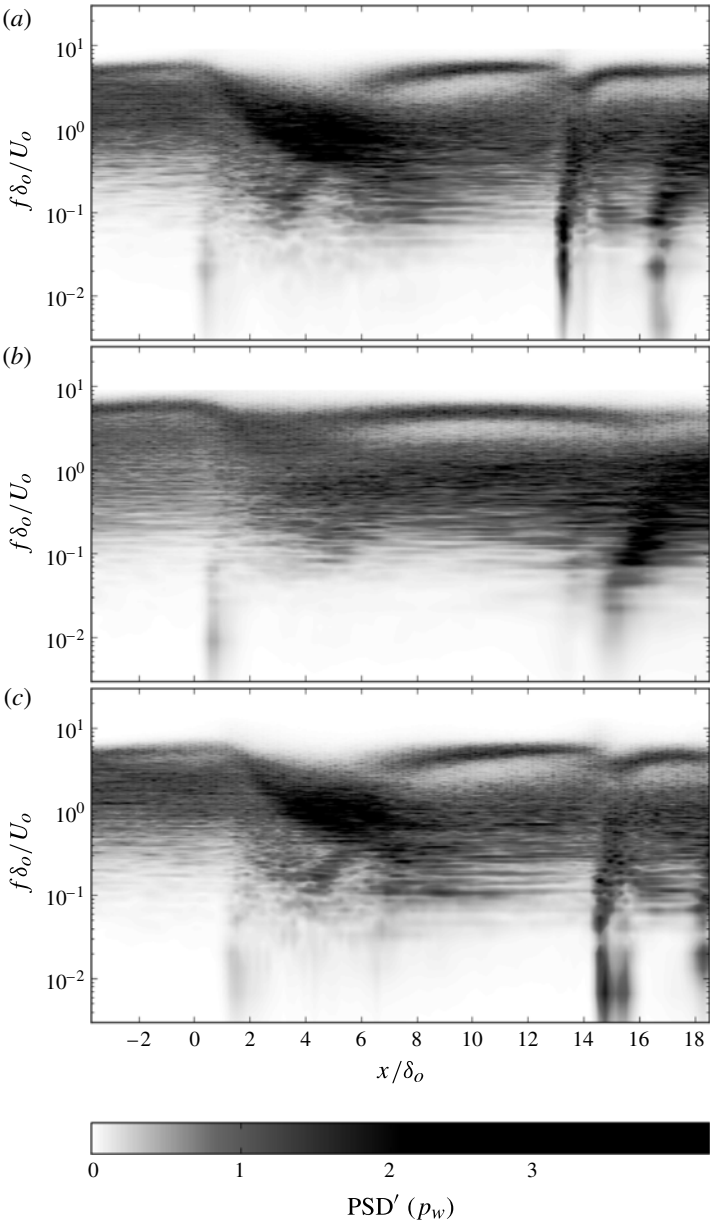

FIGURE 26. Contour maps of the premultiplied power spectral density (PSD′) (arbitrary scale) of the bottom-wall pressure for an array of probes located along the streamwise coordinate: (*a*) centre plane ($z/\delta_o = 4.4$) of simulation with sidewalls, (*b*) near-sidewall plane ($z/\delta_o \approx 0.5$) of simulation with sidewalls, (*c*) centre plane of spanwise-periodic simulation. Here, PSD′s are normalized for each streamwise coordinate location.

by a broadband region around $St = f\delta_o/U_o \approx 1$ (see also figure 27*a*). The adequacy of the digital-filter method in use for inflow turbulence generation to avoid introducing spurious low-frequency signals was assessed in Touber & Sandham (2009*b*).

Near the first STBLI on the bottom wall ($x/\delta_o \approx 2$), regions of low-frequency content are visible in the wall pressure spectra in figure 26(*a–c*), extending to

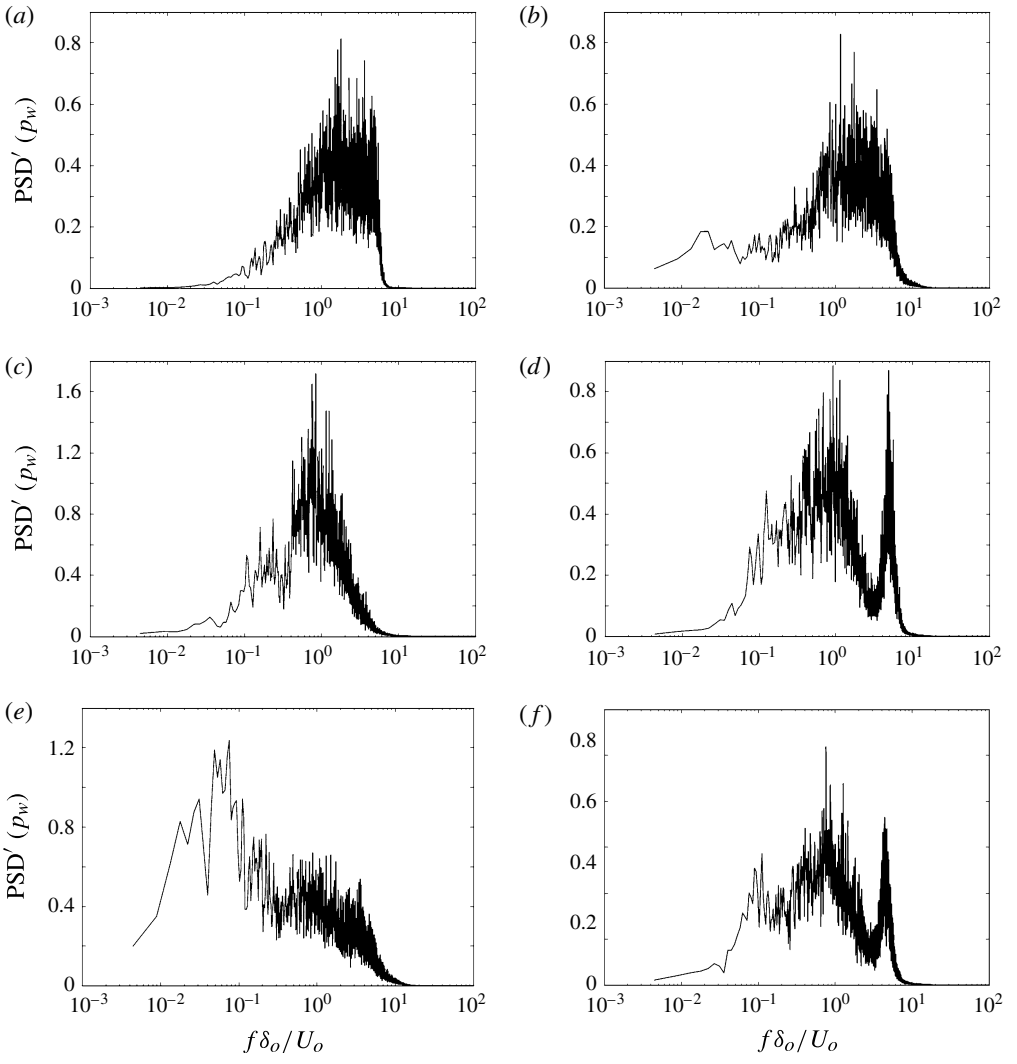

FIGURE 27. The premultiplied power spectral density (PSD′, on an arbitrary scale, normalized for each plot) of the wall pressure signals at different streamwise locations on the bottom wall, at the centre plane of the duct ($z/\delta_o = 4.4$): (*a*) $x/\delta_o = -4$, (*b*) $x/\delta_o = 0.4$, (*c*) $x/\delta_o = 3.8$, (*d*) $x/\delta_o = 9.2$, (*e*) $x/\delta_o = 13.3$, (*f*) $x/\delta_o = 15$.

frequencies below $St \approx 0.1$ and peaking around $St \sim O(0.01)$. At the centre plane of both simulations (figure 26*a*,*c*), the streamwise location where these low-frequency signals are found coincides with the foot of the separation shock, which is located upstream of the mean separation point. The spanwise-periodic simulation shows a downstream shift of the location with low-frequency signals of approximately δ_o, consistent with the delayed position of the first STBLI on that bottom wall compared with the simulation with sidewalls, as discussed in § 3.2.1. The energy contained in this low-frequency range ($St \approx 0.01$–0.1) is small compared with that of the incoming turbulence (at $St \sim O(1)$), as can be seen better in figure 27(*b*), which corresponds to the PSD′ at $x/\delta_o \approx 0.42$ on the centre plane for the simulation with sidewalls: the local maximum for low-frequency content occurs at $St \approx 0.02$. On the near-sidewall

plane, the low-frequency peak corresponding to this first STBLI occurs at a lower frequency ($St \sim 0.008$) than at the centre plane, with a similar relative strength below the dominant higher frequencies of the incoming turbulence.

The observed low-frequency unsteadiness associated with the impinging STBLI on the bottom wall is consistent with previous studies in the literature, both in experiments (see Dolling & Or 1985; Dupont *et al.* 2006; Dussauge *et al.* 2006; Piponniau *et al.* 2009; Ringuette *et al.* 2009) and numerical simulations (see Wu & Martin 2008; Garnier 2009; Touber & Sandham 2009*a*,*b*; Priebe & Martin 2012; Morgan *et al.* 2013). Nevertheless, in the present simulations, the low-frequency peak in the wall pressure spectra at the first STBLI on the bottom wall does not dominate over the frequencies of the incoming TBL. Dussauge *et al.* (2006) found the frequency of shock oscillations, f_s, of several experimental studies to be within 0.02 and 0.05, when a Strouhal number based on the separation length, L_{sep}, was used ($St_L = f_s L_{sep}/U_o$). Presently, the peaks of low-frequency unsteadiness for the simulation with sidewalls are found at $St_L \approx 0.057$ at the centre plane and 0.022 near the sidewall, whereas the spanwise-periodic simulation presents its peak at 0.023.

Moving downstream along the first STBLI, a shift is observed in the spectrum from the characteristic frequencies of the incoming TBL towards lower frequencies: compare, for example, the spectral density in figure 27(*a*), taken upstream of the first interaction (at $x/\delta_o = -4$) with that of figure 27(*c*), taken at a location inside the interaction (at $x/\delta_o = 3.8$). This shift to lower frequencies has also been reported experimentally and in previous simulations. Even though the frequency shift is observed both at the centre plane and near the sidewall, a stronger peak of the spectral density is noticed for probes located in the centre plane (figure 27*a*), whereas a more uniform distribution of the spectral density occurs across the range of frequencies found in probes near the sidewall (figure 27*b*). The spanwise-periodic simulation shows a behaviour inside the first STBLI region similar to that already described for the centre plane of the simulation with sidewalls, the only appreciable difference being the reduced streamwise extent of the region of high-intensity spectral density, as it begins further downstream ($x/\delta_o \approx 3$) than for the simulation with sidewalls ($x/\delta_o \approx 1.5$), ending approximately at the same location in both cases ($x/\delta_o \approx 8$).

In the relaxation zone that follows the first STBLI ($x/\delta_o \approx 8$–12 in the simulation with sidewalls and $x/\delta_o \approx 8$–14 in the spanwise-periodic simulation), a distinctive double-peak structure is observed for the spectral density functions at high frequencies. A representative example is shown in figure 27(*d*): the first, broader peak spans a frequency range of $f\delta_o/U_o \approx 0.4$–$1$, and a narrower peak is located at $f\delta_o/U_o \approx 5$, spanning a range of $\Delta f\delta_o/U_o \approx 2$ around it. Note that although these higher frequencies were mostly present (e.g. figure 27*a*) in the incoming TBL (probably generated near the walls, as the grid is refined to capture smaller eddies), they have been amplified by the STBLI, as will be confirmed in figure 28. This second peak at higher frequencies has been observed in previous experimental studies of the reflected STBLI (Dupont *et al.* 2005; Dussauge *et al.* 2006).

Low-frequency unsteadiness reappears at the second STBLI on the bottom wall (see figure 26), particularly at the centre plane ($x/\delta_o \approx 13$ for the simulation with sidewalls and $x/\delta_o \approx 15$ for the spanwise simulation). The spectral density content at this second STBLI is dominated by such low frequencies ($St \in 0.01$–0.1), suggesting a much stronger unsteadiness than for the first STBLI (compare figure 27*b*,*e*). Near the sidewall, a trace of the low-frequency unsteadiness derived from the second STBLI is captured in the PSD′ at $x/\delta_o \approx 13$ (see figure 26*b*), although its intensity is much weaker than at the centre plane. Note, from figure 14, that the second STBLI on the

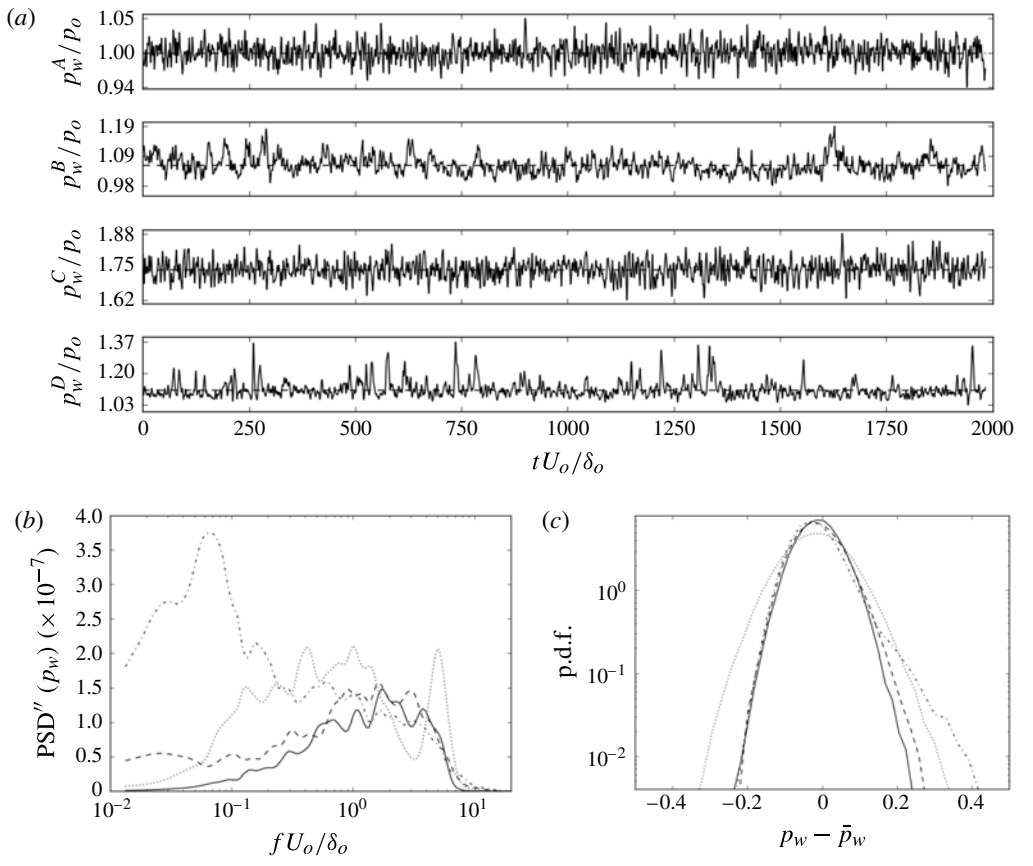

FIGURE 28. (*a*) Bottom-wall pressure signals (solid) and means (dashed) at several streamwise locations at the centre plane of the duct ($z/\delta_o = 4.4$) for the simulation with sidewalls. From top to bottom: $x_A/\delta_o = -4$ (incoming TBL), $x_B/\delta_o = 0.4$ (reflected shock foot of the first STBLI), $x_D/\delta_o = 9.2$ (relaxation zone of the first STBLI) and $x_E/\delta_o = 13.3$ (second STBLI). Pressure signals have been smoothed, for clarity, by convolution with a Hann window kernel spanning $St \approx 4.9$. (*b*) The filtered premultiplied power spectral density (PSD″) without normalization and (*c*) p.d.f.s relative to the mean values of the corresponding raw pressure signals shown in (*a*) using solid, dashed, dotted and dash–dotted lines, respectively.

bottom wall has a narrower spanwise extent compared with the first STBLI, for which the foot of the separation shock spans the full duct. The narrower extent translates into a lesser effect near the wall, compared with the centre plane. However, the curved shock that forms before the second STBLI in the core of the duct ($x/\delta_o \approx 10$) impinges on the sidewalls and near the bottom wall at approximately $x/\delta_o \approx 16$ (see figures 14 and 13*f*), producing a complex STBLI localized at the corner between the side and bottom walls. The foot of its reflected shock is located at $x/\delta_o \approx 15$, where a stronger region of low-frequency content is observed in the spectral density function shown in figure 26(*b*). For the spanwise-periodic simulation (figure 26*c*), the effect of the second STBLI on the bottom wall is clearly visible in the PSD, occurring at $x/\delta_o \approx 15$, consistent with the overall downstream displacement of the shock train observed when spanwise periodicity is considered (figure 12).

Figure 28(*a*) shows the comparison of wall pressure time signals taken at four streamwise locations along the centre plane of the duct: probe A is located upstream of the interaction ($x/\delta_o = -4$), probe B is at the foot of the reflected shock of the first STBLI ($x/\delta_o = 0.4$), probe D is within the relaxation zone of the first STBLI ($x/\delta_o = 9.2$) and probe E is at the second STBLI ($x/\delta_o = 13.3$). These probes coincide with those used in figure 27(*a*,*b*,*d*,*e*), but each signal has been filtered to remove high-frequency content by convolving them with a Hann window function kernel of width $St \approx 4.9$. The corresponding premultiplied power spectral density functions of the raw (unfiltered) signals are plotted in figure 28(*b*). These plots differ from figure 27 in that they are not normalized at each location, so that the relative amplification of the signal in each frequency range can be compared. However, the spectra have been filtered to remove the highly oscillatory character shown in figure 27(*a*,*b*,*d*,*e*), so that a direct comparison of the four curves can be made.

Figure 28(*c*) shows the p.d.f. of each (unfiltered) wall pressure signal (with respect to its mean value). The incoming boundary layer shows a symmetric p.d.f. The symmetry is lost at the foot of the separation shock in the first STBLI, as seen primarily by the right tail of the p.d.f. departing from its original shape. In the relaxation zone, the symmetry of the p.d.f. is recovered, and the only appreciable difference in the p.d.f. with respect to its counterpart at the incoming boundary layer is a larger standard deviation, resulting from larger pressure fluctuations due to the turbulence amplification across the shock. For the last probe, located at the second STBLI, the mean pressure level (and fluctuations) have recovered values comparable to the incoming boundary layer (see the ranges of the vertical axes on figure 28*a*), but the right tail of its corresponding p.d.f. is biased towards larger pressure fluctuations. This can also be inferred from a visual comparison among the four time signals shown in figure 28(*a*) where the second and fourth signals show larger departures from the mean towards higher pressures than towards lower ones, compared with the first and third signals. These high-pressure events appear more sporadically (i.e. separated by longer time scales). The peaks of low-frequency unsteadiness associated with probes B (at the first STBLI) and E (at the second STBLI) occur at different frequencies (see figure 28*b*). The first interaction presents a local maximum at $St \approx 0.02$, whereas the second interaction shows two different local peaks: a dominant one at $St \approx 0.08$ and a secondary one at $St \approx 0.02$–0.03. Likewise, the low-frequency motions found at the centre and near the sidewalls present peaks at different frequencies, as already mentioned above for the first STBLI. Whereas a bimodal p.d.f. of the wall pressure signal near the foot of the separated region has been observed in prior studies, the signals analysed in the present work do not show a bimodal character. Previous experiments have reported similar results, in the sense of an absence of bimodal wall pressure signals (see, e.g., Garg & Settles 1996; Gibson & Dolling 1991, for which the p.d.f.s of pressure signals 'were found to be essentially Gaussian throughout the so-called intermittent region'), although the cause was attributed to a limited spatial resolution and too large spacing ($O(\delta_o)$) between adjacent pressure transducers used in the experiments. The streamwise spacing between adjacent pressure probes in the present simulations is much shorter ($0.185\delta_o$), and the reason why such a bimodal character is not present in the analysed signals and in those corresponding to their adjacent probes (not shown) is not known.

To investigate the possible linear coupling of low-frequency motions corresponding to subsequent STBLIs throughout the duct, we analysed the statistical spectral coherence between pairs of wall pressure signals that show significant peaks of low frequency, for simulations with and without sidewalls independently. Only pairs

of signals that were spatially close, belonging to the same interaction, resulted in significant coherence, as found in previous studies of isolated interactions. Signals taken from pairs of consecutive STBLIs (including those occurring at the top wall, for which low-frequency unsteadiness was also found) did not show relevant levels of coherence as we sought, and nor did the probes corresponding to the same interaction on the centre and near-sidewall planes, for the simulation with sidewalls. This suggests that any coupling between low-frequency motions associated with subsequent STBLIs in the present shock train will probably be nonlinear.

4. Conclusions

In this work, we first assessed the feasibility of WMLES to reproduce the flow features resulting from the interaction of shock waves of varying strength and the TBLs that develop inside a low aspect ratio duct configuration, for which the sidewalls impose significant spanwise variation of the flow. An initial validation of the simulation methodology was done by direct comparison with PIV measurements of the targeted experiment by Helmer *et al.* (2012), extended to a larger compression wedge that generates the shock train inside the duct. Reasonable agreement was found between simulations and experiments, both qualitatively and quantitatively, in spanwise-normal planes near the centre of the duct and near the sidewalls, where experimental measurements were available. Despite the relative simplicity of the equilibrium wall model used in the current simulations, the results suggest that non-equilibrium effects can still be accurately reproduced in the simulations for the flow regime and shock intensities under consideration. Such non-equilibrium effects include adverse pressure gradients found near the STBLIs and turbulent secondary flows developed along the duct corners. While the simplified boundary layer equations solved by the wall model do not account for those non-equilibrium effects, the fact that the wall model is only applied in less than 10 % of the boundary layer implies that such non-equilibrium effects are mostly dominant in the outer layer of the TBL and, therefore, can be accurately captured by the LES solution, entering into the wall-model calculation through the upper boundary condition imposed at the exchange location between the outer (LES) and inner (wall-model) grids.

After the initial validation, additional simulations were pursued with a stronger interaction generated by a larger compression wedge that resulted in a larger region of mean flow reversal. The purpose of these simulations was to explore the physics of the multiple STBLIs found inside the computational domain mainly from the standpoint of the three-dimensional effects imposed by the confinement resulting from the presence of the sidewalls. To that effect, we performed simulations with sidewalls and without them (i.e. spanwise-periodic) for comparison.

The most noticeable effect of the sidewalls in the mean flow for the present configuration was to produce a singular shock intersection (i.e. Mach stem) at the first reflected STBLI. In contrast, the spanwise-periodic simulation showed a regular shock intersection, resulting in the whole shock system being pushed downstream with respect to the simulation with sidewalls. For the latter, the Mach stem is confined to the core of the duct and generates a subsonic wake that propagates downstream and accelerates again to supersonic speeds, interacting with the subsequent reflected shocks. A deeper analysis of the three-dimensionality of the mean flow features revealed the presence of multiple (diagonal) corner shocks emanating from the top and bottom walls at several streamwise locations. These corner shocks are responsible for the lenticular (curved) shape of the Mach stem and also, further downstream, for

the constructive interference, which produces an additional shock wave that is not present in the spanwise-periodic simulation, for which corner shocks cannot occur.

The mean separation bubble shows a strong three-dimensionality imposed by the lateral confinement. For the spanwise-periodic simulation, the separation bubble is significantly smaller, in agreement with earlier findings in the literature when comparing previous numerical simulations (assuming spanwise periodicity) with experimental results. The profiles of the streamwise skin friction coefficient and the wall pressure for the interaction strengths simulated were compared, confirming a link between the three-inflection-point wall pressure profile and presence of mean flow reversal (found for the intermediate and stronger simulations of the present work). The skewed streamwise shape of the separation bubble towards more downstream locations was linked to the patterns of instantaneous separation, which were found to be more elongated and intermittent at upstream locations of the interaction.

The study of secondary mean flow patterns showed the strong three-dimensionality imposed by the sidewalls, with cross-sectional dominant motions transitioning from being primarily vertical in the most-upstream interactions to complex multi-cell configurations involving strong lateral motions further downstream, responsible for the curvature of the shock system not observed in the spanwise-periodic simulation. A closer look at one of the corners revealed the presence of turbulent secondary flows of Prandtl's second kind, induced by gradients of Reynolds stresses. The initially symmetric pattern of counter-rotating vortices found near each corner upstream of the STBLIs is broken by the strong downward and upward motions imposed as the shock system is traversed. In the relaxation regions that follow, the two-pair vortex configuration is recovered, although it is not symmetric with respect to the corner bisector.

When looking at the instantaneous flow structure, significant departures from the time-averaged features were observed, not only affecting the interaction of the shocks with the boundary layers, but also the shape and extent of the Mach stem and its wake, even though they are located further away from the TBLs. The wake, in particular, was found to develop Kelvin–Helmholtz instabilities in the limiting shear layers, which are amplified as the downstream shocks are traversed.

Finally, from the spectral analysis of the wall pressure signals taken in arrays of probes at the centre plane and near the sidewall (the latter only for the simulation with sidewalls, and the former also for the spanwise-periodic simulation), low-frequency motions were observed near the foot of the separation shock at each STBLI, even though the spectral density content at these low frequencies is not always dominant over the broadband range of turbulence time scales of the incoming boundary layers. The frequencies at which these low-frequency motions occur are consistent with the range found in prior studies in the literature. Secondary STBLIs, which showed a more unsteady behaviour in the study of the instantaneous flow features, also present higher levels of low-frequency unsteadiness. However, there are differences between the location of the spectral density peaks for the two simulations (corresponding to lower frequencies in the spanwise-periodic simulation) as well as between the centre and near-sidewall planes under consideration for the simulation with sidewalls. The lack of statistical spectral coherence of corresponding signals located in each one of those planes, and also between probes located at consecutive interactions, suggests a nonlinear coupling between the different low-frequency motions of the shock system. In both simulations, and for the different spanwise-normal planes considered, the broadband spectral density found in the range of frequencies corresponding to the turbulence in the incoming boundary layers was mildly shifted to lower frequencies inside the STBLIs, and split into a two-peak structure in the relaxation zones.

Acknowledgements

Financial support was provided by the United States National Nuclear Security Administration (NNSA), Department of Energy, under the Predictive Science Academic Alliance Program (PSAAP) at Stanford University (DE-FC52-08NA28614), directed by P. Moin, who is gratefully acknowledged. We are also grateful to F. Ham and R. Vicquelin for early developments of the numerical code used in this work and to G. Iaccarino for useful discussions. Computer time was provided by the Open Computing Facility (OCF) at Lawrence Livermore National Laboratory (LLNL), and the High Performance Computing Center at Stanford University (NSF MRI-R2 award 960306).

Appendix

This appendix contains a further validation case for the WMLES approach employed in this work. In contrast to the 1.1 mm-high wedge case, which showed no mean separation, and the 3 mm-high compression wedge configuration, for which incipient separation occurred, this appendix targets a stronger STBLI that leads to a larger region of mean flow reversal. The objective is to assess the ability of simulations employing the equilibrium wall model described in § 2.1 to reproduce the flow features for stronger interactions such as the one corresponding to the 5 mm-high compression wedge that is analysed in the present study in § 3.2.

We consider the experiments of Dupont *et al.* (2005, 2006), Piponniau (2009), Piponniau *et al.* (2009) and Souverein *et al.* (2010) on an oblique shock wave impinging on a TBL at an approximate Mach number of 2.3. These experiments were done in the continuously operated supersonic wind tunnel at the Institut Universitaire des Systèmes Thermiques Industrieles (IUSTI) for a range of shock intensities, by varying the deflection angle of a sharp-edge plate (the shock generator) located in the free stream and attached to the top wall of the wind tunnel. The shock generator spans the tunnel cross-section. The largest deflection angle (9.5°) of the incident shock tested experimentally will be considered in our simulations, as it resulted in the strongest mean flow reversal observed experimentally. Previous computational studies of STBLI have used these experiments for validation purposes, mainly focusing on a lower (8°) deflection angle, for which milder separation occurs. Most of these computational studies considered spanwise periodicity and a lower Reynolds number than in the experiments, to reduce the computational cost of the DNS or wall-resolved LES (see, e.g., Garnier, Sagaut & Deville 2002; Touber & Sandham 2009*a*; Pirozzoli & Bernardini 2011; Morgan *et al.* 2013). Garnier (2009) performed stimulated detached eddy simulation (SDES) for the 9.5° shock deflection angle case, including the top wall and sidewalls of the wind tunnel in the computational domain. The sidewalls were found to strengthen the interaction by reducing the effective section of the wind tunnel.

In the present simulations, the computational domain comprises only a section of the wind tunnel containing the shock generator and the first STBLI on the bottom wall. The full cross-section of the wind tunnel (120 mm tall in y and 170 mm wide in z) is included, thus accounting for the confinement effects imposed by the sidewalls. The shock generator is modelled as a 9.5° inclined compression on the top wall, extending 190 mm downstream and thus protruding into the free stream. A constant-area section follows. In the experiment, a sharp-edge plate was placed directly in the free stream, attached to the top wall. The inlet of the computational domain is located 150 mm upstream of the start of the shock generator, whereas the outlet is located 310 mm downstream.

	M	δ_{99} (mm)	θ (mm)	H	Re_θ ($\times 10^3$)	C_f ($\times 10^{-3}$)	u_τ (m s^{-1})	L_i (mm)	L_s (mm)	h (mm)	$\Delta p/2\tau_{w0}$
Experiment	2.28	11	0.96	3.53	5.1	2	$\approx$25	71.5	66.5	10.2	50
WMLES$_s$	2.27	11.5	0.99	3.54	5.5	2.1	23.8	70.0	51.1	4.2	48.6
WMLES$_p$	2.28	11.5	0.98	3.57	5.5	2.1	23.4	51.5	32.2	1.6	48.8

TABLE 2. Flow parameters of the incoming TBL and the interaction retrieved from experiments (Piponniau *et al.* 2009; Souverein *et al.* 2010) and the present simulations (WMLES$_s$, simulation with sidewalls; WMLES$_p$, simulation with spanwise periodicity): M, free-stream Mach number; δ_{99}, boundary layer thickness; θ, momentum thickness; H, shape factor; Re_θ, Reynolds number based on the momentum thickness and the free-stream density, velocity and dynamic viscosity; C_f, streamwise skin friction coefficient (a value of 2.1×10^{-3} is reported in Souverein *et al.* 2010); u_τ, friction velocity; L_i, interaction length; h, maximum height of the mean dividing streamline line (defined as $y_d(x)$ such that $\int_0^{y_d(x)} \rho u \mathrm{d}y$); $\Delta p/2\tau_{w0}$, normalized shock intensity (Δp is the pressure jump across the incident shock and τ_{w0} is the wall shear stress of the incoming boundary layer).

Experimental PIV measurements of mean and turbulence quantities in the spanwise centre plane (Piponniau 2009) near the bottom wall are used to synthetically generate a turbulent inflow boundary condition following the same digital filtering technique described in § 2.2. In contrast to the rest of the simulations presented in this study, no experimental PIV data were available in planes away from the spanwise centre of the duct. Therefore, the one-dimensional PIV profiles at the centre plane are extruded along the spanwise direction up to a distance to each sidewall equal to the boundary layer thickness of the bottom wall. The relevant information needed to complete the mean and turbulence wall-normal profiles in the sidewall boundary layers is translated from the bottom-wall boundary layer. Thus, the thicknesses of the sidewalls and bottom-wall boundary layers are assumed equal, for lack of better information. This characterization of the sidewall boundary layers is far from complete, but the effect of confinement is, at least, present in these simulations. The equilibrium wall model described in § 2.1 is applied on the bottom wall, which is considered adiabatic. No-slip adiabatic boundary conditions are used to model the side and top walls: since data of the incoming boundary layers on those walls were not reported experimentally, the purpose of including those walls in the simulation is to assess any confinement effects, but not to have a full characterization of the flow features near those walls. To this effect, simulations with and without sidewalls (the latter using spanwise periodicity) are performed, and the results will be compared with experimental data in the remainder of this appendix. The spanwise-periodic simulations have a domain width equal to $6\delta_o$. The simulation with sidewalls will be referred as WMLES$_s$, whereas the spanwise-periodic simulation will be denoted by WMLES$_p$.

The mesh resolution is uniform in the streamwise and spanwise directions and equal to $\delta_o/\Delta_x \approx 8$ and $\delta_o/\Delta_z \approx 16$, respectively. In the wall-normal direction, the mesh spacing at the wall is $\delta_o/\Delta_y \approx 40$, and stretches to a uniform $\delta_o/\Delta_y \approx 10$ spacing above $3\delta_o$. In viscous units, $\Delta_x^+ \approx 100$, $\Delta_y^+ \approx 20 \rightarrow 80$ and $\Delta_z^+ \approx 50$. The exchange location of the wall model is at $0.06\delta_o$ above the wall. Statistics are collected for approximately $3500\delta_o/U_o$ ($\approx$85 flow-through times).

Table 2 shows the flow parameters of the incoming boundary layer and the separation bubble at the interaction, comparing experimental (Piponniau *et al.* 2009;

Souverein *et al.* 2010) and simulation values. The interaction length, L_i, is defined as the distance between the mean position of the separation shock and the intersection of the extrapolation to the wall of the incident shock with the bottom wall. The latter point is taken as the origin of the streamwise coordinate, x.

Morgan *et al.* (2013) performed spanwise-periodic wall-resolved simulations of this case at a reduced Reynolds number of $Re_\theta = 1500$, obtaining an interaction length of $L_i/\delta_o = 3.8$, lower than the $L_i/\delta_o = 4.5$ obtained in the present WMLES when spanwise periodicity is used. However, these values are significantly lower than the $L_i/\delta_o = 6.4$ found in the WMLES with sidewalls, which is in close agreement with the 6.45 value reported in the experiments (Dupont *et al.* 2006). This result indicates that, while a lowered Reynolds number may effectively lead to an under-prediction of the interaction length in simulations, the main contributor to that under-prediction found in prior DNS and LES of STBLI may be dominated by the assumed spanwise periodicity that prevents any confinement effects otherwise imposed by sidewalls. A similar conclusion about the smaller relevance of the Reynolds number in the interaction length was suggested, for a lower range of Reynolds numbers, in the parametric study of Morgan *et al.* (2013).

Whereas the interaction length, L_i, observed experimentally is closely matched in the present simulations when sidewalls are included, the separation length, L_s, and the maximum height of the dividing streamline, h, are under-predicted in the simulations. These values are considerably improved with respect to spanwise-periodic simulations, but the under-prediction is still significant (23 % and 59 %, respectively). The use of a wall model in the separated region might be one cause of this discrepancy: owing to the reduced-friction Reynolds number attained in that region, locally reverting to a no-slip boundary condition (without applying the wall model) may be more suitable, although it would require the addition of a sensor to the flow solver that is able to distinguish attached and separated flow regions and selectively apply the wall model only in the former. Besides the wall model, there are other factors that might lead to discrepancies of the length and height of the separation bubble between experiments and simulations: for example, differences in the streamwise extent of the shock generator, the geometry of which is not fully characterized in Piponniau *et al.* (2009), or different boundary layer thicknesses on the sidewalls (considered of equal thickness to that of the bottom wall in the present simulations, due to lack of PIV data away from the centre plane).

Figure 29(*a*) compares the time-averaged mean streamwise velocity profile on the centre plane for the incoming boundary layer near the bottom wall upstream of the STBLI, both in outer and viscous units, showing a good agreement between experiments and simulations (only the simulation with sidewalls is considered in that figure). Figure 29(*b*) shows a comparison of the downstream evolution of the wall pressure across the STBLI. The simulation follows the experimental values except in the region near the separation point (marked by the leftmost vertical dashed line), where it is seen to under-predict the values found experimentally. We note that this region partially overlaps with the oscillation zone of the unsteadiness of the separation shock. An estimate of the variability in experimental measurements of the wall pressure can be inferred from the upstream values included in that figure. Halfway through the mean separation bubble, the agreement between simulation and experiments improves, reaching a common value downstream of the interaction, significantly lower than the one that would correspond to inviscid theory (marked with a dash–dotted line).

Figure 30 compares two-dimensional contours of time-averaged velocities and Reynolds stresses extracted from the vertical plane located at the spanwise centre of

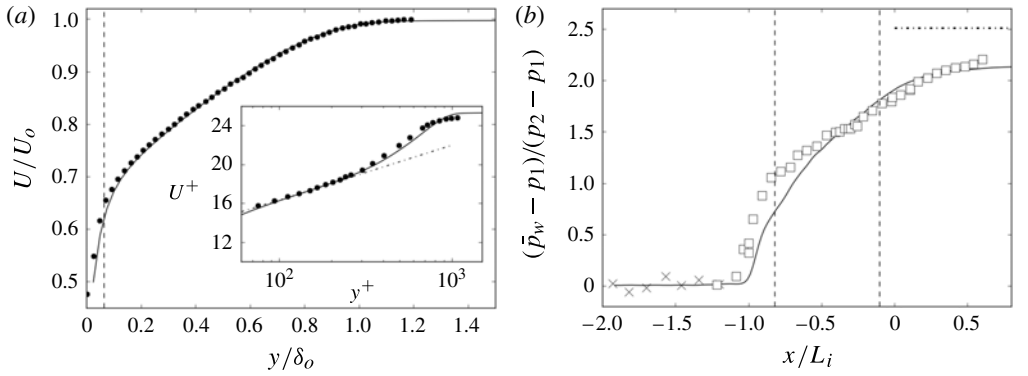

FIGURE 29. (*a*) The wall-normal profile of the time-averaged mean streamwise velocity of the incoming boundary layer at the spanwise centre, comparing the WMLES$_s$ simulation results (solid line) and experiment (symbols) (from Souverein *et al.* 2010). The vertical dashed line indicates the exchange location of the wall model. The inset shows the van Driest transformed streamwise velocity above the wall-model exchange location. (*b*) The streamwise profile of the time-averaged mean wall pressure, $\bar{p}_w$ along the STBLI (p_1 is the pressure upstream of the interaction; p_2 is the pressure downstream of the incident oblique shock), comparing WMLES$_s$ results (solid line) with experiments (symbols) (Dupont *et al.* 2006): squares correspond to $\theta = 9.5°$; crosses correspond to $\theta = 7°$ and are shown in this plot only upstream of the interaction, where experimental data for $\theta = 9.5°$ were not available. Vertical dashed lines represent the separation and reattachment points found in the WMLES$_s$ based on the time-averaged mean velocity field. The horizontal dash–dotted line at the top left corresponds to the pressure downstream of the shock reflection resulting from inviscid theory ($(\bar{p}_{wi} - p_2)/(p_2 - p_1) \approx 2.51$).

the wind tunnel. The background colour maps correspond to the experimental PIV data of Piponniau (2009), whereas the superimposed contour lines correspond to the simulations. The coordinate axes have been rescaled with the interaction length, L_i, as in previous numerical studies (Pirozzoli & Bernardini 2011; Morgan *et al.* 2013). Note that this scaling has no effect in the comparison between experiments and results from the simulation with sidewalls, since the interaction lengths are practically the same (see table 2); however, as was found in those previous studies, the simulation with spanwise periodicity has a significantly shorter interaction length and thus this rescaling step was necessary in those prior studies for a meaningful comparison, and is replicated here. Despite the improved results derived from this rescaling step for the spanwise-periodic simulation, the agreement with experiments of flow features observed in the simulation with sidewalls is superior. For example, the contour lines in the relaxation region shown for the streamwise velocity (figure 30*a*,*f*) follow the experimental contours more closely. Likewise, the height and shape of the region of high normal streamwise Reynolds stress (figure 30*c*,*h*) is better captured in the simulation with sidewalls. The qualitative agreement of the flow features, location and extent of the extrema of flow quantities plotted in figure 30 appears reasonably good, particularly for the simulation with sidewalls, for which no rescaling is needed.

Figures 31 and 32 show one-dimensional, wall-normal profiles at different streamwise locations in the interaction region and upstream, comparing experimental PIV data and numerical results for both simulation with sidewalls and with spanwise periodicity. As in figure 30, the wall-normal coordinate has been rescaled with the interaction length. The time-averaged streamwise and vertical velocities show good

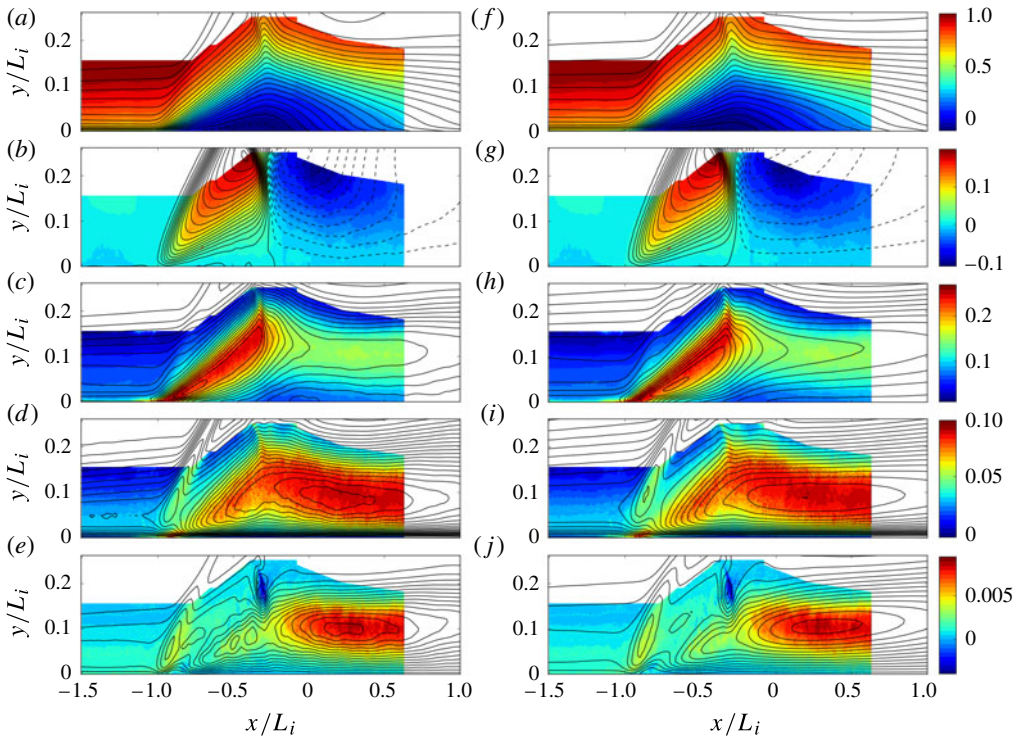

FIGURE 30. Time-averaged velocities and Reynolds stresses on the spanwise centre plane in the STBLI region. Experimental PIV data (Piponniau 2009; Piponniau *et al.* 2009) are shown as background colour maps, with simulation results given by (15) superimposed black contour lines. The left-hand plots (*a–e*) correspond to the simulations with sidewalls, whereas the right-hand plots (*f–j*) correspond to spanwise-periodic simulations. From top to bottom: streamwise velocity, U/U_o (*a*,*f*); vertical velocity, V/U_o (*b*,*g*); streamwise normal Reynolds stress, $\sqrt{\overline{u'u'}}/U_o$ (*c*,*h*); vertical normal Reynolds stress, $\sqrt{\overline{v'v'}}/U_o$ (*d*,*i*); Reynolds shear stress, $-\overline{u'v'}/U_o^2$ (*e*,*j*).

agreement for the simulation with sidewalls. Some discrepancies are observed for profiles in the separated and relaxation regions, where the streamwise velocity is somewhat over-predicted near the wall. The streamwise and shear Reynolds stresses shown in figure 32(*a*,*c*) follow the experimental values closely. Profiles of vertical Reynolds stresses from the simulations shown in figure 32(*b*) appear to over-predict the experimental values, dropping more slowly to zero away from the wall. Also, a region of high vertical Reynolds stress seen experimentally at the foot of the separation shock is not captured in the simulations (see the second plot in figure 32*b* and figure 30*d*,*i* at $x/L \approx -0.9$).

Besides these quantitative comparisons between experimental measurements and simulation results, two additional features of the interaction observed experimentally are explored in the simulations: the three-dimensionality imposed by the presence of the sidewalls, and the low-frequency unsteadiness near the separation shock.

Figure 33 shows mean streamlines and separation lines on horizontal planes extracted at increasing heights from the bottom wall. The results from the simulations show qualitatively a similar three-dimensionality imposed by the sidewalls with respect to the experimental PIV data shown in Dussauge *et al.* (2006) and Piponniau

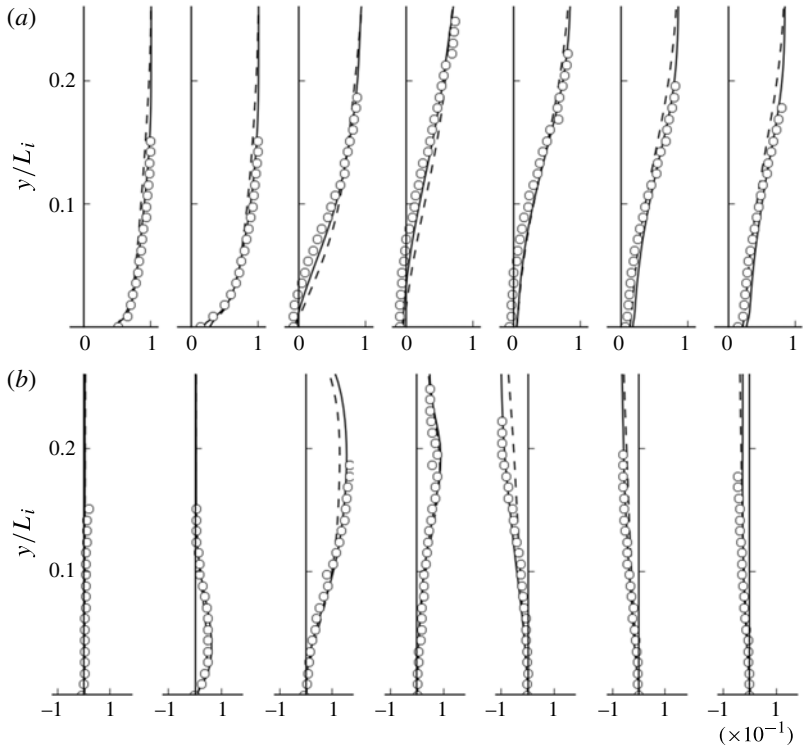

FIGURE 31. One-dimensional wall-normal profiles of time-averaged streamwise (a) and vertical (b) velocities, U/U_o^2 and V/U_o^2, extracted at rescaled streamwise locations $x/L_i = \{-1.2, -0.9, -0.6, -0.3, 0.0, 0.3, 0.6\}$. Symbols: PIV experimental data (from Piponniau 2009); solid line: data from simulation with sidewalls; dashed line: data from simulation with spanwise periodicity.

(2009): besides the separation bubble being confined to a core region of the duct, two counter-rotating vortices are observed downstream of the separation shock ($x/L_i > -1$). As the height of the horizontal plane increases, the traces of these vortices move downstream (starting from approximately the midpoint of the interaction region, very close to the bottom wall) and closer to the spanwise centre plane. These results from the simulations are consistent with the findings of Dussauge *et al.* (2006), who proposed that these tornado-like vortices are responsible for unsteady shock motions. We note that, despite the qualitative agreement, the core of these vortices at the wall is closer to the centre plane in the experiments than in the simulations, which could be another indication of a difference in the thickness of the sidewall boundary layers. Besides the size difference of the separation bubble between experiments and simulations described above, its upstream shape also appears to differ, being more diamond-like in the experiments (see figure 6 in Dussauge *et al.* 2006), whereas the simulations show a region near the spanwise core of the duct that is more two-dimensional. Once again, the actual size and influence of the sidewall boundary layers, not characterized in the experiment and probably different in our simulations, might be the reason for these discrepancies.

Low-frequency unsteadiness observed experimentally is also reproduced in the simulations, as shown in figure 34 through contours of the premultiplied power spectral density (PSD′) of the wall pressure signals. These signals are extracted

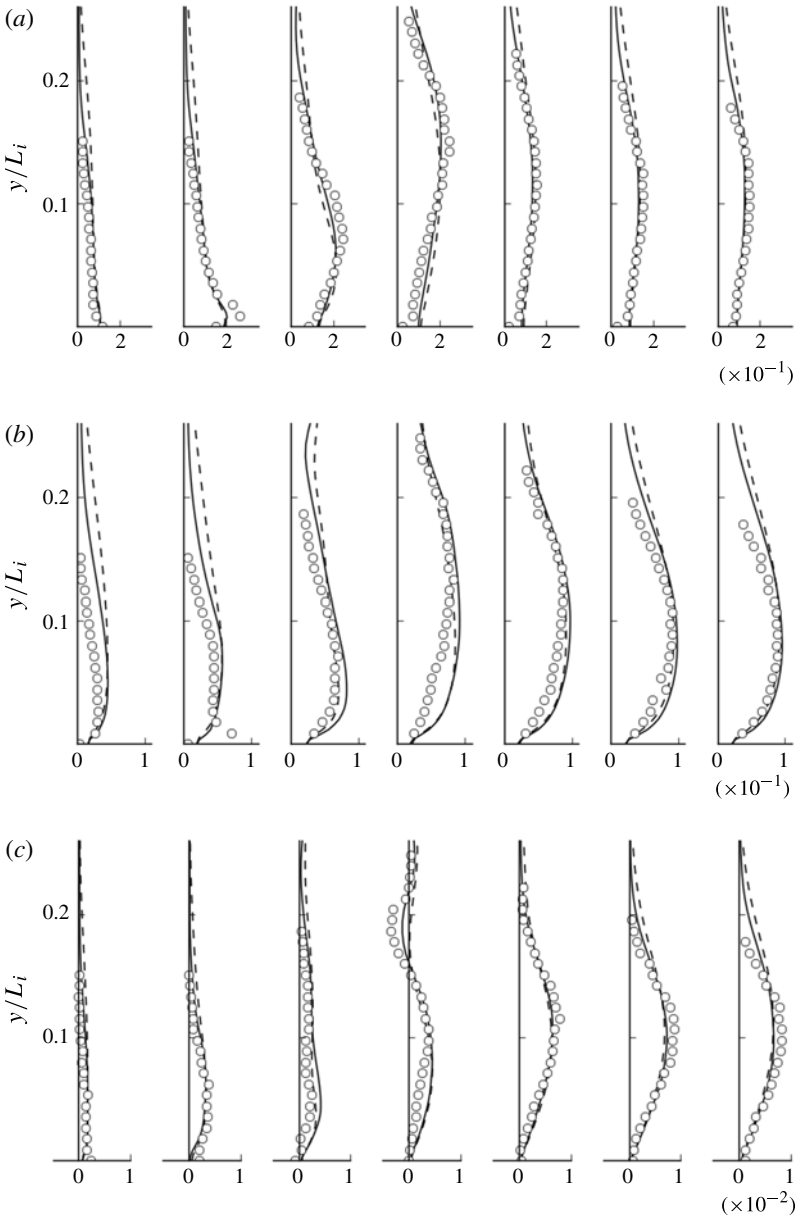

FIGURE 32. One-dimensional wall-normal profiles of time-averaged Reynolds stresses extracted at rescaled streamwise locations $x/L_i = \{-1.2, -0.9, -0.6, -0.3, 0.0, 0.3, 0.6\}$. (*a*) Streamwise Reynolds stress, $\sqrt{\overline{u'u'}}/U_o$; (*b*) Vertical Reynolds stress, $\sqrt{\overline{v'v'}}/U_o$; (*c*) Reynolds shear stress, $-\overline{u'v'}/U_o^2$. Symbols: PIV experimental data (from Piponniau 2009); solid line: data from the simulation with sidewalls; dashed line: data from the simulation with spanwise periodicity.

from probes located at the spanwise centre along the bottom wall. The PSD′ are plotted as a function of the streamwise location and the normalized frequency $St = f\delta_o/U_o$, where $U_o \approx 550$ m s^{-1}. The sampling frequency is $f \approx 200U_o/\delta_o$. At each streamwise location, the corresponding PSD′ shown in figure 34 has been

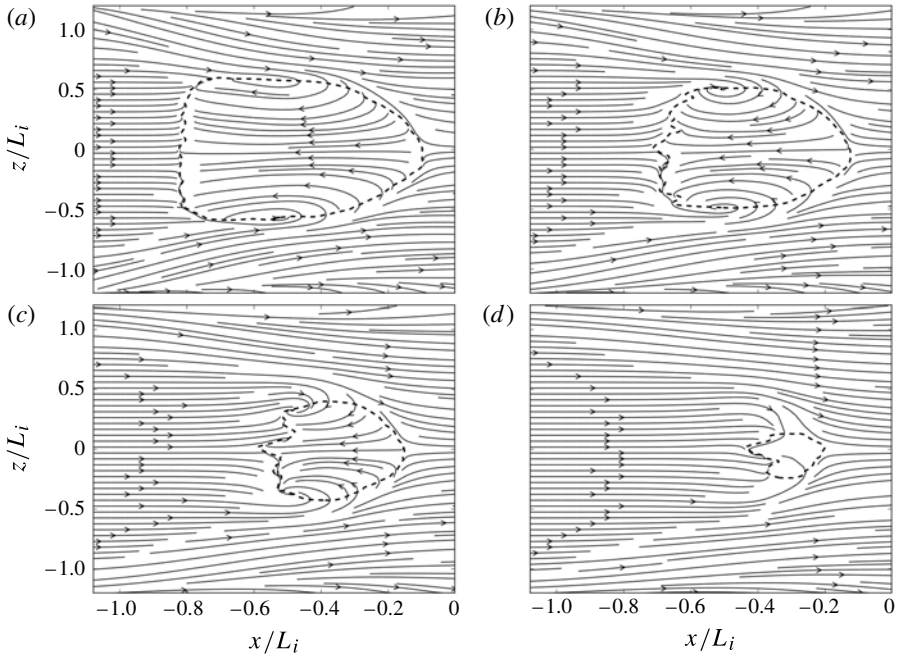

FIGURE 33. Streamlines (solid lines with arrows indicating the fluid motion) obtained from the time-averaged mean velocity on horizontal planes extracted at locations $y/h = \{0.02, 0.12, 0.24, 0.48\}$ (a,b,c,d, respectively). Dashed lines represent the loci of mean longitudinal velocity, thus demarcating the separation bubble.

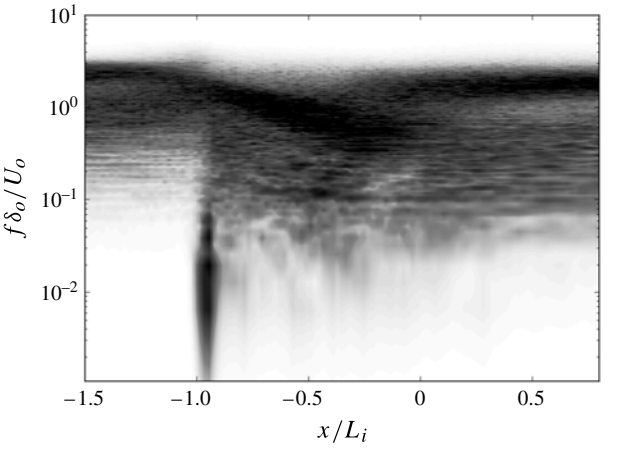

FIGURE 34. Contours of the premultiplied power spectral density (PSD′) (arbitrary scale) of the wall pressure signals on the bottom wall at the spanwise centre of the duct, as a function of the streamwise location rescaled by the interaction length, L_i and the Strouhal number $St = f\delta_o/U_o$. Here, PSD′s are normalized for each streamwise location.

normalized with its integrated value across all frequencies. It is noticed that upstream of the interaction ($x/L < -1$) energy is contained in frequencies of the order of the characteristic boundary layer frequency ($St \sim O(1)$). At the start of the interaction region ($x/L \approx -1$), near the foot of the separation shock, the pressure signal shows

the dominance of low frequencies such that $St \sim O(0.01)$. Further downstream in the interaction region, the low frequencies are no longer dominant, but intermediate frequencies develop, and the original dominant frequencies of the incoming boundary layer appear to be progressively lowered by the action of the STBLI, In the relaxation region ($x/L_i > 0$), higher frequencies observed in the incoming boundary layer are recovered and amplified, while the rest of the spectral density function has been broadened with respect to the incoming boundary.

REFERENCES

ADAMSON, T. C. JR & MESSITER, A. F. 1980 Analysis of two-dimensional interactions between shock waves and boundary layers. *Annu. Rev. Fluid Mech.* **12**, 103–138.

BABINSKY, H. & HARVEY, J. K. 2011 *Shock Wave–Boundary-Layer Interactions*, Cambridge Aerospace Series. Cambridge University Press.

BALARAS, E., BENOCCI, C. & PIOMELLI, U. 1996 Two-layer approximate boundary conditions for large-eddy simulations. *AIAA J.* **34** (6), 111–1119.

BERESH, S., CLEMENS, N. & DOLLING, D. 2002 Relationship between upstream turbulent boundary-layer velocity fluctuations and separation shock unsteadiness. *AIAA J.* **40**, 2412–2422.

BERMEJO-MORENO, I., LARSSON, J. & LELE, S. K. 2010 LES of canonical shock-turbulence interaction. In *Annual Research Briefs*, pp. 209–222. Center for Turbulence Research.

BODART, J. & LARSSON, J. 2012 Sensor-based computation of transitional flows using wall-modeled large eddy simulation. In *Annual Research Briefs*, pp. 229–240. Center for Turbulence Research.

BOURGOING, A. & REIJASSE, PH. 2005 Experimental analysis of unsteady separated flows in a supersonic planar nozzle. *Shock Waves* **14** (4), 251–258.

BRADSHAW, P. 1987 Turbulent secondary flows. *Annu. Rev. Fluid Mech.* **19**, 53–74.

BRUCE, P. J. K., BURTON, D. M. F., TITCHENER, N. A. & BABINSKY, H. 2011 Corner effect and separation in transonic channel flows. *J. Fluid Mech.* **679**, 247–262.

CABOT, W. 1995 Large-eddy simulations with wall models. In *Annual Research Briefs*, pp. 41–50. Center for Turbulence Research.

CAMPO, L. M., HELMER, D. B. & EATON, J. K. 2012 Validation experiment for shock boundary layer interactions: sensitivity to upstream geometric perturbations. *AIAA* 2012-1440.

CAMPO, L. M., HELMER, D. B. & EATON, J. K. 2013 PIV investigation of spanwise variation in incident shock boundary layer interactions. In *Proceedings of the 8th TSFP-8*. Poitiers, France.

CHAPMAN, D. R. 1979 Computational aerodynamics development and outlook. *AIAA J.* **17**, 1293–1313.

CHAPMAN, D. R., KUEHN, D. M. & LARSON, H. K. 1957 Investigations of separated flow in supersonic and subsonic streams with emphasis on the effect of transition. NACA *Tech. Rep.* R-1356.

CHOI, H. & MOIN, P. 2012 Grid-point requirements for large eddy simulation: Chapman's estimates revisited. *Phys. Fluids* **24**, 011702.

CLEMENS, N. T. & NARAYANASWAMY, V. 2014 Low-frequency unsteadiness of shock wave/turbulent boundary layer interactions. *Annu. Rev. Fluid Mech.* **46**, 469–492.

DAVIS, D. O. & GESSNER, F. B. 1989 Further experiments on supersonic turbulent flow development in a square duct. *AIAA J.* **27** (8), 1023–1030.

DAVIS, D. O., GESSNER, F. B. & KERLICK, G. D. 1986 Experimental and numerical investigation of supersonic turbulent flow through a square duct. *AIAA J.* **24**, 1508–1515.

DÉLERY, J. & DUSSAUGE, J.-P. 2009 Some physical aspects of shock wave/boundary layer interactions. *Shock Waves* **19**, 453–468.

DÉLERY, J., MARVIN, J. G. & RESHOTKO, E. 1986 Shock-wave boundary layer interactions. *Tech. Rep.* AGARD-AG-280. NATO, Advisory Group for Aerospace Research and Development.

DOLLING, D. S. 2001 Fifty years of shock-wave/boundary-layer interaction research: what next? *AIAA J.* **39**, 1517.

DOLLING, D. S. & OR, C. T. 1985 Unsteadiness of the shock wave structure in attached and separated compression ramp flows. *Exp. Fluids* **3**, 24–32.

DUPONT, P., HADDAD, C., ARDISSONE, J. P. & DEBIÈVE, J. 2005 Space and time organization of a shock wave/turbulent boundary layer interaction. *Aerosp. Sci. Technol.* **9**, 561–572.

DUPONT, P., HADDAD, C. & DEBIÈVE, J. 2006 Space and time organization in a shock-induced separated boundary layer. *J. Fluid Mech.* **559**, 255–277.

DUSSAUGE, J.-P., DUPONT, P. & DEBIÈVE, J.-F. 2006 Unsteadiness in shock wave boundary layer interactions with separation. *Aerosp. Sci. Technol.* **10** (2), 85–91.

EDWARDS, J. R. 2008 Numerical simulations of shock/boundary layer interactions using time-dependent modeling techniques: a survey of recent results. *Prog. Aerosp. Sci.* **44**, 447–465.

EDWARDS, J. R., CHOI, J.-I. & BOLES, J. A. 2008 Hybrid large-eddy/Reynolds-averaged Navier–Stokes simulation of a Mach-5 compression corner interaction. *AIAA J.* **46** (4), 977–991.

GANAPATHISUBRAMANI, B., CLEMENS, N. T. & DOLLING, D. S. 2007 Effects of upstream boundary layer on the unsteadiness of shock-induced separation. *J. Fluid Mech.* **585**, 369–394.

GANAPATHISUBRAMANI, B., CLEMENS, N. T. & DOLLING, D. S. 2009 Low-frequency dynamics of shock-induced separation in a compression ramp interaction. *J. Fluid Mech.* **636**, 397–425.

GARG, S. & SETTLES, G. S. 1996 Unsteady pressure loads generated by swept-shock-wave/boundary-layer interactions. *AIAA J.* **34** (6), 1174–1181.

GARNIER, E. 2009 Stimulated detached eddy simulation of three-dimensional shock/boundary layer interaction. *Shock Waves* **19**, 479–486.

GARNIER, E., SAGAUT, P. & DEVILLE, M. 2002 Large eddy simulation of shock/boundary-layer interaction. *AIAA J.* **40** (10), 1935–1944.

GESSNER, F. B., FERGUSON, S. D. & LO, C. H. 1987 Experiments on supersonic turbulent flow development in a square duct. *AIAA J.* **25**, 690–697.

GIBSON, B. & DOLLING, D. S. 1991 Wall pressure fluctuations near separation in a Mach 5, sharp fin-induced turbulent interaction. *AIAA Paper* 91-0646.

GREEN, J. E. 1970 Reflexion of an oblique shock wave by a turbulent boundary layer. *J. Fluid Mech.* **40**, 81–95.

GRILLI, M., SCHMID, P. J., HICKEL, S. & ADAMS, N. A. 2012 Analysis of unsteady behaviour in shockwave turbulent boundary layer interaction. *J. Fluid Mech.* **700**, 16–28.

GUN'KO, YU. P., KUDRYAVTSEV, A. N. & RAKHIMOV, R. D. 2004 Supersonic inviscid corner flows with regular and irregular shock interaction. *Fluid Dyn.* **39** (2), 304–318.

HADJADJ, A., LARSSON, J., MORGAN, B. E., NICHOLS, J. W. & LELE, S. K. 2010 Large-eddy simulation of shock/boundary-layer interaction. In *Proceedings of the Summer Program*, pp. 141–152. Center for Turbulence Research.

HELMER, D., CAMPO, L. & EATON, J. 2012 Three-dimensional features of a Mach 2.1 shock/boundary layer interaction. *Exp. Fluids* **53**, 1347–1368.

HELMER, D. & EATON, J. 2011 Measurements of a three-dimensional shock–boundary layer interaction. *Tech. Rep.* PhD thesis (TF-126). Stanford University.

HICKEL, S., TOUBER, E., BODART, J. & LARSSON, J. 2012 A parametrized non-equilibrium wall-model for large-eddy simulations. In *Proceedings of the Summer Program*, pp. 127–136. Center for Turbulence Research.

HUMBLE, R., ELSINGA, G., SCARANO, F. & VAN OUDHEUSDEN, B. 2009*a* Three-dimensional instantaneous structure of a shock wave/turbulent boundary layer interaction. *J. Fluid Mech.* **622**, 33–62.

HUMBLE, R. A., SCARANO, F. & VAN OUDHEUSDEN, B. W. 2009*b* Unsteady aspects of an incident shock wave/turbulent boundary layer interaction. *J. Fluid Mech.* **635**, 47–74.

HUSER, A. & BIRINGEN, S. 1993 Direct numerical simulation of turbulent flow in a square duct. *J. Fluid Mech.* **257**, 65–95.

JOUNG, Y., CHOI, S. U. & CHOI, J.-I. 2007 Direct numerical simulation of turbulent flow in a square duct: analysis of secondary flows. *J. Engng Mech. ASCE* **213**, 213–221.

KAWAI, S. & LARSSON, J. 2012 Wall-modeling in large eddy simulation: length scales, grid resolution and accuracy. *Phys. Fluids* **24**, 15105.

KAWAI, S. & LARSSON, J. 2013 Dynamic non-equilibrium wall-modeling for large eddy simulation at high Reynolds numbers. *Phys. Fluids* **25**, 015105.

KHALIGHI, Y., NICHOLS, J. W., LELE, S., HAM, F. & MOIN, P. 2011 Unstructured large eddy simulations for prediction of noise issued from turbulent jets in various configurations. *AIAA* 2011-2886.

KLEBANOFF, P. S. 1955 Characteristics of turbulence in a boundary layer with zero pressure gradient. NACA *Tech. Rep.* 1247.

KLEIN, M., SADIKI, A. & JANICKA, J. 2003 A digital filter based generation of inflow data for spatially developing direct numerical or large eddy simulations. *J. Comput. Phys.* **186**, 652–665.

KUEHN, D. M. 1959 Experimental investigation of the pressure rise required for the incipient separation of turbulent boundary layers in two-dimensional supersonic flow. *NASA Memo.* 1-21-59A.

KUTLER, P. 1974 Supersonic flow in the corner formed by two intersecting wedges. *AIAA J.* **12** (5), 577–578.

LARSSON, J. & LELE, S. K. 2009 Direct numerical simulation of canonical shock/turbulence interaction. *Phys. Fluids* **21**, 126101.

LUND, T. S., WU, X. & SQUIRES, K. D. 1998 Generation of turbulent inflow data for spatially-developing boundary layer simulations. *J. Comput. Phys.* **140**, 233–258.

MORGAN, B., DURAISAMY, K., NGUYEN, N., KAWAI, S. & LELE, S. K. 2013 Flow physics and RANS modelling of oblique shock/turbulent boundary layer interaction. *J. Fluid Mech.* **729**, 231–284.

MORGAN, B., LARSSON, J., KAWAI, S. & LELE, S. K. 2011 Improving low-frequency characteristics of recycling/rescaling inflow turbulence generation. *AIAA J.* **49** (3), 582–597.

PIOMELLI, U. & BALARAS, E. 2002 Wall-layer models for large-eddy simulations. *Annu. Rev. Fluid Mech.* **34**, 349–374.

PIPONNIAU, S. 2009 Instationnarités dans les décollements compressibles: cas des couches limites soumises à ondes de choc. PhD thesis, L'Univerisité de Provence.

PIPONNIAU, S., DUSSAUGE, J. P., DEBIÈVE, J. F. & DUPONT, P. 2009 A simple model for low-frequency unsteadiness in shock-induced separation. *J. Fluid Mech.* **629**, 87–108.

PIROZZOLI, S. 2012 On the size of the energy-containing eddies in the outer turbulent wall layer. *J. Fluid Mech.* **702**, 521–532.

PIROZZOLI, S. & BERNARDINI, M. 2011 Direct numerical simulation database for impinging shock wave/turbulent boundary-layer interaction. *AIAA J.* **49** (6), 1307–1312.

PIROZZOLI, S. & GRASSO, F. 2006 Direct numerical simulation of impinging shock wave/turbulent boundary layer interaction at $M = 2.25$. *J. Comput. Phys.* **18** (6), 065113.

PIROZZOLI, S., LARSSON, J., NICHOLS, J. W., BERNARDINI, M., MORGAN, B. E. & LELE, S. K. 2010 Analysis of unsteady effects in shock/boundary layer interactions. In *Annual Research Briefs*, pp. 153–164. Center for Turbulence Research.

PLOTKIN, K. J. 1975 Shock wave oscillation driven by turbulent boundary-layer fluctuations. *AIAA J.* **13** (8), 1036–1040.

PRIEBE, S. & MARTIN, M. P. 2012 Low-frequency unsteadiness in shock wave-turbulent boundary layer interaction. *J. Fluid Mech.* **699**, 1–49.

PRIEBE, S., WU, M. & MARTIN, M. P. 2009 Direct numerical simulation of a reflected-shock-wave/turbulent-boundary-layer interaction. *AIAA J.* **47** (5), 1173–1185.

RINGUETTE, M. J., BOOKEY, P., WYCKHAM, C. & SMITS, A. J. 2009 Experimental study of a Mach 3 compression ramp interaction at $Re_\theta = 2400$. *AIAA J.* **47** (2), 373–385.

SOUVEREIN, L. J. 2010 On the scaling and unsteadiness of shock induced separation. *Tech. Rep.* PhD thesis, Université de Provence Aix-Marseille I.

SOUVEREIN, L., DUPONT, P., DEBIEVE, J., VAN DUSSAUGEN, J., OUDHEUSDEN, B. & SCARANO, F. 2010 Effect of interaction strength on unsteadiness in turbulent shock-wave-induced separations. *AIAA J.* **48**, 1480–1493.

SPALART, P. R. 2009 Detached-eddy simulation. *Annu. Rev. Fluid Mech.* **41**, 181–202.

TOBAK, M. & PEAKE, D. J. 1982 Topology of three-dimensional separated flows. *Annu. Rev. Fluid Mech.* **14**, 61–85.

TOMKINS, C. D. & ADRIAN, R. J. 2003 Spanwise structure and scale growth in turbulent boundary layers. *J. Fluid Mech.* **490**, 37–74.

TOUBER, E. & SANDHAM, N. 2009*a* Comparison of three large-eddy simulations of shock-induced turbulent separation bubbles. *Shock Waves* **19** (6), 469–478.

TOUBER, E. & SANDHAM, N. 2009*b* Large-eddy simulation of low-frequency unsteadiness in a turbulent shock-induced separation bubble. *Theor. Comput. Fluid Dyn.* **23**, 79–107.

TOUBER, E. & SANDHAM, N. 2011 Low-order stochastic modelling of low-frequency motions in reflected shock-wave/boundary-layer interactions. *J. Fluid Mech.* **671**, 417–465.

TUTKUN, M., GEORGE, W. K., DELVILLE, J., STANISLAS, M., JOHANSSON, P. B. V., FOUCAUT, J.-M. & COUDERT, S. 2009 Two-point correlations in high Reynolds number flat plate turbulent boundary layers. *J. Turbul.* **10** (21), 1–23.

URBIN, G. & KNIGHT, D. 2001 Large-eddy simulation of a supersonic boundary layer using an unstructured grid. *AIAA J.* **39** (7), 1288–1295.

VREMAN, A. W. 2004 An eddy-viscosity subgrid-scale model for turbulent shear flow: algebraic theory and applications. *Phys. Fluids* **16** (10), 3670–3681.

WANG, M. & MOIN, P. 2002 Dynamic wall modeling for large-eddy simulation of complex turbulent flows. *Phys. Fluids* **14** (7), 2043–2051.

WU, M. & MARTIN, M. P. 2008 Analysis of shock motion in shockwave and turbulent boundary layer interaction using direct numerical simulation data. *J. Fluid Mech.* **594**, 71–83.

XIE, Z.-T. & CASTRO, I. P. 2008 Efficient generation of inflow conditions for large eddy simulation of street-scale flows. *Flow Turbul. Combust.* **81** (3), 449–470.